Wave shape prediction in complex coastal systems

de Wit, F.P.

DOI
10.4233/uuid:0fb850a4-4294-4181-9d74-857de21265c2

Publication date
2022

Document Version
Final published version

Citation (APA)
de Wit, F. P. (2022). *Wave shape prediction in complex coastal systems*. [Dissertation (TU Delft), Delft University of Technology]. https://doi.org/10.4233/uuid:0fb850a4-4294-4181-9d74-857de21265c2

WAVE SHAPE PREDICTION IN COMPLEX COASTAL SYSTEMS

FLORIS DE WIT

WAVE SHAPE PREDICTION IN COMPLEX COASTAL SYSTEMS

Floris de Wit

Propositions

accompanying the dissertation

Wave Shape Prediction in Complex Coastal Systems

by

Floris Paul de Wit

1. The nonlinear wave shape does not instantly respond to changes in environmental conditions. [This thesis]
2. There is a direct link between the nonlinear wave shape and the bound wave height. [This thesis]
3. The triad source term can be used to account for the evolution of wave shape in spectral wave models. [This thesis]
4. There is a need for fourth generation spectral wave models.
5. Ursell is most well-known for presenting the Stokes nonlinearity number times two.
6. Model stability is often misinterpreted as model accuracy.
7. Sailors understand waves better than coastal modellers.
8. The most effective way to counter climate change is by having less people on planet earth.
9. To stimulate a healthy lifestyle, fruits, vegetables and bikes should be tax free.
10. Running a marathon is healthy.

These propositions are regarded as opposable and defendable, and have been approved as such by the promotors Prof. dr. ir. A.J.H.M. Reniers and dr. M.F.S. Tissier.

Stellingen

behorende bij het proefschrift

Wave Shape Prediction in Complex Coastal Systems

door

Floris Paul de Wit

1. De nietlineaire golfvorm reageert niet instantaan op veranderende omgevings condities. [Dit proefschrift]
2. Er is een directe link tussen de nietlineaire golfvorm en de gebonden golfhoogte. [Dit proefschrift]
3. De triad bronterm kan gebruikt worden om te evolutie van de golfvorm in spectrale golfmodellen bij te houden. [Dit proefschrift]
4. Er is behoefte aan een vierde generatie spectrale golfmodellen.
5. Ursell is het meest bekend voor het presenteren van twee maal het Stokes nietlineairiteit getal.
6. Model stabiliteit wordt vaak onterecht verward met model accuraatheid.
7. Zeilers begrijpen golven beter dan kustmodelleurs.
8. De meest effectieve manier om klimaatverandering tegen te gaan is om minder mensen op aarde te hebben.
9. Om een gezonde levensstijl te stimuleren moeten groenten, fruit en fietsen belasting vrij zijn.
10. Het lopen van een marathon is gezond.

Deze stellingen worden opponeerbaar en verdedigbaar geacht en zijn als zodanig goedgekeurd door de promotoren Prof. dr. ir. A.J.H.M. Reniers and dr. M.F.S. Tissier.

WAVE SHAPE PREDICTION IN COMPLEX COASTAL SYSTEMS

WAVE SHAPE PREDICTION IN COMPLEX COASTAL SYSTEMS

Dissertation

for the purpose of obtaining the degree of doctor
at Delft University of Technology,
by the authority of prof. dr. ir. T.H.J.J. van der Hagen,
chair of the Board for Doctorates,
to be defended publicly on Thursday 22 December 2022, 15:00 o'clock

by

Floris Paul DE WIT

Master of Science in Civil Engineering,
Delft University of Technology, The Netherlands,
born in Leidschendam, The Netherlands.

This dissertation has been approved by the promotors.

Composition of the doctoral committee:

Rector Magnificus,	Chairperson
Prof.dr.ir. A.J.H.M. Reniers	Delft University of Technology, promotor
Dr. M.F.S. Tissier	Delft University of Technology, copromotor
Independent members:	
Prof.dr.ir. S.G.J. Aarninkhof	Delft University of Technology
Prof.dr. B.G. Ruessink	Utrecht University
Prof.dr.ir. J.A. Roelvink	IHE Delft Institute for Water Education
	Delft University of Technology
Dr.ir. M. Zijlema	Delft University of Technology
Dr. F. Floc'h	Université de Bretagne Occidentale, France

This work is part of the research program 'Collaboration Program Water' with project number 14489 (SEAWAD), which is (partly) financed by NWO Domain Applied and Engineering Sciences.

Keywords: wave shape, bound wave height, bispectrum, triads, BWE model

Printed by: Ridderprint

ISBN 978-94-6384-400-0

An electronic version of this dissertation is available at
http://repository.tudelft.nl/.

CONTENTS

Summary vii

Samenvatting ix

1 Introduction 1
1.1 Background and problem description. . . . 1
1.2 Aim and approach 5

2 Characterizing wave-shape evolution on an ebb-tidal shoal 7
2.1 Introduction 8
2.2 Methodology 9
2.3 Results 16
2.4 Discussion 24
2.5 Conclusions. . . . 26
2.A Drifter study 28
2.B Validity Delft3D Model 30

3 The Relationship between Sea-Swell Bound Wave Height and Wave Shape 31
3.1 Introduction 32
3.2 Background 34
3.3 Bound Variance 36
3.4 Data. . . . 38
3.5 Results 42
3.6 Discussion 47
3.7 Conclusions. . . . 54
3.A Accuracy of Bound Wave Height Formulations 56

4 Wave shape from a bound wave evolution model 59
4.1 Introduction 60
4.2 The spectrum, bispectrum and wave shape 61
4.3 Spectral evolution equations for total and bound variance density 63
4.4 Test simulations and model set-up 68
4.5 Results 70
4.6 Discussion 78
4.7 Conclusion 82
4.A Energy conservation SPB 84

5 Field scale application of the wave shape model 85
5.1 Introduction 86
5.2 Methods 86
5.3 Results 89

5.4 Overestimation of the bound wave height over flat bathymetry 93
5.5 Conclusions. 94
5.A Nonlinear interaction coefficients and attenuation with depth of bound components 96

6 Conclusion **101**
6.1 Conclusions. 101
6.2 Outlook 103

References **107**

Summary **124**

Acknowledgements **129**

About the author **133**

List of Publications **135**

SUMMARY

When waves propagate towards the coast, nonlinear interactions occur under the influence of decreasing water depth and variable ambient currents. This changes the initially harmonic wave shape into a nonlinear wave shape due to the presence of bound waves accompanying the freely propagating primary waves. The nonlinear wave shape ranges from skewed waves with steeper crests and flatter troughs to asymmetric waves where the wave front has pitched forward creating a saw-tooth wave shape at breaking. Analogous to the nonlinear surface elevation, also the near-bed orbital wave velocity is nonlinear. This results in a wave-shape driven sediment transport, generally directed in the direction of wave propagation. For accurate predictions of the sediment transport, it is thus important to know the wave shape. This is especially important in complex coastal systems with strong variations in bathymetry where wave-induced sediment transport gradients affect the subsequent morphological evolution. Therefore, this thesis focuses on measuring and modelling of the nonlinear wave shape.

To investigate the spatial and temporal differences in wave shape, a six week measurement campaign was conducted. This was done at the ebb-tidal shoal seaward of the Ameland Inlet, where waves and currents were measured at 10 locations. Averaged over these locations for the full measurement period, the observed wave shape compares really well against the wave shape parameterization of Ruessink et al. (2012). However, when looking at specific instances in space and time, observations can deviate significantly from this parameterization. The largest deviations occur at the shallowest measurement locations and can be attributed to strong variations in wave-breaking, nonlinear energy transfer rate, and spatial gradients in tidal currents. It was found that in these strongly varying conditions, the wave shape is better described as a function of the conditions slightly further offshore than as a function of the local conditions. This is explained by the fact that the wave shape does not respond instantly to changing environmental conditions, but needs some time and space to adapt.

Both the nonlinear wave shape and the bound superharmonic wave height can be calculated from surface elevation or pressure time series using bispectral analysis. A clear relationship is demonstrated between the two by using measured near-bed pressure time series from three different field experiments. This implies that information on the spatially varying bound wave height can be used to better predict the nonlinear wave shape. One way to predict the bound superharmonic wave height is by applying equilibrium second order wave theory to measured frequency-directional wave spectra. It is shown that this works well in relatively deep water, provided conditions are not too nonlinear. However, in relatively shallow water, the mismatch between observed and predicted bound wave height increases significantly due to wave breaking, strong currents, and increased wave nonlinearity. This is explained by the fact that an equilibrium theory does not hold under rapidly changing conditions.

An alternative to using equilibrium second order wave theory to predict the bound

superharmonic wave height is to use a spectral wave model. Such a model resolves the action balance equation to predict the evolution of the frequency-directional spectrum over a variable bathymetry. The energy transfer towards the bound superharmonics is already included in spectral wave models by the nonlinear triad source term. In this thesis an extension is presented that keeps track of the amount of energy that has been transferred to the superharmonics by the triad interactions and resolves the evolution of these bound harmonics. This extension is called the Bound Wave Evolution (BWE) model. The resulting spatial distribution of the bound wave height can serve as a proxy for the nonlinear wave shape. The accuracy of the BWE model is highly dependant on the triad source term. Therefore, the capabilities of two commonly-used triad source terms (LTA and SPB) to capture the growth of the bound wave height are evaluated after careful calibration. Using these source terms, the BWE model is well capable of predicting the nonlinear wave shape in the shoaling zone, where the bound wave energy is dominated by triad wave interactions. In the surf zone, however, where a combination of triads and wave breaking controls the spectral evolution, the nonlinear wave shape is overestimated. Overall, the SPB method is more accurate but comes at a higher computational cost.

The BWE model is finally applied to predict wave shape evolution seaward of the Ameland ebb-tidal delta. The modeled wave shape is compared to the field measurements and to two wave shape parameterizations. On the seaward slope of the ebb-tidal delta and on the shoal, the BWE model provides an accurate estimate of the wave shape. However, beyond this region, where depth is increasing after the shoal, further research is required to accurately predict the wave shape. This further research involves a better representation of the source terms for triads, breaking and the release of higher harmonics when the depth is constant or increasing.

In conclusion, it is shown that resolving the bound energy evolution equation is a promising way to predict the spatial evolution of the nonlinear wave shape in complex coastal systems.

SAMENVATTING

Golven die naar de kust toe lopen worden beïnvloed door een afnemende waterdiepte en veranderende stroomsnelheden. Hier zorgen niet-lineaire interacties ervoor dat secundaire golven gebonden worden aan de primaire vrije golven. Hierdoor verandert de initieel harmonische golfvorm in een niet-lineaire golfvorm. Dit uit zich in gepiekte golven met stijlere toppen en vlakkere dalen en asymmetrische golven waarbij de golftop voorover helt vlak voordat de golf breekt.

Zes weken aan veldmetingen zijn gedaan om de ruimtelijke en tijdsafhankelijke variaties in golfvorm te onderzoeken. Dit is gedaan met tien meetpunten zeewaarts van het Amelander Zeegat waar golven en getij stroming elkaar tegen komen. De gemeten golfvorm van alle meetpunten over de gehele meetperiode komt goed overeen met de golfvorm parameterizatie van Ruessink et al. (2012). Maar wanneer naar specifieke momenten of locaties gekeken wordt, kunnen de metingen flink afwijken van de parameterizatie. De grootste afwijkingen gebeuren bij de ondiepe meetpunten en kunnen toegeschreven worden aan sterke variaties in golfbreken, niet-lineaire interactie sterkte en getijstroming. Het bleek dat de golfvorm in deze sterk veranderende omgeving beter voorspelt wordt door parameters die wat verder zeewaarts verkregen zijn dan lokale parameters. Dit komt waarschijnlijk doordat de golven zich niet direct aan kunnen passen aan de veranderende omstandigheden maar wat meer tijd nodig hebben.

Zowel de niet-lineaire golfvorm als de gebonden superharmonische golfhoogte kunnen verkregen worden door bispectrale analyse toe te passen op wateroppervlak of druk tijdseries. Metingen van drie verschillende locaties laten een duidelijke relatie tussen deze golfvorm en gebonden golfhoogte zien. Dit impliceert dat ruimtelijke informatie over de gebonden golfhoogte gebruikt kan worden om de niet-lineaire golfvorm te voorspellen. Een manier om de gebonden golfhoogte te verkrijgen is door evenwicht tweede orde golftheorie toe te passen op golfspectra. Zolang de condities niet te niet-lineair zijn en het in relatief diep water is werkt dit heel aardig. Maar in ondieper water vergroot de afwijking tussen metingen en tweede-orde voorspelde gebonden golfhoogte. Dit ligt er aan dat een tweede orde evenwichtstheorie gebruikt wordt terwijl de condities snel veranderend zijn.

In plaats van tweede orde evenwichts golftheorie te gebruiken voor het voorspellen van de gebonden golfhoogte kan ook een spectraal golf model gebruikt worden. Een dergelijk model lost de actie balans vergelijkingen op om de evolutie te voorspellen van frequentie-richting spectra over een variërende bodem. De energie overdracht naar de gebonden superharmonische componenten is al opgenomen in zulke modellen middels de niet-lineaire triad bronterm. In dit proefschrift wordt het BWE-model gepresenteerd, een model uitbereiding die bijhoudt hoeveel energie er al door de triads naar de hogere harmonische is verplaatst en die vervolgens de voortplanting van de componenten oplost. Hieruit kan de ruimtelijke verdeling van de gebonden golfhoogte verkregen worden, die gebruikt kan worden als een benadering voor de niet-lineaire golfvorm. Omdat de accu-

raatheid van het BWE model sterk afhankelijk is van de triad bronterm, is de prestatie van twee veelgebruikte triad brontermen (LTA en SPB) om de gebonden golfhoogte te voorspellen onderzocht. Na kalibratie van deze brontermen is het BWE model goed in staat de niet-lineaire golfvorm in de shoaling zone te voorspellen, waar de gebonden golf energie gedomineerd wordt door triad interacties. In de brandingszone, waar een combinatie van triads en golfbreken de spectrale ontwikkeling bepaalt, wordt de niet-lineaire golfvorm overschat. In het algemeen, geeft de SPB methode een betere voorspelling, maar dit gaat wel ten koste van hogere rekentijd.

Als laatste is het BWE model toegepast om de golfvorm veranderingen zeewaarts van de Amelander eb delta te voorspellen. De gemodelleerde golfvorm is vergeleken met de veldmetingen en twee golfvorm parameterisaties. Het BWE model levert een accurate voospelling van de golfvorm op de zeewaartse vooroever en bovenop de eb delta. In het gebied hierna daarentegen, waar het weer dieper wordt, is meer onderzoek nodig om de golfvorm goed te kunnen voorspellen. Dit vervolgonderzoek bestaat uit verbeterde brontermen voor triads, golfbreken en het loslaten van hogere harmonische componenten wanneer de diepte constant is of toeneemt.

Concluderend laat dit proefschrift zien dat het oplossen van de gebonden golfenergie vergelijking een veelbelovende manier is om de ruimtelijke veranderingen in niet-lineaire golfvorm te voorspellen in complexe kustsystemen.

1

INTRODUCTION

1.1. BACKGROUND AND PROBLEM DESCRIPTION

Due to sea-level rise, subsidence and other human interventions, the coastline of the Netherlands is retreating (Mulder, 2000; Ranasinghe & Stive, 2009; Katsman et al., 2011). To cope with this, the country's policy is to keep the sand volume in the coastal system constant (Rijkswaterstaat, 1990). This is done by applying sand nourishments, to ensure the land area does not decrease and is protected against storm events (Kabat et al., 2009). Over the years a gradual trend is observed from beach nourishments (Dean, 2002; Hanson et al., 2002) towards shoreface nourishments (Hamm et al., 2002; Grunnet & Ruessink, 2005), and more recently to mega nourishments (Stive et al., 2013; de Schipper et al., 2016; Luijendijk et al., 2017; Kroon et al., 2022; Brand et al., 2022).

Apart from the straight coastline, the intertidal Wadden Area in the north of The Netherlands is an area of concern from the view point of sediment losses (van der Spek, 2018). Here a series of barrier islands is located[1], alternated by tidal inlets, separating the North Sea from the intertidal Wadden Sea (see Fig. 1.1). In specific, the sediment volume of the ebb-tidal deltas (shallow areas seaward of the tidal inlets) is decreasing because of two reasons. Firstly, the aforementioned relative sea-level rise. And secondly, due to the artificial closure of the Southern Sea into Lake IJssel and the Wadden Sea by the construction of a large closure dam (Wang et al., 2018). This closure in combination with relative sea-level rise distorted the balance between the tidal prism and the channel depths which is compensated by a net import of sediment into the tidal basin to fill the tidal channels (Elias et al., 2003; Wang et al., 2012). Ebb-tidal deltas serve the important function of protecting the back barrier basin against incoming storms as well as being a sediment source for the beaches of the adjacent islands (Pearson et al., 2020; Elias et al., 2019). Furthermore the deltas are important ecological features containing a rich variety of macro benthic species (Holzhauer et al., 2022). In order to preserve these functions and features in the future, it is proposed to apply mega nourishments on the ebb-tidal deltas. Before doing so, it is

[1] Note that the Wadden area extends until Germany and Denmark, but the focus here is on the Dutch part.

1

Figure 1.1: The location of the Ameland Inlet, separating the barrier islands of Ameland and Terschelling, indicated with a red box on the map of the Netherlands. The Ameland inlet is the tidal inlet analysed in this thesis.

important to predict the evolution of such a nourishment.

In order to predict the long-term effect of an artificial intervention, such as a mega nourishment, commonly process-based morphological evolution models are applied (e.g., de Vriend et al., 1993; Cayocca, 2001; Ojeda et al., 2008; Kristensen et al., 2010). The predictive skill of such models depends on the extent to which the physical processes that play a role in the area are resolved. For the tidal inlets between the Wadden Islands, the dominant processes are wind-generated waves and tides (Sha, 1989; Elias & van der Spek, 2006). Waves come in from the northwestern directions, typically with a wave period of 5-12 s, and the tidal flow has a semi-diurnal character which means the period is approximately 12 h (Elias et al., 2019; Lenstra et al., 2019; van Prooijen et al., 2020). As the timescale of the waves is so small in comparison with the tide and the lifespan of a nourishment, it is unfeasible to resolve all individual waves. Therefore the effect of waves on the evolution of underwater topography is accounted for by wave-averaged models. Traditionally, the role of waves was assumed to be stirring up the sediment after which it is horizontally transported by the currents (Bijker, 1967; Bailard, 1981). Whereas the stirring up of sediment is well represented by wave-averaged parameters (Van Rijn et al., 2004; Grant & Madsen, 1979; Fredsøe, 1984; Soulsby et al., 1993), also intra-wave processes, which are not resolved by wave-averaged models, influence the sediment transport (Watanabe & Isobe, 1991; Madsen & Grant, 1977; Watanabe & Sato, 2005; Bosboom & Klopman, 2001). Amongst these intra-wave processes is the sediment transport caused by the nonlinearity of the near-bed velocity signal, which is closely related to the nonlinear wave shape (King Jr, 1991; Miles, 2013; Gonzalez-Rodriguez & Madsen, 2007; Nielsen, 1992; Henriquez et al., 2014). This type of sediment transport is referred to in literature as wave-induced sediment transport, intra-wave sediment transport, or wave-shape induced sediment transport. This mode of transport is important for the evolution of beach

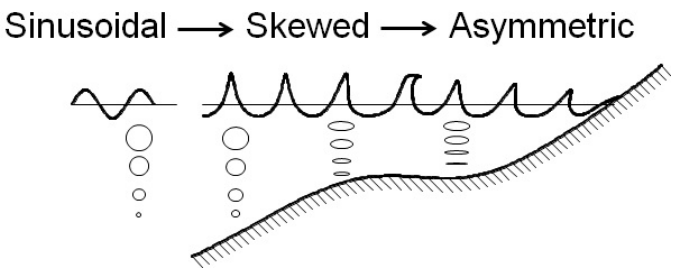

Figure 1.2: Sketch of wave shape evolution and corresponding orbital velocities from deep water towards the coast (from Abreu, 2011)

morphology (Miles, 2013; Roelvink & Stive, 1989; Reniers et al., 2004) and bar migration (Elgar et al., 2001; Hoefel & Elgar, 2003; Gallagher et al., 1998; Ruessink et al., 2007). Furthermore, it has been shown by both Chen et al. (2015) and Reniers et al. (2019) that this contribution of the wave shape to the total sediment transport can be dominant in stormy conditions over an ebb tidal delta, hence when large bathymetric changes are expected.

When waves propagate towards shallower water, the waves transform into a nonlinear shape (Elgar & Guza, 1985), visualized in Figure 1.2. First, the crests get steeper and shorter with longer and flatter troughs, which is referred to as skewed waves (Stokes, 1880). Analogous to the surface elevation, the associated near-bed velocity is stronger beneath the crest than between the trough of those waves (Freilich & Guza, 1984). With the near-bed sediment transport proportional to the mean cubed velocity $\langle u^3 \rangle$, this results in a net onshore sediment transport (Ribberink & Al-Salem, 1994). Subsequently, when the waves propagate further and are close to breaking, they get a pitched forward, sawtooth alike wave shape (Svendsen et al., 1978), called asymmetric waves. The near-bed velocity signal associated with asymmetric waves has a similar velocity beneath the crest and the trough, leading to $\langle u^3 \rangle = 0$. Below the steep front of the wave, however, the velocity is rapidly accelerated from maximum offshore to maximum onshore (Drake & Calantoni, 2001; Nielsen, 2006). This enhanced acceleration leads to horizontal pressure gradients (Drake & Calantoni, 2001) and an increase in bottom shear stress (Nielsen, 1992; Henriquez et al., 2014), both resulting in an onshore sediment transport (Hsu & Hanes, 2004; Calantoni & Puleo, 2006; van der A et al., 2010; Silva et al., 2011). So both skewed and asymmetric waves can contribute to a net onshore sediment transport. In literature skewness and asymmetry are sometimes referred to as velocity skewness and acceleration skewness, respectively. To avoid confusion, this thesis refers to them as skewness and asymmetry.

Most of the present understanding on wave-shape induced sediment transport originates from cross-shore modelling studies on sandbar migration. From observations it is known that bar migration is offshore during highly energetic storm periods and onshore during the calmer periods in between (Sallenger Jr et al., 1985). The offshore bar migration during storms is quite well understood to be caused by the strong undertow caused by energetic waves (Thornton et al., 1996; Gallagher et al., 1998). Although it was suspected that the wave-shape induced sediment transport was responsible for the onshore bar migration during calmer periods (Dubois, 1988; Osborne & Greenwood, 1992), initial attempts using nearshore bed load transport models based on the energetics approach, in which

the sediment transport is proportional to the velocity moments including $\langle u^3 \rangle$ (Bagnold, 1966; Bowen, 1980; Bailard, 1981), did not satisfactory reproduce the onshore bar migration (Roelvink & Stive, 1989; Wright et al., 1991; Thornton et al., 1996; Gallagher et al., 1998; Rakha et al., 1997). This was hypothesized to be because this approach ignores the influence of asymmetry while the effect of skewness was included (Elgar et al., 2001; Drake & Calantoni, 2001). Hoefel & Elgar (2003) showed onshore bar migration by using an energetics approach sediment transport model forced by the wave asymmetry. However, Henderson et al. (2004) demonstrated that by accounting for the phase shift within the wave boundary layer, thereby transforming the free-stream asymmetry into near-bed skewness, could also explain the observed onshore bar migration. This was subsequently supported by the modeling studies of Hsu et al. (2006), provided that a different bed shear stress was applied for the current and wave-induced sediment transport, and by Ruessink et al. (2007) using a skewed-only wave-induced bed shear stress. Findings from these former studies are confirmed by Fernández-Mora et al. (2015), who also show that the shoaling zone is dominated by skewness induced transport whereas the inner surf zone is dominated by asymmetry induced transport. Recently, Boechat Albernaz et al. (2019) showed a significant improvement of morphological evolution on the decadal timescale by applying a parametrization including both skewness and asymmetry (Ruessink et al., 2012) instead of a skewness only parameterization (Isobe & Horikawa, 1982).

There are a number of significant differences between a barred coastline and an ebb-tidal delta. Firstly, the absence of a fixed coastline closely behind the ebb delta will decrease the magnitude of the undertow during stormy conditions, potentially increasing the relative importance of wave-shape induced sediment transport. This might partially explain why ebb-tidal shoals eventually attach to the downdrift island. A second difference is the role of tidal currents. Although they can be present at a barred coast, they are commonly alongshore directed with small gradients in alongshore direction. This results in small net transport because the updrift and downdrift sediment transport will be comparable. Furthermore, the effect on wave dynamics is negligible as the directions of the tidal current and wave propagation are close to perpendicular (de Wit et al., 2017). In contrast, at the complex bathymetry in the vicinity of a tidal inlet, strong gradients in tidal currents lead to regions of erosion and deposition. Besides, the tidal direction is frequently in or against the direction of wave propagation thereby influencing the wave dynamics. Waves propagating against a current will become shorter, higher and more nonlinear (Peregrine, 1976; Hedges et al., 1985; Soulsby et al., 1993; Dodet et al., 2013). Vice versa, waves in the direction of the current will become longer, lower and less nonlinear. A third difference is that the three dimensionality encountered at an ebb-tidal delta is much greater than at a coastline, where the processes can more easily be distinguished in cross-shore and alongshore.

As explained, a proper prediction of the wave shape is crucial for accurately capturing the morphological evolution of complex coastal systems. The current practice in process-based morphological evolution models is to include the effect of the wave shape by means of a local wave shape parameterization (e.g., Isobe & Horikawa, 1982; Doering & Bowen, 1995; Ruessink et al., 2012). This practice, however, has two major limitations:

- The influence of current magnitude and direction are not accounted for in present parametrizations, even though they are known to have significant influence on the

wave shape.

- Local parametrizations depend on local bulk parameters only such as water depth, wave height and period. Intrinsically it is thus assumed that the wave shape is in equilibrium with the local conditions. This means that the validity is questionable in non-equilibrium conditions, for instance under rapid changes in depth or currents (Rocha et al., 2013). Furthermore, other (non-local) environmental parameters are known to affect the development of the wave shape such as the bed slope (De Bakker et al., 2016; Norheim et al., 1998; Filipot, 2015; Chen et al., 2018), spectral shape (Hasselmann, 1962; Norheim et al., 1998; Rocha et al., 2017) and directional distribution (Hasselmann, 1962; Freilich et al., 1990; Salmon et al., 2016). Ignoring these influences will lead to inaccuracies of the predicted wave shape.

1.2. AIM AND APPROACH

This PhD thesis is part of SEAWAD, a scientific research project which ultimate aims is to develop the system knowledge and tools to predict the morphological and ecological effects of mega-nourishments on the ebb-tidal deltas of the Wadden Sea. In order to achieve this, the following four knowledge gaps were identified and addressed in four sub projects:

1. What is the effect of intra-wave processes on sediment transport patterns?
2. What is the influence of bed forms on sediment transport?[2]
3. How does the grain size distribution influence the sediment pathways?[3]
4. How do hydrodynamic and sediment parameters affect the response of benthic communities to nourishments?[4]

This thesis deals with the first sub project. Given that the wave-driven sediment transport is a function of the wave nonlinearity, it is important to first understand this process. Therefore, the aim of this thesis is to improve the accuracy of the nonlinear wave shape prediction in complex coastal systems (such as the Ameland ebb-tidal delta). The computational demand of this predictive tool should be limited such that it is applicable in long-term morphological models. A combination of field data measurements, data analysis techniques and numerical modelling is applied to achieve this aim.

Chapter 2 explores the nonlinear wave shape measurements from the SEAWAD field campaign (van Prooijen et al., 2020). The measured wave shape is compared against the commonly used parameterization of Ruessink et al. (2012) to investigate its performance for varying locations and conditions. The findings of this chapter serve as a basis for the further research of this thesis. In Chapter 3, bispectral analysis of the same data set shows that there is a clear relationship between the wave shape and the bound wave height. This relationship is found not to be site specific as the same is found for two other data sets at Egmond, The Netherlands (Ruessink et al., 2001; Van Rijn et al., 2002) and Duck, USA (Birkemeier et al., 1997; Reniers et al., 2004). These findings open a pathway for Chapter

[2] For the findings within this sub project, see: Brakenhoff et al. (2019, 2020a,b); Brakenhoff (2021).
[3] For the findings within this sub project, see: Pearson et al. (2020, 2021b,a, 2022); Pearson (2022).
[4] For the findings within this sub project, see: Holzhauer et al. (2020, 2022).

4, in which an evolution equation for the bound wave harmonics is added to the spectral wave model SWAN. From these bound wave harmonics, the bound wave height and thus the wave shape can be computed. This has the advantage over applying a local parameterization that it accounts for the prior evolution of the wave shape before reaching a certain location, making it more applicable in non-equilibrium conditions. The performance of this model is tested by comparing its bound wave height and wave shape to those obtained from the measurements and parameterizations in Chapter 5. Finally, conclusions and future perspectives are discussed in Chapter 6.

2

CHARACTERIZING WAVE-SHAPE EVOLUTION ON AN EBB-TIDAL SHOAL

ABSTRACT

Field measurements of waves and currents were obtained at ten locations on an ebb-tidal shoal seaward of Ameland Inlet for a six-week period. These measurements were used to investigate the evolution of the near-bed velocity skewness and asymmetry, as these are important drivers for wave-induced sediment transport. Wave shape parameters were compared to traditionally used parameterizations to quantify their performance in a dynamic area with waves and tidal currents coming in from different directions over a highly variable bathymetry. Spatially and temporally averaged, these parameterizations compared very well to the observed wave shape. However, significant scatter was observed when looking at specific locations or instances in time. The largest deviations from the parameterization were observed at the shallowest locations, where the contribution of wave-induced sediment transport was expected to be the largest. This chapter shows that this scatter was caused by differences in wave-breaking, nonlinear energy transfer rate, and spatial gradients in tidal currents. As a solution, it is proposed to include the prior evolution of the wave before reaching a location in future parameterizations in numerical modeling instead of only using local parameters to predict wave shape.

This chapter is an adapted version from the publication: de Wit, F.P., Tissier, M.F.S. and Reniers, A.J.H.M., (2019), Characterizing Wave Shape Evolution on an Ebb-Tidal Shoal, *Journal of Marine Science and Engineering* 7(10), 367.

2.1. INTRODUCTION

Tidal inlets and their deltas are highly dynamic systems (Hayes et al., 1970; Oertel, 1972). Deep channels are formed by the in- and outgoing tidal currents. Sediment is exchanged through a network of channels between the tidal flats, deltas and adjacent barrier island coasts (Hayes, 1980; Fitzgerald, 1984). At the seaward end of the ebb channel, a relatively shallow area is located, the ebb-tidal delta. It is shaped as a result of the decelerating tidal flow and the influence of waves from offshore. The ebb-tidal delta serves an important role in these systems. During storm conditions, it provides shelter to the back-barrier basin by dissipating high incoming waves. Furthermore, the ecosystem has a high ecological value containing a large variety of benthic species.

According to Finley (1978), morphodynamic development of the ebb-tidal delta depends on the tidal flow and waves approaching from offshore. Traditionally, it was considered that waves stir up the sediment, which is then transported by the currents (Grant & Madsen, 1979). However, as stated by Nielsen (1988), wave-induced sediment transport itself can be of significant influence, even in presence of strong currents. Properly accounting for wave-induced sediment transport in process-based numerical models (e.g., Lesser et al., 2004; Warner et al., 2008) is of high importance to represent bar formation along a straight coast. In a more complex environment, such as a tidal inlet, the evolution of the ebb tidal shoal and delta is formed by the wave-induced sediment transport. A model study by Chen et al. (2015) concluded that morphological changes at the ebb-tidal delta are dominated by wave-induced sediment transport, where the other surroundings are dominated by the current-induced sediment transport.

Nonlinearity of the near-bed velocity is an important parameter determining the wave-induced sediment transport (Hoefel & Elgar, 2003). Nonlinear wave shape can be defined as the skewness (vertical asymmetry) and asymmetry (horizontal asymmetry) of a time series (Elgar & Guza, 1985). The initial sinusoidal wave shape, as occurs in deep water far away from the coast, becomes nonlinear when moving into shallower water. First, it transforms in a skewed shape with short peaked crests and long flat troughs. Due to the faster propagation of the crest with respect to the trough, waves become pitched forward resulting in an asymmetrical wave shape. Eventually, as the waves become more and more asymmetric and break, skewness decreases. Analogous to gradients in depth, gradients in coastal currents result in wave shape changes. Wave skewness and asymmetry are intra-wave properties, which are not resolved in the wave-averaged models that are used to drive morphodynamic models. Therefore, it is essential to have an accurate parameterization to include their contribution to the total sediment transport. A recent study has shown that properly parameterizing the near-bed velocity substantially improves morphodynamic predictions on the decadal time-scale (Boechat Albernaz et al., 2019).

The first sediment transport models including the effects of velocity skewness were developed by Stive (1987) and Roelvink & Stive (1989). The importance of adding velocity asymmetry was shown by Drake & Calantoni (2001). Doering & Bowen (1995) provided a parameterization of orbital velocity skewness and asymmetry based on field measurements obtained from four beaches. They found a correlation between skewness/asymmetry and the Ursell number, namely $Ur = \frac{3}{4}\frac{A}{k^2 d^3}$, a local nonlinearity parameter based on wave amplitude A, wave number k, and mean water depth d. Although the relationship between bi-amplitude (skewness and asymmetry combined) and the Ursell num-

ber is observable in the shoaling and surf zone, they stated that it is less clear in the surf zone. In a similar study, based on many more data points (34.000 vs. 48), Ruessink et al. (2012) found a similar relationship as a function of the Ursell number. Differences between the two parameterizations are only significant for $Ur > 3$. Rocha et al. (2013) compared available nonlinearity parameterizations based on field experiments and state that the Ruessink et al. (2012) parameterization can predict skewness and asymmetry on low-sloping beaches for specific wave conditions, but that it does not work as well for steeper beaches and longer wave periods. In a follow-up study, Rocha et al. (2017) used a numerical model to conclude that a decreasing offshore wave steepness, decreasing bed slope, and decreasing spectral width all lead to a higher maximum nonlinear wave shape (skewness and asymmetry combined) and different development along the beach profile. Although not included in the previously mentioned parameterizations (Doering & Bowen, 1995; Ruessink et al., 2012), the effects of wave steepness (Dibajnia et al., 2001), spectral bandwidth (Norheim et al., 1998) and bottom slope (Norheim et al., 1998; Dong et al., 2014; Filipot, 2015) on skewness and asymmetry have been shown in previous research.

Several studies (e.g., Doering & Bowen, 1995; Ruessink et al., 2012; Rocha et al., 2017) have investigated the parameterization of the wave shape, most of them have focused on (barred) beaches in the surf zone. It is questionable how applicable these parameterizations are at an ebb-tidal delta for a number of reasons. Firstly, at an ebb-tidal delta the bathymetry is much more complex than for an open coastline with milder alongshore variations, leading to a larger range of incoming directions and spreading. Secondly, tidal currents might play an important role. Tidal currents opposing the direction of wave propagation can lead to decreasing wave length, increasing wave height and eventually even wave breaking (e.g., Groeneweg et al., 2009; Rusu et al., 2011). Therefore, it is likely that tidal currents have an influence on the wave shape. Whereas in coastal waters, tidal currents are often (almost) perpendicular to the wave direction, hence barely affecting the waves (Thornton & Guza, 1982; Tissier et al., 2015), at an ebb-tidal delta, the currents and waves can face each other under any arbitrary angle. Thirdly, depths of the ebb-tidal delta are generally larger than those investigated in previous studies.

In this chapter, we compare near-bed velocity skewness and asymmetry from a new dataset of measurements at an ebb-tidal delta to existing parameterizations. Data were obtained during the CoastalGenesis2/SEAWAD field campaign in September 2017 at the Ameland Inlet, The Netherlands (van Prooijen et al., 2020). In Section 2.2, the field campaign and data-processing techniques are discussed. Temporal and spatial variations in wave shape, their dependence on the Ursell number and the role of prior wave transformation is addressed in Section 2.3. Subsequently, in Section 2.4, we discuss the consequences of the results on sediment transport, and ways to improve future wave shape parameterizations. Concluding remarks are given in Section 2.5.

2.2. METHODOLOGY

2.2.1. FIELD CAMPAIGN

To obtain the system knowledge necessary to plan future sand nourishments in ebb-tidal deltas, a large field campaign was conducted in September 2017 at the Ameland Inlet, the CoastalGenesis2/SEAWAD field campaign (van Prooijen et al., 2020). The Ameland

Inlet is located in the north of The Netherlands, between barrier Islands Ameland and Terschelling. The area is highly dynamic, with combined action of waves and tidal currents. The main tidal channel has depth-averaged currents up to 2 m/s in a maximum depth of 20 m. North of the channel, a shallow sandy area is formed by the deceleration of the diverging ebb tide, the ebb-tidal delta (see Figure 2.1). This area is shaped by the combination of waves and tide. Waves, locally generated in the North Sea, approach the ebb delta from north to northwestern directions. They are short (5–10 s) and very variable in height (0.5–5 m).

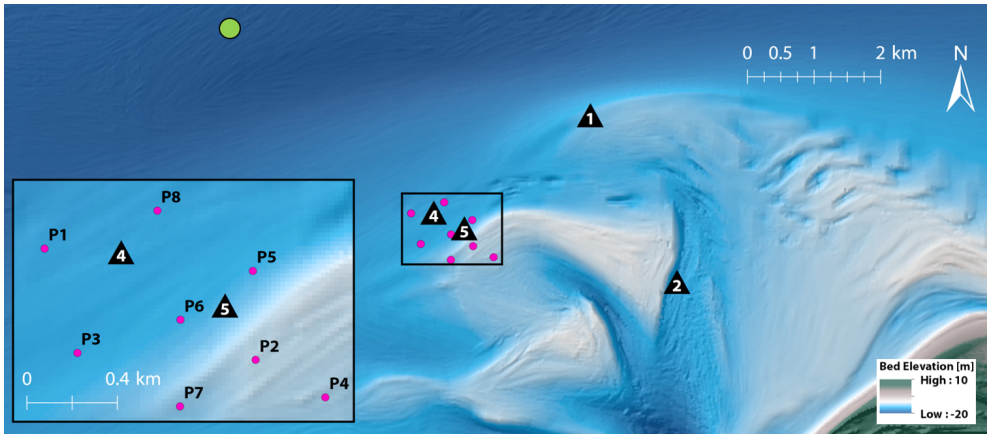

Figure 2.1: Bathymetric map of Ameland ebb-tidal delta with instrument frames (black triangles), pressure sensors (pink circles), and offshore wave buoy (green circle). In the bottom left corner is a zoomed-in map of the ebb-tidal shoal. where most of the instruments were located.

Five instrument frames were deployed for a six-week period, measuring velocities, waves, water levels, sediment concentrations, bed forms, conductivity, temperature and density. Eight pressure sensors surrounded the frames to get more spatial information on waves. Frame and pressure sensor locations are indicated in Figure 2.1. Additionally, drifter measurements and 13-h tidal-inlet discharge measurements were performed. Furthermore, grab samples, box cores, and water samples were obtained to characterize the sediment composition in the bed and water column. For a detailed description of the field campaign, see van Prooijen et al. (2020).

For this study, the focus was on near-bed, high-frequency measurements of velocity and pressure. At the frames (F), this was measured by a downward-looking High-Resolution Acoustic Doppler Current Profilers (ADCP), measuring the velocity profile in the lowest 0.5 m of the water column above the bed and pressure 0.5 m above the bed at a frequency of 4 Hz. The standalone pressure sensors (P) only measured pressure at a frequency of 10 Hz approximately 0.5 m above the bed. To compute the depth-averaged currents, the above-mentioned downward looking ADCPs were used in combination with upward looking ADCPs measuring the velocity profile from 2.3 m above the bed to the free surface at a frequency of 1.25 Hz. Mean water depth, bed slope, instrumentation, and sampling frequency are given in Table 2.1. The bed slope (indicated in Table 2.1) was computed over a distance of 200 m in the mean direction of wave incidence (north-

northwest), in order to reflect the slope the waves encountered before reaching a certain sensor.

Figure 2.2 shows the main bathymetric transect including the positions of the measurement locations. The nine sensors available were grouped into four clusters based on their position on the ebb-tidal delta:

- **Shelf:** P1, P8, F4, and P3. These sensors were at the milder shelf in mean depths between 10.5 and 8 m.
- **Seaward slope:** P5, P7, and F5. These sensors were at the steeper seaward edge of the shoal in mean depths between 8 and 5 m.
- **Shoal:** P2 was at the transition between the seaward slope and the flat top of the shoal.
- **Landward slope:** P4 was at the basin end slope of the shoal. It was 300 m more landward than P2 in a region where the depth starts increasing after the shallowest point, which was located between P4 and P2.

Table 2.1: Overview of instruments, their location, the mean depth and bed slope they were in, and the sampling frequency they operated in.

Cluster	Location	Depth (m)	Bed Slope (-)	Instrument	Frequency (Hz)
Shelf	P1	10.4	0.004	PS	10
	P8	9.5	0.004	PS	10
	F4	8.5	0.004	ADCP down	4
				ADCP up	1.25
	P3	8.2	0.002	PS	10
Seaward slope	P5	7.9	0.005	PS	10
	F5	6.6	0.006	ADCP down	4
				ADCP up	1.25
	P7	5.3	0.009	PS	10
Shoal	P2	4.3	0.011	PS	10
Landward slope	P4	4.6	−0.002	PS	10
Other	F1	6.6	0.009	ADCP down	4
				ADCP up	1.25

During the field campaign, a wide range of conditions were encountered with two storms alternated by calm periods. In Figure 2.3, the conditions throughout the campaign are presented. The offshore wave conditions (Figures 2.3a–c) were obtained from a wave-buoy (green circle in Figure 2.1), and tidal elevation and depth-averaged velocities (Figures 2.3d–f) from the most offshore measurement frame F4. Waves, coming in from the North Sea (northern to western directions), were between 0.5 and 5 m. Two storms occurred, with significant wave heights up to 5 m. Due to limited fetch, wave periods were

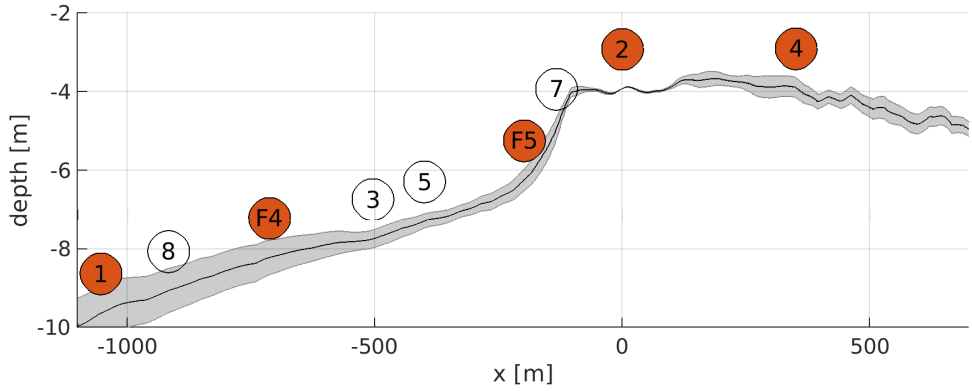

Figure 2.2: Main bathymetric transect (black line), including the standard deviation in depth (grey area). This standard deviation was computed over 91 transects with the same length as the main transect rotated through a fixed point at P2 between −45° and +45° from the main transect to visualize the three-dimensionality of the area. Sensor locations are indicated in a red circle if they were on the main transect and in a white circle if they were not on the main transect. The pressure sensors that were not on the main transect were placed such that they were at the depth at which they were located.

generally short, 6–8 s, with peaks to 10 s during the second storm. Water levels varied with a tidal range of 2.6 m. Additionally, a storm surge of up to 1 m was observed. At the seaward slope of the ebb-tidal delta, the tidal velocities ranged from 0.5 m/s towards southeast during flood to 0.5 m/s northwest during ebb. During the first storm, an outflow exceeding 1 m/s was observed, probably related to wind-driven outflow from the Wadden Sea basin (van Weerdenburg, 2019).

2.2.2. DATA PROCESSING

All instruments operated in burst mode, with bursts of 30 min. The way the signals were processed in time-averaged quantities is described in this subsection.

VELOCITY

High-resolution (4 Hz) profile measurements of velocity were obtained 0.5 m above the bed by the downward-looking ADCPs. Additionally, lower resolution (1.25 Hz) profile measurements were obtained above the frame, from 2.3 m above the bed to the water surface. All velocity signals were filtered based on correlation (Elgar et al., 2005), despiked (Goring & Nikora, 2002; Mori et al., 2007), and converted to an East–North–Up reference frame. Depth-averaged currents were computed from the upward- and downward looking ADCP profiles (with the gap between the two instruments linearly interpolated), and characterized by a mean current magnitude U and direction θ_U.

PRESSURE

Water pressure p was obtained by subtracting the air-pressure p_{air} from pressure signals p_{tot} measured by the ADCPs (locations F4 and F5) and pressure sensors (P1-P8). Mean water depth was calculated using $d = z_p + \langle p \rangle / \rho g$, in which z_p is the height of the pressure sensor above the bed, $\langle p \rangle$ is the burst averaged pressure, ρ is the water density and g is

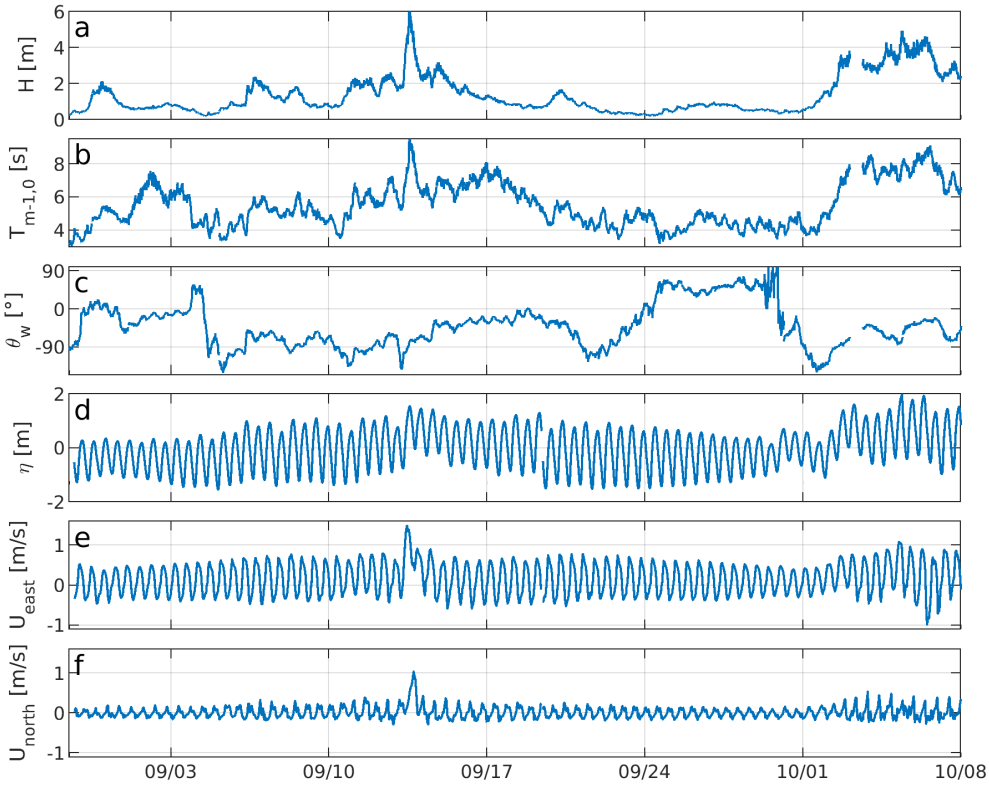

Figure 2.3: Overview of half-hourly averaged conditions during the KG2/SEAWAD field campaign from 29 August to 10 October: (**a**) Significant wave height; (**b**) mean spectral wave period; and (**c**) mean direction are obtained from the offshore wave-buoy. (**d**) Mean surface elevation and depth-averaged velocity in (**e**) east and (**f**) north directions were obtained from the most offshore measurement frame, F4.

the gravitational acceleration. The surface elevation η was reconstructed by using a frequency dependent correction factor, based on linear wave theory, accounting for pressure attenuation over depth. Significant wave height $H = 4\sqrt{m_0}$ and period $T_{m-1,0} = m_{-1}/m_0$ were obtained by applying spectral analysis on the surface elevation in the short-wave frequency range (0.05–0.3 Hz), in which m_j is the spectral moment of order j. Additionally, 2D spectral analysis was performed on surface elevation, eastward and northward velocity time series in the same frequency range to obtain the mean wave direction θ_w and spreading σ_{θ_w}. Wave number k was computed by iteratively solving the linear dispersion relationship:

$$\omega = \sigma + kU_n = \sqrt{gktanh(kd)} + kU_n \tag{2.1}$$

with absolute frequency $\omega = 2\pi/T_{m-1,0}$, relative frequency σ, and U_n the depth-averaged current in direction of wave propagation, which can be computed from U, θ_U, and θ_w. The estimation of depth-averaged currents, which are required to compute k for locations P1–P8, where velocity measurements were not available, is described in Section 2.2.3.

CALCULATION OF NONLINEAR PARAMETERS

Wave skewness, asymmetry and the Ursell number were derived from time series of pressure and velocity. To only consider the short-wave contribution, a frequency filter of 0.05–0.3 Hz was applied to the time series. For the first analysis (Section 2.3.1), the dimensional skewness and asymmetry was used, because it is reflective of the amount of wave-induced sediment transport. They were computed as:

$$\widetilde{Sk}_q = \langle q^3 \rangle \tag{2.2}$$

$$\widetilde{As}_q = \langle \mathscr{H}\{q\}^3 \rangle \tag{2.3}$$

where q is the filtered time series of a quantity, which can be either velocity or pressure, $\mathscr{H}\{...\}$ denotes the imaginary part of the Hilbert transform, and $\langle ... \rangle$ indicates time averaging over the burst. To compare our dataset to previous field campaigns and parameterizations, skewness and asymmetry were also presented in the conventionally used dimensionless form:

$$Sk_q = \frac{\langle q^3 \rangle}{\langle q^2 \rangle^{3/2}} \tag{2.4}$$

$$As_q = \frac{\langle H\{q\}^3 \rangle}{\langle q^2 \rangle^{3/2}}. \tag{2.5}$$

As the measured skewness and asymmetry were compared to the Ur-based parameterization introduced by Ruessink et al. (2012), the Ursell number was estimated exactly as in this chapter, i.e.,

$$Ur = \frac{3}{4} \frac{A}{k^2 d^3}, \tag{2.6}$$

with wave amplitude $A = H/2$, k calculated with Equation (2.1) using $T_{m-1,0}$ as a period estimate, and d the mean depth.

ESTIMATION OF NEAR-BED VELOCITY TIME SERIES FROM PRESSURE SIGNALS

Near-bed velocity data were only available at three locations, in mean water depths between 7 and 10 m. To extend our dataset to a larger depth range, between 4 and 12 m, near-bed orbital velocities were also estimated from the pressure time series measured by the standalone pressure sensors P1–P8. The near-bed orbital velocity signal is computed from the pressure signal using linear wave theory. This is done by applying a Fast-Fourier-Transform on the pressure timeseries, subsequently multiplying the near-bed pressure complex amplitudes with the frequency dependant correction factor $K_{lin}(\sigma) = \frac{\sigma}{\rho g tanh(kd)}$ to estimate the near-bed velocity spectrum. The near-bed velocity signal $u_{p2u}(t)$ is then retrieved by performing an inverse Fast-Fourier-Transform. The subscript $p2u$ refers to the fact that the velocity is derived from the pressure using the steps above.

To verify this method, reconstructed velocity skewness and asymmetry were compared to directly measured velocity skewness and asymmetry at the measurement frames (Figure 2.4). For F4, the method systematically over predicts skewness (red data points in Figure 2.4), which is also reflected in a Root-Mean-Squared-Error (RMSE) of 0.12. For F1 (RMSE = 0.06) and F5 (RMSE = 0.07), skewness is very well predicted. Not a lot of asymmetry was observed at the measurement frames, and a similar error (RMSE = 0.04) was found for all three frames.

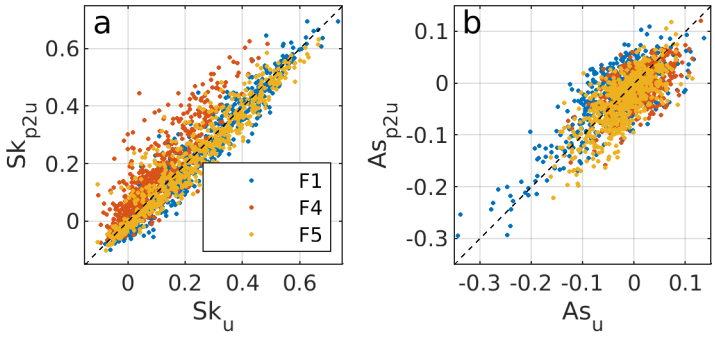

Figure 2.4: Correlation between (**a**) skewness and (**b**) asymmetry directly measured from the near bed velocity (Sk_u and As_u) and from reconstructed near-bed velocity (Sk_{p2u} and As_{p2u}) at measurement Frames 1 (blue), 4 (red), and 5 (yellow). The black dashed line is unity.

2.2.3. DEPTH-AVERAGED CURRENTS

At locations P1–P8, the currents were not measured. These were, however, needed to solve the dispersion relationship (Equation (2.1)). Due to the complex bathymetry, the current field exhibits strong spatial variations over the domain of interest (see also the exploratory drifter study in Appendix 2.A). Hence, the currents from the frames cannot directly be used at the pressure sensors. Therefore, an estimate of burst averaged currents at these locations was provided by a Delft3D simulation of the campaign, including the effects of wind, waves and tide for the duration of the field campaign. The setup and details of the numerical model are described in Nederhoff et al. (2019), and the validity in predicting the correct magnitude and direction of the currents is shown in Appendix 2.B by comparing predicted and measured depth-averaged currents at F1, F4, and F5.

The importance of including time-averaged currents in the dispersion relationship is related to the magnitude of kU_n compared to the magnitude of σ. The importance is thus higher for shorter waves and larger tidal currents in or against direction of wave propagation. Because of mass continuity, largest currents were observed at the shallowest location, P2, which was therefore the location where the effect of the current on waves was expected to be most noticeable. At this location, when not including currents, the average and maximum error for k was 6% and 33%, respectively. Since k was also included in the conversion from pressure to surface elevation (Section 2.2.2) and near-bed orbital velocity (Section 2.2.2), the aforementioned error in k influenced σ, A, Ur, Sk_{p2u}, and As_{p2u} with maximum errors of 20%, 12%, 38%, 3%, and 3%, respectively. The error introduced by not including currents is visualized in Figure 2.5, which clearly shows that A, Sk_{p2u}, and As_{p2u} were barely influenced, whereas k, σ, and Ur changed significantly when including the currents.

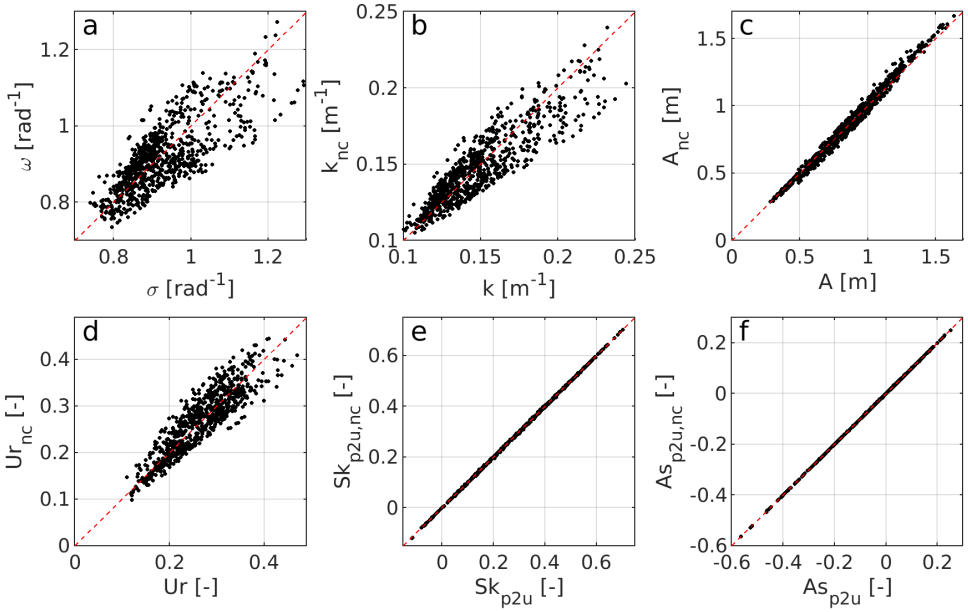

Figure 2.5: Error estimate of wave parameters at P2 when not taking into account currents in the dispersion relationship. (**a**) Frequency; (**b**) wave number; (**c**) amplitude; (**d**) Ursell number; (**e**) skewness; and (**f**) asymmetry while not taking into account the current (subscript nc) are plotted as a function of the same parameters but taking into account the current. The red dashed lines represent unity.

2.3. RESULTS

2.3.1. DATA OVERVIEW AND SELECTION

Significant wave height H, dimensional skewness $\widetilde{Sk}_{p2u}$ and asymmetry $\widetilde{As}_{p2u}$ at the deepest (P1, d = 10.4 m) and shallowest (P2, d = 4.3 m) locations, are presented in Figure 2.6. The magnitudes of $\widetilde{Sk}_{p2u}$ and $\widetilde{As}_{p2u}$ are highly variable in time (Figure 2.6b,c). The largest absolute values were mainly observed in stormy periods at 13 September and 3–7 October, where $H > 2$ m. Depth-induced shoaling generally leads to slightly increasing wave heights between P1 and P2, apart from the two storms in which wave breaking leads to a decrease in wave height (Figure 2.6a). It can be seen that $\widetilde{Sk}_{p2u}$ increases while moving to the shallower sensor, and a clear tidal pattern can be seen in the $\widetilde{Sk}_{p2u}$ during the second storm. Large values of $|\widetilde{As}_{p2u}|$ occur when conditions are close to wave breaking or once the waves are breaking. This explains why near-zero $\widetilde{As}_{p2u}$ was observed at P1, but that waves get asymmetric at P2.

For the following analyses, the focus was on cases with considerable $\widetilde{Sk}_{p2u}$ and $\widetilde{As}_{p2u}$ for two reasons: first because this reflects when wave-induced sediment transport occurs, and second to prevent nonphysically high values of dimensionless skewness and asymmetry when $\langle u^2 \rangle^{3/2}$ is really small. $\widetilde{S}_{p2u} = \sqrt{\widetilde{Sk}_{p2u}^2 + \widetilde{As}_{p2u}^2}$, a combined nonlinear parameter, calculated at the most nonlinear location P2, was used to determine which cases to include. The threshold was set such that 99% of cumulative nonlinearity $\widetilde{S}_{p2u}$ was taken

into account in the following, which was caused by only 42% of the bursts. Eventually, 813 half-hourly bursts were selected (see shaded areas in Figure 2.6), i.e. 17 days of unique data in which significant $\widetilde{Sk}_{p2u}$ and $\widetilde{As}_{p2u}$ are present.

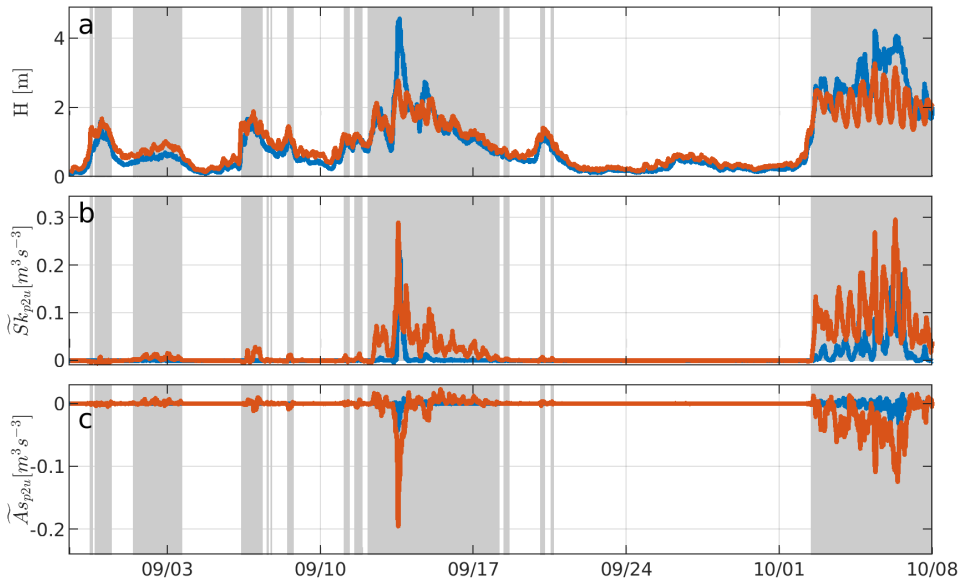

Figure 2.6: Time series of: (**a**) spectral wave height; (**b**) dimensional skewness; and (**c**) dimensional asymmetry at sensor P1 (blue) and P2 (red). The shaded grey area indicates waves which are taken into account as a result of the nonlinearity threshold on $\widetilde{S}_{p2u}$.

2.3.2. DEPENDENCE OF WAVE SHAPE PARAMETERS ON THE LOCAL URSELL NUMBER

Traditionally, the Ursell number Ur is used to explain the variations in skewness Sk_u and asymmetry As_u (Doering & Bowen, 1995; Ruessink et al., 2012). For our dataset, Ur ranges from 0 to 0.7, i.e., values similar to those typically found in the shoaling and outer surf zone. In this range, both Sk_u and As_u are expected to increase for increasing Ur, with the increase in As_u starting at higher Ur-values (see parameterization by Ruessink et al. (2012), dotted blue lines in Figure 2.7).

When Sk_{p2u} and As_{p2u} of all locations were combined and binned as a function of their local Ursell number, the results compare remarkably well with the parameterization of Ruessink et al. (2012), as can be seen in Figure 2.7a,b. An almost perfect match was observed between the bin-meaned Sk_{p2u} of all locations and the parameterization. A similar match was found for the As_{p2u} bins at low Ur, but for $Ur > 0.3$ observed As_{p2u} is significantly lower than the parameterized value. Overall, this suggests that, although based on measurements on barred beaches, the parameterization is applicable in a more complex environment such as an ebb-tidal delta. However, it should be noted that the standard deviation per bin is significant with respect to the mean of the bin, which is also reflected by the extensive clouds of data points in Figure 2.7a,b. As shown in the following,

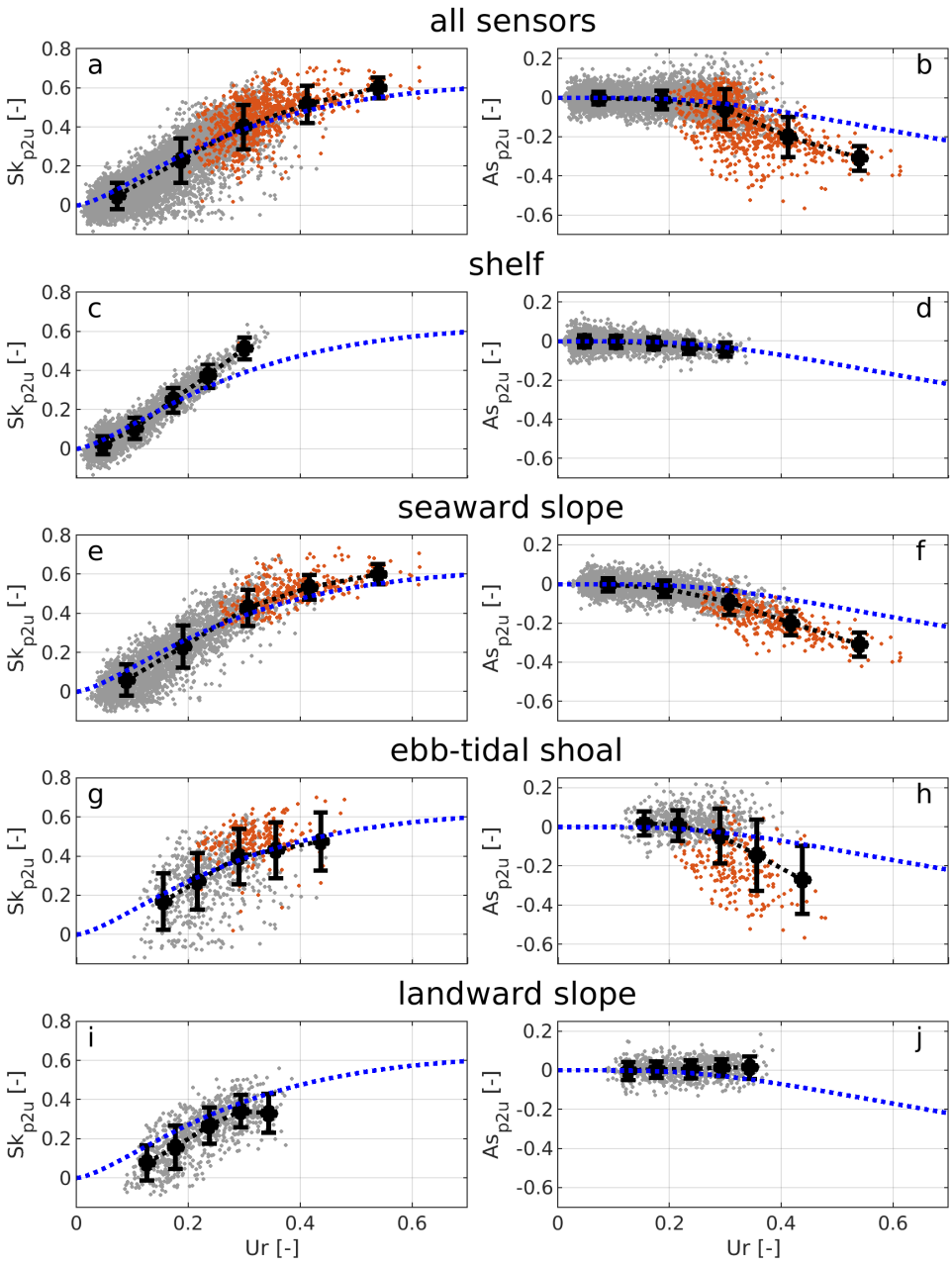

Figure 2.7: Sk_{p2u} (left) and As_{p2u} (right) as a function of Ur at all locations and for different clustered locations (the clusters are as defined in Table 2.1): (**a**,**b**) all sensors combined; (**c**,**d**) the shelf; (**e**,**f**) seaward slope; (**g**,**h**) ebb-tidal shoal; and (**i**,**j**) landward slope. Individual data points, visualized by the dots, are in red when local wave breaking is expected ($G > 0.5$) and grey if no wave-breaking is expected ($G < 0.5$), based on Equation (2.7). Black error bars indicate mean per bin ± one standard deviation. Five equally sized bins are defined between the minimum and maximum observed Ur within each subset of the data. The blue dashed line is the parameterization by Ruessink et al. (2012).

although the wave shape parameters are well predicted by parameterizations depending on Ur for the entire dataset, when considering individual locations or specific wave conditions, the parameterization can systematically under- or overestimate Sk_{p2u} and As_{p2u}.

At the shelf, Sk_{p2u} is fully controlled by Ur (Figure 2.7c), with correlation coefficients R^2 between 0.87 and 0.89 (see Table 2.2). When it gets shallower, two trends can be observed. A larger scatter in Sk_{p2u} was observed at a given Ur, and the slope of the best linear fit between Sk_{p2u} and Ur decreases from the shelf to the seaward slope (Figure 2.7e). On top of the shoal and at the landward slope (Figure 2.7g,i), the correlation between Sk_{p2u} and Ur decreases to 0.28 and 0.13, thus variability in Sk_{p2u} cannot be well described by the variability in Ur.

As_{p2u} is near-zero at the shelf (Figure 2.7d) although Sk_{p2u} is already present (Figure 2.7c), which is as expected for $Ur < 0.3$ (see blue lines in Figure 2.7). The near-zero As_{p2u} at this location explains the low correlation between As_{p2u} and Ur (Table 2.2). At the seaward slope, As_{p2u} starts to develop indicating pitched forward waves, which are breaking or close to breaking (Figure 2.7f). On top of the shoal, high variability in As_{p2u} was observed (Figure 2.7h). There is no clear trend as high $|As_{p2u}|$ occurs for a wide range in Ur between 0.25 and 0.4. Moreover, for this range, cases were also observed where As_{p2u} is near-zero although Ur is up to 0.45. For the bursts with non-zero As_{p2u}, there is a clear difference between the slope of As_{p2u} as a function of Ur at the seaward slope (Figure 2.7f) and the shoal (Figure 2.7h), which leads to an increased scatter when all sensors are combined (Figure 2.7b). At the landward slope, where the depth has slightly increased As_{p2u} is near-zero for the full Ur-range. This behavior was also observed and modeled by Elgar et al. (1997), who found that highly skewed and asymmetric waves can become symmetrical again in increasing water depths.

In summary, although it is slightly underestimating Sk_{p2u} at the shelf and overestimating As_{p2u} at the seaward slope, the parameterization by Ruessink et al. (2012) is capable of predicting Sk_{p2u} and As_{p2u} reasonably well at the shelf and the seaward slope (see dashed blue lines in Figure 2.7c–f). On top of the shoal, the data cloud suggests that no parameterization based on Ur only can properly predict Sk_{p2u} and As_{p2u}. The same holds for Sk_{p2u} at the landwards slope (see dashed blue lines in Figure 2.7g,i). No As_{p2u} was observed behind the ebb-delta, although for higher Ur, some As_{p2u} would be expected based on the parameterization (see dashed blue lines in Figure 2.7j). The fact that observed Sk_{p2u} and As_{p2u} for a given Ur-band (e.g., 0.3–0.4) are very different depending on the location and that large scatter was observed at the shallow locations suggest that more physical processes need to be accounted for than local Ur only.

2.3.3. ROLE OF WAVE TRANSFORMATION

Deviations with respect to the parameterization by Ruessink et al. (2012) occur for high Sk_{p2u} in deeper water (Figure 2.7c) and high $|As_{p2u}|$-values (Figure 2.7f,h). Besides that, a significant increase in variability was observed on top of the shoal (Figure 2.7g,h). All these differences are explored here by examining wave transformation effects associated with wave breaking, non-linear interactions and currents.

Table 2.2: Correlation coefficient R^2 between measured Sk_{p2u} and As_{p2u} and Ur.

Location	Sk_{p2u} R^2	As_{p2u} R^2
P1	0.89	0.03
P8	0.88	0.05
F4	0.87	0.10
P3	0.89	0.07
P5	0.91	0.29
F5	0.87	0.47
F1	0.83	0.36
P7	0.76	0.74
P4	0.28	0.01
P2	0.13	0.05

VARIABILITY CAUSED BY WAVE BREAKING

High $|As_{p2u}|$-values typically correspond to breaking waves. Therefore, the high values at P2 and P7 (Figure 2.7f,h) suggest that differences in breaking patterns could describe part of the variability. The relative wave height, H/d, is a common parameter to discriminate between breaking and non-breaking waves. To quantify whether waves are expected to break between P1 and P2, a new parameter, G, was defined, which is the predicted wave height at P2 divided by the water depth at P2. The predicted wave height at P2 was obtained by shoaling the wave height from P1 towards P2 assuming energy conservation and unidirectional wave propagation. In equation form, G, was computed as:

$$G = \frac{H_{P1}\sqrt{c_{g,P1}/c_{g,P2}}}{d_{P2}} \tag{2.7}$$

with group celerity c_{g_i} at location i computed according to linear wave theory as:

$$c_{g_i} = \left(\frac{1}{2} + \frac{k_i d_i}{sinh(2k_i d_i)}\right)\frac{\sigma_i}{k_i}. \tag{2.8}$$

If G is higher than 0.5, which is within the common range of breaking criteria for irregular waves over sloping bathymetry for $\gamma = H_{br}/d$ (Battjes & Stive, 1985), it is assumed that wave breaking took place. The added value of using G over the more traditional local estimate of H/d is that it not only indicates whether waves are expected to break or not, but also for how long waves have been breaking and thus what proportion of a random wave field is expected to break. Thus, G essentially describes how far in the surf zone the data have been collected.

Figure 2.8a,b shows how the wave shape parameters, Sk_{p2u} and As_{p2u}, vary as a function of G. For $G > 0.5$, the absolute values of Sk_{p2u} and As_{p2u} are also high. For low values of G, a wide range in Sk_{p2u} and near-zero As_{p2u} was observed. This difference is consistent with the fact that shoaling waves start developing Sk_{p2u} earlier than As_{p2u}. If we use a threshold of $G = 0.5$, we clearly see that the two distinct trends in As_{p2u} at P2 are explained by the fact whether waves have broken or not before reaching P2 (see red markers in Figure 2.7h). In addition, we see that most variability in Sk_{p2u} is associated with

low G values, i.e., non-breaking cases. Figure 2.8c finally shows that Ur, although commonly used to predict Sk_{p2u} and As_{p2u}, is not able to discriminate between breaking and non-breaking waves (see for instance the wide range of G for $Ur = 0.3$ in Figure 2.8c).

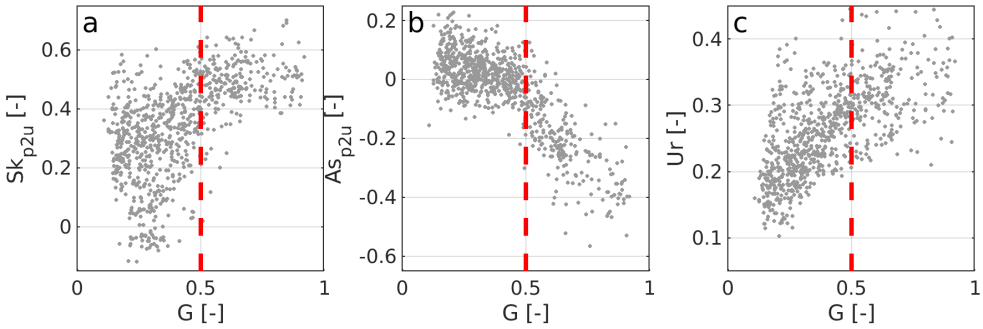

Figure 2.8: (**a**) Sk_{p2u}; (**b**) As_{p2u}; and (**c**) Ur at P2 as a function of parameter G, defined as the incoming wave height at P1 shoaled towards P2 divided by the water depth at P2. Red dashed line represents wave breaking threshold $G = 0.5$.

To further investigate the role of wave transformation on the observed variability in Sk_{p2u} and As_{p2u}, we examined the changes in wave characteristics over the bathymetric transect (Figure 2.2). More specifically, we examined the changes in Sk_{p2u}, As_{p2u} and Ur during wave propagation from P7 (d = 5.3 m) to P2 (d = 4.3 m), as P7 was the last sensor before scatter in Sk_{p2u} and As_{p2u} as a function of Ur significantly increased. Sk_{p2u} is remarkably constant between the two sensors regardless of the fact whether waves are breaking or not (Figure 2.9b) while $|As_{p2u}|$ stays near-zero for non-breaking cases and slightly increases for breaking cases (Figure 2.9c). The increase in $|As_{p2u}|$ for breaking cases is explained by the fact that depth has decreased, thus a larger proportion of the waves will be breaking waves at P2. This is consistent with the strong dependence of As_{p2u} on G described above. In contrast to the marginal changes in Sk_{p2u} and As_{p2u}, Ur significantly changes between P7 and P2, with a clear decrease for breaking waves and an increase for non-breaking waves (Figure 2.9a). The observed decrease in Ur is caused by increasing k, and decreasing a due to breaking. The observed increase in Ur for non-breaking cases, on the other hand, is a result of an increase in a and a decrease in d. This decrease of Ur for breaking waves (high Sk_{p2u}) in contrast to the increase for non-breaking waves (low Sk_{p2u}) explains the increased scatter at P2 compared to P7 (black vs. grey and red markers in Figure 2.9d, in which the red and grey arrows represent the general trend for breaking and non-breaking cases, respectively). In a similar manner, scatter in asymmetry is increased from P7 to P2 (see Figure 2.9e). It also explains why the most asymmetric waves were observed at lower Ur numbers at P2 than at P7 (compare Figure 2.7f,h). Thus, apparently, when wave-breaking occurs, the Ur-number is not the best parameter to predict the wave shape, since large scatter was observed. An approach to reduce the scatter in parameterizations predicting the wave shape is discussed in Section 2.4.2.

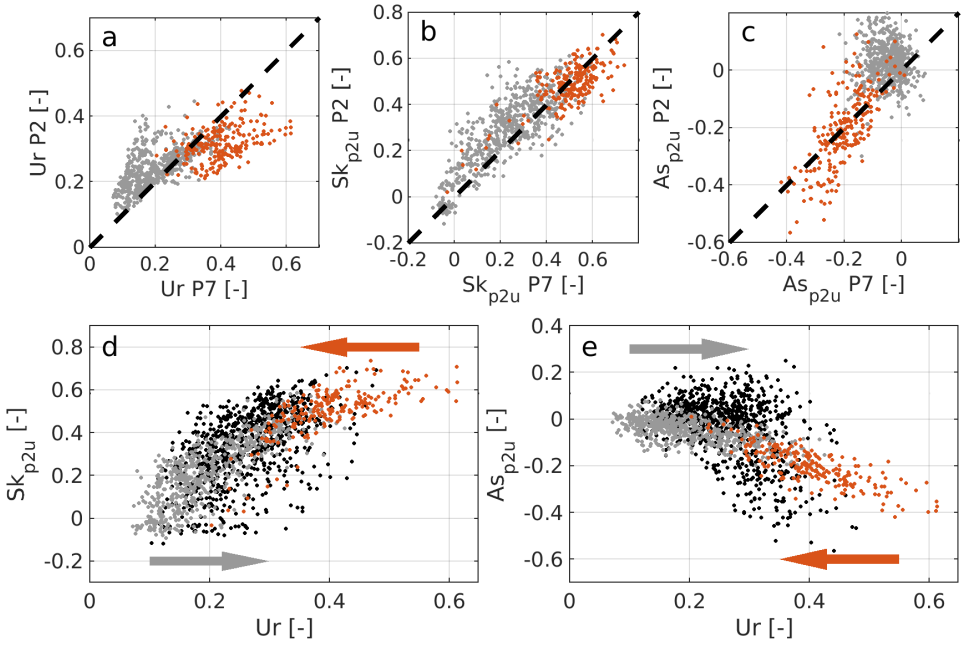

Figure 2.9: Development of: (**a**) Ur; (**b**) Sk_{p2u}; and (**c**) As_{p2u} for non-breaking (grey) and breaking (colored) cases, from P7 to P2. Ur, Sk_{p2u} and As_{p2u} at P2 are visualized as a function of Ur, Sk_{p2u} and As_{p2u} at P7, respectively. Colors for the breaking cases indicate U_n (m/s). The black dashed line has slope 1, thus indicates no change. The effect on (**d**) Sk_{p2u} and (**e**) As_{p2u} as a function of Ur is shown by visualizing data-points at P7 in grey (non-breaking) and red (breaking) and at P2 in black (all). The general evolution of data clouds from P7 to P2 for non-breaking and breaking conditions is visualized by grey and red arrows, respectively.

VARIABILITY CAUSED BY NONLINEAR ENERGY TRANSFER RATE

Nonlinear interactions lead to energy transfer from the primary harmonics to the higher harmonics and are thus essential for the development of Sk_{p2u} and As_{p2u}. From Hasselmann (1962), it is known that the wave length, and thus period, of the primary wave field is a key variable influencing the nonlinear energy transfer strength. As a result, longer waves are expected to develop Sk_{p2u} sooner and at a higher rate than shorter waves. This was confirmed by the modeling study of Rocha et al. (2017), who showed that waves with higher period have faster development of Sk_{p2u} and As_{p2u}.

In line with findings by Hasselmann (1962) and Rocha et al. (2017), in this dataset, the incoming wave period $T_{m-1,0}$ (at the deepest sensor P1) explains a significant part of the variability in Sk_{p2u} as a function of Ur at the shallow sensors. Figure 2.10a shows that, within each Ur-bin, Sk_{p2u} varies as a function of $T_{m-1,0}$ at P1. Although the wave period is included in Ur through k, a long low wave can have the same Ur as a shorter higher wave when in the same depth, whereas a higher amount of Sk_{p2u} and $|As_{p2u}|$ is expected for the longer wave based on the different nonlinear energy transfer rate.

Besides variability at the shallow sensors, the higher Sk_{p2u} in deeper water is also related to high incoming wave periods. The longer waves, which feel the bottom earlier, have already transformed into a more skewed wave shape than predicted by the parame-

terization by Ruessink et al. (2012) based on local Ur (Figure 2.10b).

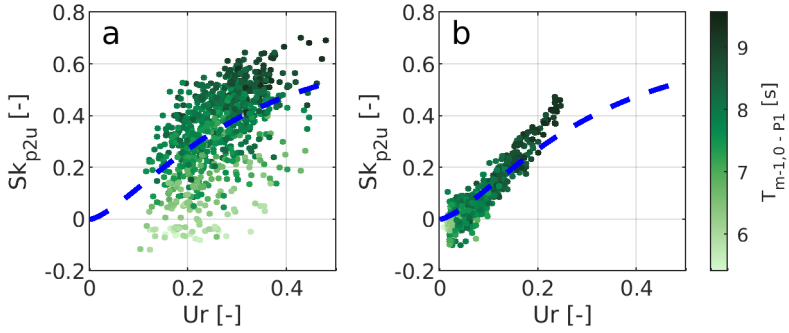

Figure 2.10: (**a**) Sk_{p2u} as a function of Ur at P2 in d = 4.3m and (**b**) at P1 in d = 10.4m. Light to dark green colors indicate the incoming spectral period $T_{m-1,0}$ at P1 in seconds. The blue dashed lines represent the Ruessink et al. (2012) parameterization.

VARIABILITY CAUSED BY CURRENTS

At P2, a large range of As_{p2u} and Ur is seen for the breaking waves (red dots in Figure 2.7h), which cannot be explained by a difference in incoming wave period because all those waves are long (9–10 s, not shown). It can be seen in Figure 2.11c that opposing and following currents lead to two distinct branches. This results in a different As_{p2u} observed for opposing and following waves for the same Ur. The two different branches can be explained by the fact that, in breaking conditions, Ur decreases more when the waves propagate from P7 to P2 for opposing currents than for following currents (compare blue and red colors in Figure 2.11a). This stronger decrease is due to the shortening of wave length if the current magnitude increases in shallow water during the opposing currents, and subsequently the change in k influences Ur.

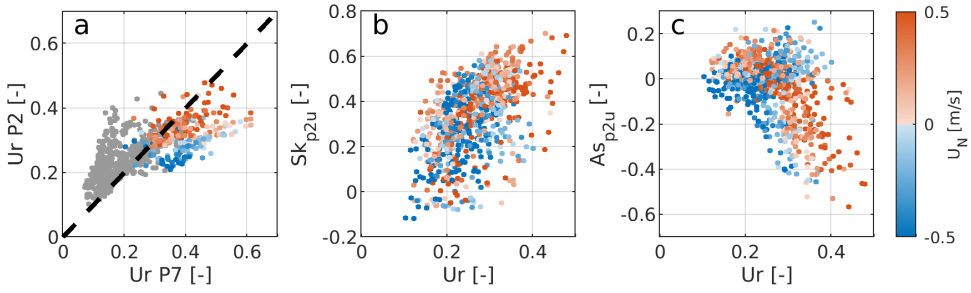

Figure 2.11: Influence of the currents on Ur, Sk_{p2u}, and As_{p2u} at P2. (**a**) Development of Ur from P7 towards P2, in which grey dots are non-breaking cases and colored dots are breaking cases. The black dashed line represents unity. (**b**) Sk_{p2u} as a function of Ur. (**c**) As_{p2u} as a function of Ur. Blue to red colors indicate the ambient current in direction of wave propagation U_n in m/s.

2.4. DISCUSSION

2.4.1. RELEVANCE IN MORPHODYNAMIC MODELING

Long-term simulations using process-based models do not model waves to such extent that the skewness and asymmetry are resolved. Therefore, parameterizations are needed to predict the skewness and asymmetry, usually as a function of local Ur.

A recent numerical study for this specific tidal inlet by Reniers et al. (2019) investigated the relevance of wave-shape induced transport compared to the traditional transport where sediment is stirred up by waves and transported by the currents. They found that the contribution of wave-shape transport is the dominating mode of transport in stormy conditions at the shallow locations, and can counteract the tide-induced sediment transport leading to a net onshore sediment transport.

This dataset has shown that it is in those conditions, when wave-shape transport is dominant, that most deviations from the parameterizations are observed (e.g., for breaking waves and at the shallow sensors). Since wave-shape transport is always onshore directed, small errors will accumulate over long-term simulations and can thus significantly influence the development of the shallow ebb-tidal shoal.

2.4.2. CORRECTING FOR DELAYED RESPONSE IN WAVE SHAPE

Changes in Sk_{p2u} and As_{p2u} when waves propagate from P7 to P2 are much less significant than changes in Ur (see Figure 2.9). This suggests a delayed response of the wave shape, and in particular of the skewness, to changes in the Ursell number when waves propagate towards shallower water depths. In the following, we want to check if using an Ursell number corresponding to an earlier stage of wave transformation, $Ur^\star$ (defined at depth $d^\star = d+\Delta d$, with $\Delta d > 0$) has better predictive skills than using the local Ursell value Ur (at depth d). Since P4 (at the landward slope) is in a different regime, where $\Delta d < 0$, it is excluded for this analysis. We assume that, at the deepest sensor, the skewness is close to being fully developed and thus has an optimal fit with the Ursell number (see also the high R^2 value in Table 2.2 for P1), which we take as a reference for the optimization procedure. More specifically, we iteratively estimate, for each sensor, the depth correction Δd needed to get the best fit with the observation at P1 in terms of both slope and intersect of the least square linear fit. The modified $Ur^\star$ is computed as:

$$Ur^\star = \frac{3}{4}\frac{A^\star}{k^{\star 2} d^{\star 3}}, \tag{2.9}$$

with $k^\star$ obtained by deshoaling k from depth d to $d^\star$ using linear wave theory, and amplitude $A^\star$, at depth $d^\star$ obtained by linear interpolation between the location under consideration and the location before it in deeper water.

Table 2.3 shows per location the Δd by which the Ursell number needs to be corrected in order to obtain the optimized $Ur^\star$. It is seen that the delay is negligible ($\Delta d < 0.25$ m) at the deeper sensors (P1, P8, F4, P3, and P5), but is significant at the shallower sensors on the steeper seaward slope (F5, P7, and P2). Figure 2.12 shows Sk_{p2u} and As_{p2u} as a function of local Ur and delayed $Ur^\star$. For Sk_{p2u}, it is seen that variability reduces when using $Ur^\star$ (compare Figure 2.12a,c), which is also reflected by a small decrease in standard deviation (averaged of the standard deviations of the five bins) from 0.09 to 0.08. Although $Ur^\star$ is optimized for Sk_{p2u}, As_{p2u} also seems to be better predicted by $Ur^\star$ since the individual

sensors for high $|As_{p2u}|$ follow similar trends. The averaged standard deviation for As_{p2u} does not decrease (0.07 for Ur and $Ur^{\star}$), which is probably because most points have close to zero As_{p2u}, thus will not be affected by the delayed parameterization. Visually, it can be seen, however, that it decreases the number of outliers.

Table 2.3: Depth by which Ur needs to be delayed to get $Ur^{\star}$ per sensor accompanied by the mean depth and bed slope the sensors are in.

Location	**P1**	**P8**	**F4**	**P3**	**P5**	**F5**	**P7**	**P2**
Δd (m)	0	0.25	0.2	0.2	0	1.1	0.8	0.85
d (m)	10.4	9.5	8.5	8.2	7.9	6.6	5.3	4.3
bed slope (-)	0.004	0.004	0.004	0.002	0.005	0.006	0.009	0.011

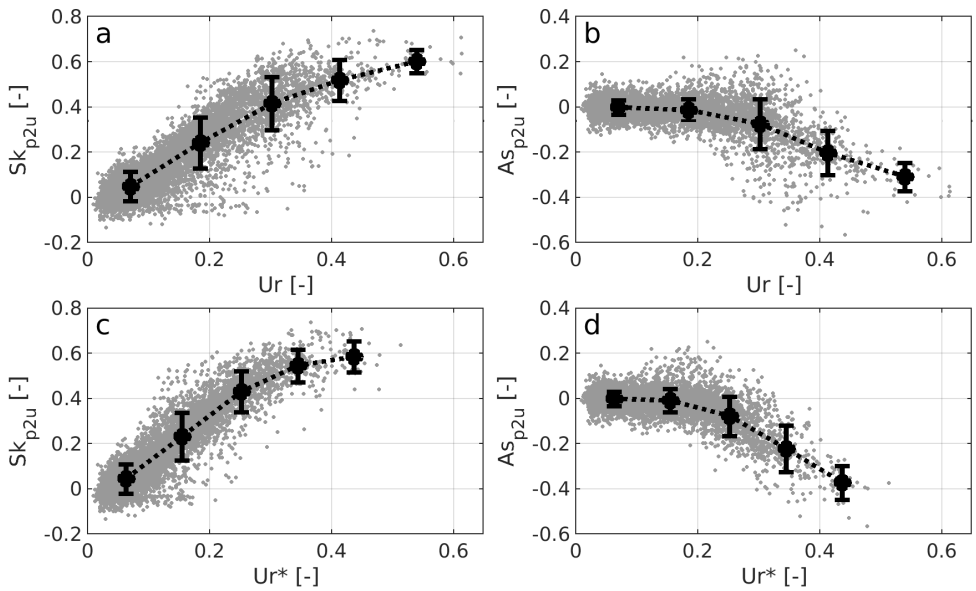

Figure 2.12: (**a**) Sk_{p2u} and (**b**) As_{p2u} of all sensors (excluding P4) as a function of local Ur. (**c**) Sk_{p2u} and (**d**) As_{p2u} of all sensors (excluding P4) as a function of delayed $Ur^{\star}$. Black error bars indicate mean per bin ± one standard deviation.

2.4.3. FUTURE WORK

This chapter characterizes conditions in which the wave shape deviates from commonly used parameterizations. It is proposed in a follow-up study to include offshore wave steepness as this determines the shoaling characteristics and the breakpoint of the waves (Rocha et al., 2017). In addition, the strength of the nonlinear interactions should be included since this proved to explain most of the variability at the shallow sensors for non-breaking waves. Once waves break, the parameterization can be improved by taking into account the proportion of waves which are breaking, because this was shown to be the

dominant parameter defining the amount of asymmetry in breaking conditions. Finally, it should be investigated whether the delayed response of the wave shape to changes in the Ursell number under rapidly changing conditions should be accounted for, and if so how it varies with bed slope, wave length and directional spreading.

The efficiency of the above-mentioned improvements cannot be properly quantified with our field data due to their limited spatial resolution. Although it is an exceptionally comprehensive dataset, wave characteristics were only measured at ten locations over a relatively large area, with only one measurement point in the breaking zone and one in the de-shoaling zone. Future work will include the use of detailed wave-resolving simulations, from which skewness and asymmetry can be estimated with a high spatial resolution. This will allow us to study the development of wave shape at many more locations and under controllable conditions in which only a single input parameter is varied. This will allow us to further improve our understanding of the physical processes relevant to predict wave shape evolution and improve future parameterizations.

As mentioned above, parameterizations for skewness and asymmetry are usually used to parameterize wave-induced sediment transport in process based models. In such a modeling approach, wave predictions are usually based on a phase-averaged spectral wave model. It is interesting to note that such models provide much more information than the wave parameters currently used to calculate Ur and hence to parameterize skewness and asymmetry. They for instance also provide data on directional spreading, frequency spreading and the proportion of breaking waves and associated dissipation patterns, which could also be included in an improved parameterization.

2.5. CONCLUSIONS

This chapter presents a new dataset of waves and currents obtained at 10 locations on the ebb-tidal shoal seaward of the Ameland Inlet. Pressure signals were transformed in near-bed orbital velocity signals in order to investigate the occurrence of the near bed velocity skewness and asymmetry, as these are the main drivers of wave-induced sediment transport. Significant $\widetilde{Sk}_{p2u}$ and $\widetilde{As}_{p2u}$ were observed during the stormy periods with $H >$ 2 m, and it was seen that $\widetilde{Sk}_{p2u}$ and $|\widetilde{As}_{p2u}|$ increased moving to shallower water.

Wave shape parameterizations are usually a function of local Ur. For this dataset it was found that variability in wave shape was well-explained by variability in local Ur in deeper water. However, for shallower locations, variability in Ur could only partially explain the variability in Sk_{p2u} and As_{p2u}, indicating that some physical processes are not properly accounted for. The increased scatter at the shallow locations could be attributed to a combination of three main physical processes: wave-breaking, spatial variability in tidal currents, and the nonlinear energy transfer rate.

Towards the shallow sensors, a rapid decrease in Ur for breaking conditions and an increase for non-breaking conditions is observed, although Sk_{p2u} and As_{p2u} only marginally change. This leads to significant scatter in Sk_{p2u} and As_{p2u} as a function of Ur at these shallow locations (see Figure 2.9). For opposing currents, this decrease in Ur for breaking conditions is even bigger than for following currents, because the wave length decreases and increases, respectively. Another influence contributing to the scatter of Sk_{p2u} as a function of Ur is the nonlinear energy transfer rate, which is not properly accounted for

in Ur.

It is shown that a potential improvement for future parameterizations would be to correct for the fact that the wave shape does not instantly respond to changes in depth and currents. For this dataset, this led to a reduced variance from 0.09 to 0.08 for Sk_{p2u}. It is expected that the added value will be higher if relatively more cases with high nonlinearity are included in the dataset.

APPENDICES

2.A. DRIFTER STUDY

To provide insight in the spatial variability of the (surface) currents around the measurement frames and pressure sensors, 30 GPS-equipped floating surface drifters were developed. These drifters were constructed from water-tight containers filled with concrete to decrease the buoyancy in order to reduce the effect of the wind. A flag is added for visibility, a bottom plate to limit the vertical motion and a cell phone as GPS tracking device (see Fig 2.13).

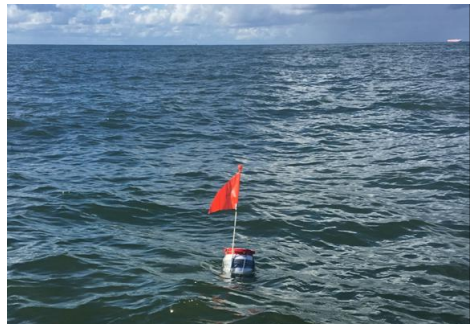

Figure 2.13: GPS-equipped surface current drifter deployed in the Ameland Inlet.

Figure 2.14 shows the bathymetry of the ebb tidal shoal with the black box indicating the area where the drifter deployments were performed. The drifter deployments discussed here were performed on the 9th of September 2017 between flood tide and ebb tide (see bottom panel of Fig. 2.15 for the associated water levels). Wind and wave conditions were very mild during this day, so the drifter displacements are predominantly tide-driven. A total of 15 successive drifter deployments were performed (see numbers in Fig. 2.15). Per deployment, 20 drifters were released upstream of the measurement area and retrieved when all of them had passed the instrumented area. For each of the 15 deployments, the GPS locations of the drifters were de-spiked and frequency-filtered to retain the current-related displacement. Subsequently, the velocity along the individual drifter tracks was obtained by differentiating the displacement in time. Interpolating these tracks to a regular grid provided a current map for each deployment (see Fig. 2.15).

It can be seen that during flood tide (Fig. 2.15 panels 1-5), velocities are rather uniformly distributed with a slight increase in magnitude in the shallower area (southeast). In contrast, during ebb tide (Fig. 2.15 panels 12-15), stronger currents are more concentrated in the ebb channel resulting in stronger spatial velocity gradients. During slack tide (Fig. 2.15 panels 8-11), a counterclockwise rotation of the currents is observed.

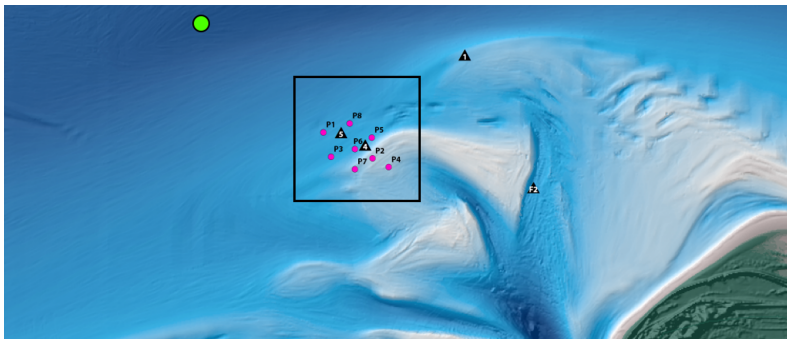

Figure 2.14: Bathymetry of the Ameland ebb-tidal delta with the black box indicating the area in which drifter measurements were performed.

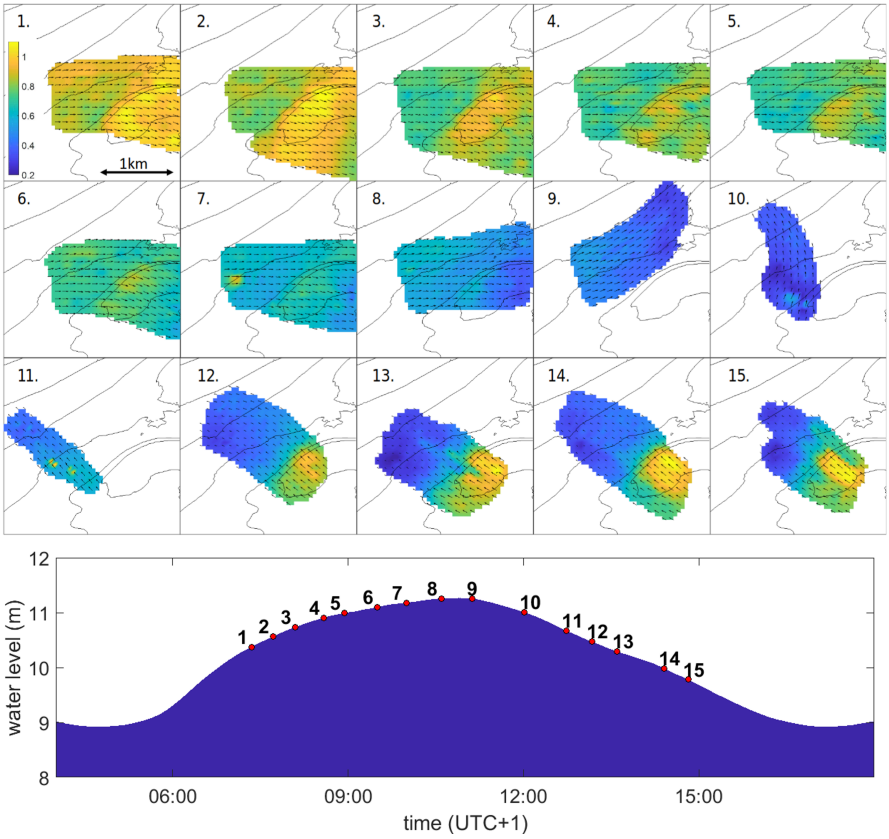

Figure 2.15: Velocity maps (in m/s) from the 15 subsequent drifter deployments on the 9th of September 2017 for different tidal phases at the ebb-tidal shoal. Panel numbers are associated with the water levels shown in the bottom panel.

2.B. VALIDITY DELFT3D MODEL

The Delft3D model of the Ameland Inlet and surroundings, as described by Nederhoff et al. (2019), is used to estimate velocities where they were not measured (at the standalone pressure sensors). Figure 2.16 shows the modeled water levels and depth-averaged velocities as a function of the measured water levels and depth-averaged velocities at Frames 1, 4, and 5. Table 2.4 shows that the order of magnitude of water levels and velocities is well-predicted by the model, with RMSE not exceeding 0.25 m and 0.13 m/s for water levels and depth-averaged velocities, respectively.

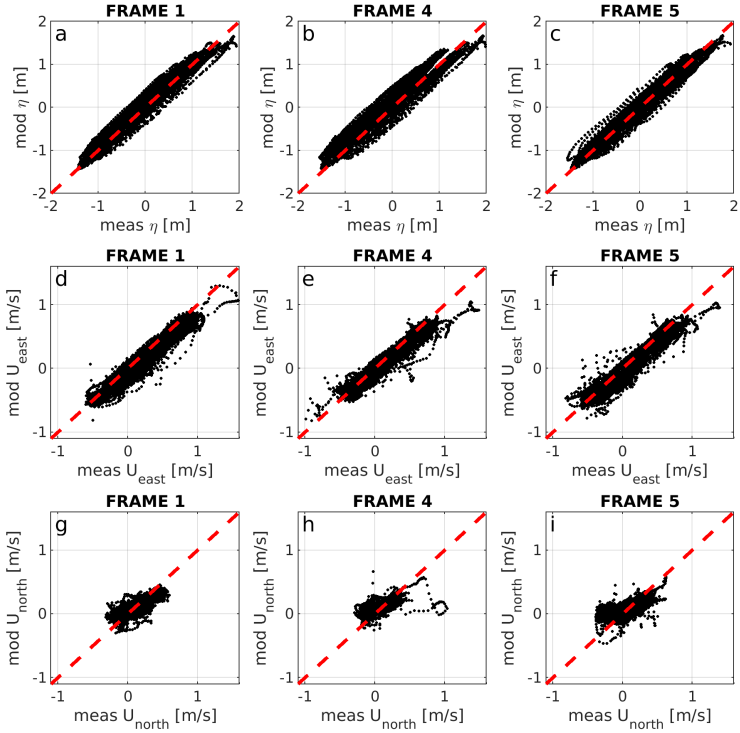

Figure 2.16: Comparison between measured and modeled η, U_{east}, and U_{north} at Frames 1, 4, and 5 where black dots are individual data points and red dashed lines are unity.

Table 2.4: RMSE between half-hourly-averaged modeled and measured water levels and depth-averaged velocities at Frames 1, 4, and 5.

	F1	**F4**	**F5**
η (m)	0.17	0.25	0.16
U_{east} (m/s)	0.13	0.12	0.13
U_{north} (m/s)	0.10	0.12	0.13

3

THE RELATIONSHIP BETWEEN SEA-SWELL BOUND WAVE HEIGHT AND WAVE SHAPE

ABSTRACT

The nonlinear wave shape, expressed by skewness and asymmetry, can be calculated from surface elevation or pressure time series using bispectral analysis. Here, it is shown that the same analysis technique can be used to calculate the bound superharmonic wave height. Using measured near-bed pressures from three different field experiments, it is demonstrated that there is a clear relationship between this bound wave height and the nonlinear wave shape, independent of the measurement time and location. This implies that knowledge on the spatially varying bound wave height can be used to improve wave shape-induced sediment transport predictions. Given the frequency-directional sea-swell wave spectrum, the bound wave height can be predicted using second order wave theory. This chapter shows that in relatively deep water, where conditions are not too nonlinear, this theory can accurately predict the bispectrally estimated bound superharmonic wave height. However, in relatively shallow water, the mismatch between observed and predicted bound wave height increases significantly due to wave breaking, strong currents, and increased wave nonlinearity. These processes are often included in phase-averaged wind-wave models that predict the evolution of the frequency-directional spectrum over variable bathymetry through source terms in a wave action balance, including the transfer of energy to bound super harmonics. The possibility to calculate and compare with the observed bound super harmonic wave height opens the door to improved model predictions of the bound wave height, nonlinear wave shape and associated sediment transport in large-scale morphodynamic models at low additional computational cost.

This chapter is an adapted version from the publication: de Wit, F.P., Tissier, M.F.S. and Reniers, A.J.H.M., (2020), Characterizing Wave Shape Evolution on an Ebb-Tidal Shoal, *Journal of Marine Science and Engineering 8*(9), 643.

3.1. INTRODUCTION

Coastal management decisions, such as nourishment strategies and sea level rise scenarios, rely more and more on morphodynamic model simulations. Within these simulations, fluxes in sediment transport, caused by hydrodynamic forcing mechanisms, result in changes in the bathymetry. An important contribution to the sediment transport fluxes is the wave shape-induced sediment transport driven by the skewness and asymmetry of the individual waves (Hoefel & Elgar, 2003; Hsu et al., 2006; Ruessink et al., 2011; Silva et al., 2011). Although its instantaneous magnitude is often smaller than other contributions, it can have a considerable net effect on the bathymetric evolution as the contribution is typically in the dominant wave direction (Kranenburg et al., 2013; Walstra et al., 2012). As such, it is important for beach recovery after storm impact (Elgar et al., 2001; Masselink et al., 2007), onshore bar motion (Thornton et al., 1996; Elgar et al., 2001; Aagaard et al., 2006; Ruessink et al., 2007) and the evolution of ebb-tidal shoals (e.g., Chen et al., 2015; Reniers et al., 2019).

Current large-scale morphodynamic modeling approaches generally combine a spectral wave transformation model (Booij et al., 1999; Ris et al., 1999; Benoit et al., 1997; Tolman, 1991; Janssen et al., 2006) and a flow model (e.g., Lesser et al., 2004; Walstra et al., 2001; Elias et al., 2001; Luettich et al., 1992; Westerink et al., 1994) to predict the local wave, flow and sediment transport conditions (e.g., Roelvink et al., 2003; Lesser et al., 2004). Using a local parameterization based on the wave height, wave period and water depth, the wave skewness, asymmetry, and associated sediment transport are obtained (e.g., Isobe & Horikawa, 1982; Doering & Bowen, 1995; Abreu et al., 2010; Ruessink et al., 2012; Boechat Albernaz et al., 2019). However, as was shown by Rocha et al. (2013), Rocha et al. (2017), and De Wit et al. (2019), predicting the wave shape using a local approach has its limitations, related to the fact that the prior evolution of wave shape is not taken into account. As a result, the wave shape can be different although the local wave height, period, and water depth are exactly equal, if, for instance, the bed slope is different (Norheim et al., 1998; Eldrup & Andersen, 2020), the conditions are rapidly changing (De Wit et al., 2019), or the offshore wave steepness is different (Rocha et al., 2017). Thus, there is a need for a better way to predict the wave shape that includes the history of the waves before reaching a certain location.

The wave skewness and asymmetry can be computed with a bispectral analysis corresponding to the sum of the real and imaginary parts of the bispectrum, respectively (e.g., Hasselmann et al., 1963; Elgar & Guza, 1985). The bispectrum is a reflection of the coupling between the primary waves and the bound super and sub harmonics (Elgar & Guza, 1985; Eldeberky & Madsen, 1999). This implies that there is a close connection between the nonlinear wave shape and the proportion of bound wave energy.

The bound portion of energy in the super harmonics within a directionally spread sea-swell wave field can be predicted with the second order theory of Hasselmann (1962) based on a local equilibrium over a horizontal bed. However, in the presence of a variable bathymetry and thus spatially evolving sea-swell wave field this may lead to an erroneous estimate as demonstrated by Herbers & Burton (1997). On the other hand, spectral wind-wave models often include a source term to describe the transfer of wave energy from the primary wind-waves to bound super harmonics through triad sum interactions over variable bathymetry (Eldeberky & Madsen, 1999; Salmon et al., 2016; Becq-Girard et al., 1999).

The modeled bound fraction of superharmonic wave energy is an integration of the source term in the down-wave direction showing up as an additional spectral peak at twice the primary frequencies (e.g., Madsen & Eldeberky, 1999; Eldeberky & Madsen, 1999). However, to speed up the computations to enable morphodynamic computations at realistic time scales, the phase information is ignored and even though the spatially evolving fraction of bound energy is implicitly predicted, the accompanying skewness and asymmetry are not known.

Examining the three-dimensional (3D) wavenumber-frequency spectrum is a relatively straightforward way to discriminate between the bound and free wave energy as these follow different dispersion relations (e.g., Phillips, 1960). However, estimating the full 3D wave spectrum requires high-resolution spatial information that is rarely available in the field (see e.g., Leckler et al. (2015) for one of the exceptions). Alternatively, bispectra can be used to characterize the portion of bound energy in a given frequency range. Most efforts to quantify and analyze bound harmonic energy have focussed on the sub-harmonic range (e.g., Henderson et al., 2006; Ruessink, 1998; Sheremet et al., 2002; Van Dongeren et al., 2003; Roelvink et al., 2009; Guedes et al., 2013; De Bakker et al., 2015) following the work of Herbers et al. (1994) who demonstrated that the bound fraction of subharmonic (i.e., infragravity) energy could be obtained from the difference interactions in the bispectrum. Significantly less attention has been devoted to quantifying the bound energy in the super harmonic range, with the most notable contributions being the work by Herbers & Guza (1992, 1994) and Herbers et al. (1992) who examined bound wave energy in intermediate water depths.

The aforementioned studies (Herbers & Guza, 1992, 1994; Herbers et al., 1992) showed that triad sum interactions between wave components with large difference angle of propagation can contribute significantly to the bound near-bed pressure variance at these depths. Interestingly, these are typically associated to negative interaction coefficients according to the theory of Hasselmann (1962), while the more classical sum interactions between wave components with small difference in angle of propagation have a positive contribution. Thus, for a given sum frequency in the superharmonic range, both positive and negative contributions from primary wave pairs can occur such as the bispectrum is expected to yield a lower limit of the bound super harmonic energy. Several authors (Elgar & Guza, 1985; Young & Eldeberky, 1998; Sénéchal et al., 2002) additionally mention, based on the work of McComas & Briscoe (1980), that estimating the bound super harmonics from the bispectrum in a broad-banded spectrum is not straightforward. This inhibits a direct comparison with the predictions of the wind-wave spectral models. Notably, Herbers et al. (1992) did find a good match between predictions by the theory of Hasselmann (1962) and observations in a case of narrow-banded energetic swell conditions (their Figure 10d) in contrast to conditions with crossing sea states (their Figure 10a–c). This raises the question to what extent the bispectral estimate of the bound super harmonic fraction can work for sea-swell conditions.

In the following, we therefore construct a method to first estimate the bound portion of the energy in the super harmonics in a realistic directionally spread wave field and secondly to use this as a predictor of the nonlinear wave shape controlling wave skewness and asymmetry. To that end, the velocity and pressure data obtained at nine locations on the Ameland ebb-tidal delta from the CoastalGenesis2/SEAWAD field campaign in Septem-

ber 2017 are examined using bispectral analysis. The bound superharmonic fraction is expressed as an equivalent observed bound wave height that is compared with the predicted bound wave height obtained from the equilibrium theory of Hasselmann (1962) to explore its spatial evolution. Next, the correspondence between the bound wave height and nonlinear wave shape is examined to explore the potential of using a wave shape parameterization based on the predicted bound wave height instead of a local parameterization. This is followed up with a discussion on the general applicability of such an approach and the necessary steps in spectral wave modeling to enable these predictions.

3.2. BACKGROUND

3.2.1. THE SPECTRUM

The surface elevation is represented as a summation of discrete frequencies as

$$\eta(t) = \sum_{m=-N}^{N} \frac{1}{2} C_m e^{-2\pi i f_m t} + \frac{1}{2} C_m^* e^{2\pi i f_m t} \tag{3.1}$$

in which C_m is the complex amplitude at discrete frequency $f_m = m\Delta f$ with Δf being the frequency resolution, C_m^* indicates the complex conjugate of C_m, i is the imaginary number, and t is time. The number of discrete spectral estimates is $2N+1$, which are bound by the Nyquist frequencies: $\pm f_N = \pm f_s/2$, in which f_s is the discrete sampling frequency of the surface elevation time series. The complex amplitudes are obtained by applying a discrete fast Fourier transformation on the surface elevation. Subsequently, the (double-sided) variance spectrum is defined as

$$E'_m = \mathbf{E}[C_m C_m^*] \qquad \text{for: } -N \le m \le N \tag{3.2}$$

in which $\mathbf{E}[...]$ denotes the expected value. For convenience, readability and computational efficiency the variance spectrum is instead presented as a single sided discrete variance spectrum:

$$E_m = 2E'_m \qquad \text{for: } 0 \le m \le N \tag{3.3}$$

The corresponding variance density spectrum is:

$$E(f_m) = \frac{E_m}{\Delta f} \qquad \text{for: } 0 \le m \le N \tag{3.4}$$

from this the sea-swell variance can be calculated as:

$$m_0 = \sum_{m=i_{min}}^{i_{max}} E(f_m)\Delta f \tag{3.5}$$

in which i_{min} and i_{max} are indices corresponding to the sea-swell frequency range. These are defined in this study as $f_{i_{min}} = f_{peak}/2$ in order to separate the sea-swell waves from the infragravity waves (Roelvink et al., 2009) and $f_{i_{max}} = f_N$. The sea-swell significant wave height is obtained from the variance with:

$$H = 4\sqrt{m_0} \tag{3.6}$$

If besides pressure, also collocated x- and y-velocities are present, the 2D frequency-directional variance spectrum can be computed:

$$E(f_m,\theta_r) = E(f_m)\Theta(f_m,\theta_r) \tag{3.7}$$

in which $\Theta(f_m,\theta_r)$ is the directional distribution at discrete frequency f_m and discrete direction θ_r.

3.2.2. THE BISPECTRUM

The bispectrum is a spectral representation of third-order statistics that can be used to analyze the nonlinear interactions between a triad of frequencies f_m, f_n and f_p that satisfies $f_m + f_n = f_p$. The discrete bispectrum is defined as

$$B_{m,n} = \mathbf{E}[C_m C_n C_p^*] \qquad \text{for: } p = m+n \text{ and } -N \le m,n,p \le N \tag{3.8}$$

Subsequently, the bispectral density is defined as:

$$B(f_m,f_n) = \frac{B_{m,n}}{(\Delta f)^2} \tag{3.9}$$

If the three components are statistically independent, there is no phase correlation and $B(f_m,f_n) = 0$. In that case, the third component f_p is not bound to f_m and f_n but freely propagating. On the other hand, a non-zero bispectrum $B(f_m,f_n)$ indicates that (part of) the variance at f_p is bound to the energies at f_m and f_n.

In contrast to the variance density spectrum, the bispectrum is complex. The normalized magnitude and phase of the bispectrum are the bicoherence b^2 and the biphase β, given by

$$b^2(f_m,f_n) = 8\frac{|B(f_m,f_n)|^2}{E(f_m)E(f_n)E(f_p)} \tag{3.10}$$

$$\beta(f_m,f_n) = tan^{-1}\left(\frac{\Im(B(f_m,f_n))}{\Re(B(f_m,f_n))}\right) \tag{3.11}$$

in which $\Re$ and $\Im$ denote the real and imaginary parts, respectively. The factor 8 in Equation (3.10) arises because the double-sided bispectral density is normalized by single-sided variance densities. According to Kim & Powers (1979), the bicoherence characterizes the relative degree of coupling between three waves at f_m, f_n, and f_p, which can be used to determine the bound variance at f_p. Different equations to calculate the bicoherence have been presented in literature, all slightly differing in the way the bispectrum is normalized. Here, the equation of Haubrich (1965) is presented, as was later also applied by Herbers et al. (1994). Furthermore, Elgar & Guza (1988) showed that the statistical reliability of the bicoherence is insensitive to the normalization method. The intensity of the imaginary part of the bispectrum is indicative for the strength of the nonlinear energy transfers, which result in temporal or spatial changes in the spectrum (e.g., Agnon et al., 1993; Herbers & Burton, 1997). The real and imaginary parts of the bispectrum are also closely related to the wave shape, as will be described in Section 3.2.3.

Every triad interaction appears in the bispectrum multiple times. Due to symmetry in the bispectrum, it is redundant to calculate and analyze the full bispectrum, but all

sum and difference interactions are present in the triangle in (f_m, f_n)-space bounded by $(f_m = 0, f_n = 0)$, $(f_m = f_{N/2}, f_n = f_{N/2})$, and $(f_m = f_N, f_n = 0)$. For a detailed description of the symmetry regions in the bispectrum the reader is referred to Kim & Powers (1979).

3.2.3. WAVE SHAPE

The nonlinear shape of a wave can be described by its skewness (asymmetry w.r.t. the vertical axis) and asymmetry (asymmetry w.r.t. the horizontal axis). Skewness Sk_η and asymmetry As_η are third-order statistics (Elgar & Guza, 1985), which are proportional to the real and imaginary parts of the bispectrum, normalized by the variance. The sea-swell Sk_η and As_η are computed as

$$Sk_\eta = \frac{6\sum_{m=i_{min}}^{i_{max}} \sum_{n=i_{min}}^{i_{max}} \Re(B(f_m, f_n))(\Delta f)^2}{m_0^{3/2}} \tag{3.12}$$

$$As_\eta = \frac{6\sum_{m=i_{min}}^{i_{max}} \sum_{n=i_{min}}^{i_{max}} \Im(B(f_m, f_n))(\Delta f)^2}{m_0^{3/2}} \tag{3.13}$$

The factors 6 arise from the fact that the triangle that includes all positive frequencies of the bispectrum triangle covers 1/6 of the bispectral area. Sk_η and As_η can be combined in the nonlinear wave shape parameter S_η (Ruessink et al., 2012):

$$S_\eta = \sqrt{Sk_\eta^2 + As_\eta^2} \tag{3.14}$$

3.3. BOUND VARIANCE

This section outlines the method to obtain both the predicted as well as the observed bound wave variances, and the equivalent bound wave heights, from measurements.

3.3.1. PREDICTED BOUND VARIANCE FOR EQUILIBRIUM CONDITIONS

Using second-order finite depth theory, the variance associated with the bound super harmonics can be predicted (Hasselmann, 1962). Based on this theory, the bound variance at a given frequency f_p resulting from all sum interactions between primary sea-swell components which contribute to the variance at f_p is calculated as

$$E_{b,pred}(f_p) = \frac{1}{2} \sum_{r=1}^{N_\theta} \sum_{s=1}^{N_\theta} \sum_{m=i_{min}}^{p-i_{min}} E(f_{p-m}, \theta_r) E(f_m, \theta_s) D^2(f_{p-m}, f_m, \theta_r, \theta_s, d) \Delta f (\Delta\theta)^2 \tag{3.15}$$

in which r and s are discrete indices defining the directional bins such that $\theta_r = r\Delta\theta$ and $\theta_s = s\Delta\theta$. N_θ is the discrete number of directional bins resulting in the directional resolution $\Delta\theta = 2\pi/N_\theta$. D is the nonlinear coupling coefficient for seafloor pressure given by Herbers et al. (1994) and d is the mean water depth. The corresponding bound super harmonic wave height is computed as

$$H_{b,pred} = 4\sqrt{\sum_{p=i_{b,min}}^{i_{b,max}} E_{b,pred}(f_p)\Delta f} \tag{3.16}$$

in which $i_{b,min}$ and $i_{b,max}$ are indices corresponding to the bound superharmonic frequency range. These are defined in this study as $f_{i_{b,min}} = f_{peak}$ and $f_{i_{b,max}} = f_N$.

3.3.2. OBSERVED BOUND VARIANCE FROM THE BISPECTRUM

As was mentioned in Section 3.2.2, Kim & Powers (1979) [1] pointed out that the proportion of bound variance is related to the bicoherence. Integrating the bicoherence over all triad sum interactions contributing to frequency f_p gives the proportion of variance at f_p which is bound:

$$\begin{aligned}\frac{E_{b,obs,KP79}(f_p)}{E(f_p)} &= \sum_{m=i_{min}}^{p-i_{min}} b^2(f_m, f_{p-m})\Delta f \\ &= 8\sum_{m=i_{min}}^{p-i_{min}} \frac{|B(f_m, f_{p-m})|^2}{E(f_m)E(f_{p-m})E(f_p)}\Delta f \end{aligned} \tag{3.17}$$

The observed bound variance in the super harmonics can be written as

$$\sum_{p=i_{b,min}}^{i_{b,max}} E_{b,obs,KP79}(f_p)\Delta f = 8\sum_{p=i_{b,min}}^{i_{b,max}}\sum_{m=i_{min}}^{p-i_{min}} \frac{|B(f_m, f_{p-m})|^2}{E(f_m)E(f_{p-m})E(f_p)}(\Delta f)^2 \tag{3.18}$$

The observed bound wave height is subsequently computed as

$$H_{b,obs,KP79} = 4\sqrt{\sum_{p=i_{b,min}}^{i_{b,max}} E_{b,obs,KP79}(f_p)\Delta f} \tag{3.19}$$

Herbers et al. (1994) [2] proposed an expression for the observed bound proportion of variance in the infragravity wave range due to difference interactions between primary sea-swell waves using the bispectrum. In a similar way, we define the observed bound proportion of variance at frequency f_p associated with the sum interactions (i.e., bound super harmonics) as

$$\begin{aligned}\frac{\sum_{p=i_{b,min}}^{i_{b,max}} E_{b,obs,HEG94}(f_p)\Delta f}{\sum_{p=i_{b,min}}^{i_{b,max}} E(f_p)\Delta f} = \\ \alpha(f_p)\left|\frac{\frac{1}{2}\sum_{p=i_{b,min}}^{i_{b,max}}\sum_{m=i_{min}}^{p-i_{min}} B(f_m, f_{p-m})(\Delta f)^2}{\sqrt{\frac{1}{8}\sum_{p=i_{b,min}}^{i_{b,max}}\sum_{m=i_{min}}^{p-i_{min}} E(f_m)E(f_{p-m})(\Delta f)^2\sum_{p=i_{b,min}}^{i_{b,max}} E(f_p)\Delta f}}\right|^2\end{aligned} \tag{3.20}$$

in which $\alpha(f_p)$ is a weighting factor to account for differences in interaction strength between all triads contributing to frequency f_p. As discussed by Herbers et al. (1994), however, this effect is small for sea-swell waves and α can be assumed to be 1. Subsequently,

[1] KP79 refers to the methods and equations from Kim & Powers (1979).
[2] HEG94 refers to the methods and equations from Herbers et al. (1994).

the bound wave variance is expressed as

$$\sum_{p=i_{b,min}}^{i_{b,max}} E_{b,obs,HEG94}(f_p)\Delta f = 4\frac{\left|\sum_{p=i_{b,min}}^{i_{b,max}}\sum_{m=i_{min}}^{p-i_{min}} B(f_m,f_{p-m})(\Delta f)^2\right|^2}{\sum_{p=i_{b,min}}^{i_{b,max}}\sum_{m=i_{min}}^{p-i_{min}} E(f_m)E(f_{p-m})(\Delta f)^2} \tag{3.21}$$

Finally, the resulting bound wave height is computed as

$$H_{b,obs,HEG94} = 4\sqrt{\sum_{p=i_{b,min}}^{i_{b,max}} E_{b,obs,HEG94}(f_p)\Delta f} \tag{3.22}$$

Comparing Equations (3.18) and (3.21) illustrates the differences between the methods to compute the bound wave variance. While Kim & Powers (1979) first calculate all individual bicoherences before summing them, Herbers et al. (1994) first sum over the bispectrum and the cross products of the spectrum, subsequently square the absolute value of the summed bispectrum, and finally calculate the ratio. In Appendix 3.A, the performance of both methods is investigated as a function of the statistical reliability of the expected values of the spectrum and bispectrum (Equations (3.4) and (3.9)). From this, it is decided to use the HEG94 formulation to compute the observed bound wave height, because it provides the most reliable estimate for a low number of degrees of freedom. This is of key importance in order to be applicable to field data in which the time series duration is usually limited in order to satisfy stationary conditions. Essentially, by first summing the bispectrum and spectral cross terms individually, additional averaging is applied which results in a statistically more reliable spectrum for the same duration. It should be noted that this additional way of averaging is only valid if the part of the bispectrum over which is summed is dominated by positive sum interactions, because otherwise the contributions of the sum and difference interactions cancel each other out. Thus, in the following $H_{b,obs}$ refers to the observed bound wave height calculated following the HEG94 method (Equations (3.21) and (3.22)).

3.4. DATA

3.4.1. COASTALGENESIS2/SEAWAD FIELD CAMPAIGN

The 6-week CoastalGenesis2/SEAWAD field campaign was conducted in September and October 2017 by a consortium of universities and research institutes in order to improve the understanding of physical processes at the Ameland inlet (van der Werf et al., 2019; van Prooijen et al., 2020). The Ameland Inlet is a tidal inlet between the barrier islands Terschelling and Ameland at the north of the Netherlands. The barrier islands are located between the North Sea and the Wadden Sea. Seaward of the Ameland inlet, an ebb-tidal shoal has formed due to the deceleration of the ebb-tidal flow. During storm conditions with waves incoming from the north, it is on this shoal that the waves start feeling the bottom, reshape, and eventually break.

This chapter focuses on pressure and velocity measurements obtained at nine locations clustered together on the seaward side of the ebb-tidal shoal (see also Chapter 2). At two measurement frames (F4 and F5, see red dots in Figure 3.1), collocated pressure and near-bed velocity measurements were obtained. This was done using high-resolution,

downward looking, Acoustical Doppler Velocity Profilers (ADCP) that measured the velocity profile over the bottom 50 cm of the water column and concurrent pressure with a sampling frequency of 4 Hz. At seven other locations surrounding the two frames, standalone pressure sensors (P1–P8, black dots in Figure 3.1) were deployed measuring the pressure continuously with a sampling frequency of 10 Hz. The two frames and three pressure sensors were aligned along a main transect, while the four other pressure sensors were deployed on side transects to investigate two-dimensional spatial variability. The mean water depth and the sensor height above the bed is given for all locations in Table 3.1.

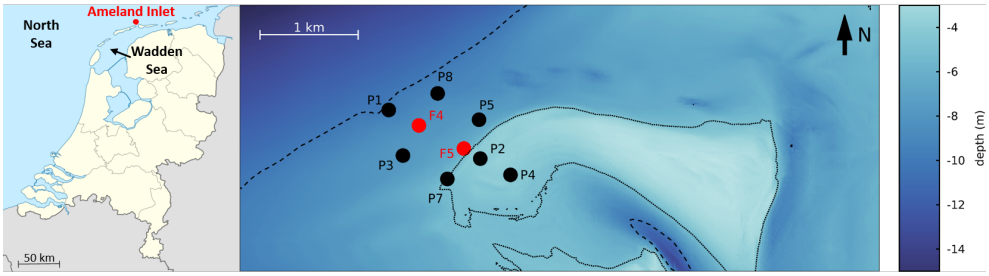

Figure 3.1: Left panel: Overview map of the Netherlands with the measurement location of the ebb-tidal shoal indicated by a red dot (source: Wikipedia Commons). Right panel: Bathymetric map of Ameland ebb-tidal shoal showing the location of the instrument frames (red circles) and pressure sensors (black circles). The dotted and dashed lines represent the −5 m and −10 m contour lines, respectively.

Table 3.1: Overview of measurement locations, the mean depth and sensor height above the bed as deployed in the field, and the quantities which were measured (p stands for pressure, and u and v are the horizontal components of the velocity field).

Location	Depth (m)	Sensor Height (m)	Measurement
P1	10.4	0.5	p
P8	9.5	0.5	p
F4	8.5	0.5	p, u, v
P3	8.2	0.5	p
P5	7.9	0.5	p
F5	6.6	0.5	p, u, v
P7	5.3	0.5	p
P2	4.3	0.5	p
P4	4.6	0.5	p

3.4.2. DATA PROCESSING

Measured pressure is expressed in meters of water column by dividing by ρg, in which ρ is the density of sea water (=1025 kg/m^3) and g the gravitational acceleration (=9.81 m/s^2). For two reasons it is chosen not to reconstruct the surface elevation accounting for wave-induced pressure attenuation with depth. First, wave shape-induced sediment transport is driven by the near-bed wave shape. Second, reconstructing the surface elevation from the near-bed pressure requires the use of a transfer function that generally relies on linear

wave theory. This introduces uncertainty, particularly in the high frequency range, where the bound higher harmonics are found. As a result, wave heights referred to in this chapter are actually near-bed pressure-head derived wave heights (denoted with superscript nb), meaning that the actual wave height as would be observed at the surface is slightly larger.

Hourly time series are subdivided in 71 semi-overlapping blocks of 100 s. Subsequently, the spectrum, bispectrum, and bicoherence are estimated with 142 degrees of freedom (Eqs. (3.4), (3.9), and (3.10)). The wave height (Eq. (3.6)) and peak period $T_{peak} = 1/f_{peak}$ are computed from the spectrum in which f_{peak} is the frequency at which the variance is maximum. The observed bound wave height is computed following the method of HEG94 (Eqs. (3.21) and (3.22)). The focus is on the bound variance present in the superharmonic frequency range that originates from sum interactions between frequencies in the sea-swell range. Therefore, interactions involving components in the infragravity range should be excluded. This is done by using a frequency cut-off separating sea-swell and infragravity wave frequencies, here defined as $f_{peak}/2$ following Roelvink et al. (2009). Hence, the index i_{min} is defined such that $f_{i_{min}} = f_{peak}/2$.

At F4 and F5, where collocated measurements of pressure and velocity are present, the 2D frequency-directional spectrum is computed using the Maximum Entropy Method (Lygre & Krogstad, 1986) with $\Delta\theta = 5°$, from which the energy-weighted mean direction θ_w and directional spreading σ_{θ_w} are computed. In this chapter, directions are presented in a Cartesian convention, thus the direction in which the wave is propagating is measured counterclockwise from the east. At the other locations, the normalized directional distribution of the closest frame is used in order to construct the 2D spectrum from the measured pressure spectrum using Equation (3.7). Subsequently, at all locations the predicted bound wave height is obtained using Equations (3.15) and (3.16). In order to make a fair comparison between the predicted and observed bound wave heights, they need to be calculated over the same frequency range, such that the same triad interactions are included in both estimates. This is done by using the same index i_{min} as described in the previous paragraph. The uncertainty introduced by using a nearby directional distribution Θ on the calculation of $H^{nb}_{b,pred}$ is discussed in Section 3.6.1.

In a few rare occasions, some minimal variance (at most 10% of the total) is present in directional bins opposing the peak incoming wave direction. These could not be explained by the concurrent wind conditions nor crossing sea states, and are most likely an artifact of the method used to construct the frequency-directional spectra. As the nonlinear interaction coefficient can be orders of magnitude stronger for opposing wave components (Herbers & Guza, 1991), this minimal amount of variance can adversely affect the bound wave height prediction. Furthermore, these opposing components do not contribute to the sea-swell wave shape of interest because their bound wave length is much longer than the primary waves. Therefore, contributions to the predicted bound wave height for interactions with $D < 0$ are not taken into account.

The tidal current is a ubiquitous feature on an ebb-tidal delta. Its presence causes a shift between the absolute frequency ω and relative frequency σ, the Doppler shift. Formally wave theories, as used by Hasselmann (1962), are valid in a moving frame of reference (Fenton, 1990; Hedges, 1995), thus using the relative frequency. This requires, however, that the current magnitude in direction of wave propagation is known, which is not the case at the seven standalone pressure sensors. Estimating the current in the direc-

tion of wave propagation U_n at these locations would require a number of assumptions on wave refraction and the evolution of the current over the complex bathymetry. Therefore, it is decided to use ω at all sensors to compute k using the linear dispersion relationship. Subsequently, ω and k are used to determine D. The mismatch in frequency and wavenumber at the frames where velocities are measured is on average 3% and at most 10%. This mismatch is expected to be larger at the shallower sensors where k and U_n are both expected to increase. The uncertainty on $H^{nb}_{b,pred}$ introduced by this mismatch is discussed in Section 3.6.1.

Wave shape parameters (Sk_p, As_p, and S_p) are calculated from the near-bed pressure-head bispectrum (using Equations (3.12–3.14)). In order to obtain the wave shape associated with bound superharmonics and to be consistent with the bound wave height formulations, only interactions in the bispectrum with $f > f_{peak}/2$ are included.

3.4.3. DATA SELECTION AND OVERVIEW

For this study, it is chosen to only present cases in which the wave height at P1 exceeds 0.5 m. Cases with a lower wave height showed a negligible amount of bound variance as well as near-zero Sk_p and As_p, and are therefore disregarded in this chapter. After this data selection, a total of 347 one-hour cases are included in this study. The majority of these cases (287) occurred during two storm events that coincided with the field campaign. To give an idea of the conditions, the wave height, period, direction, and mean water level at F4 during these two storms are shown in Figure 3.2. Another 60 cases outside of these storms are included, which occurred during four smaller events with $0.5 < H^{nb} < 1$ m. When all 9 sensors are considered, this results in 3123 data points.

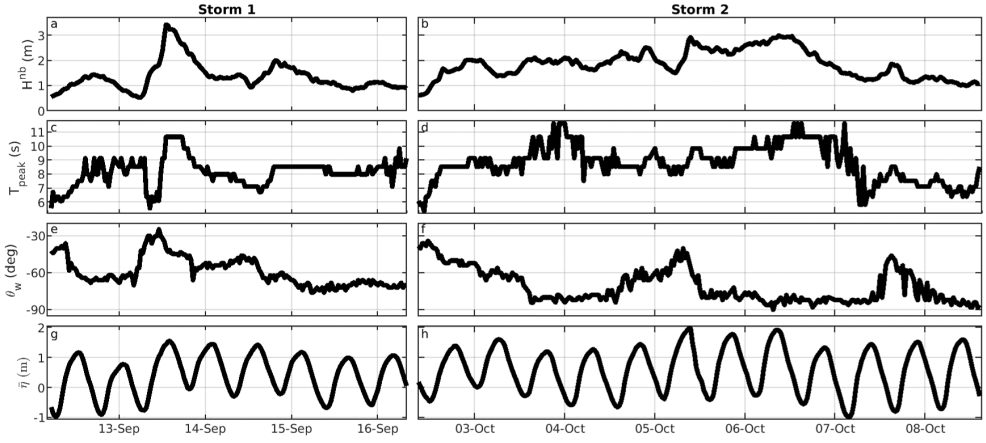

Figure 3.2: Overview of H^{nb} (**a**,**b**), T_p (**c**,**d**), θ_w (**e**,**f**), and the mean water level $\bar{\eta}$ (**g**,**h**) at F4 during storm 1 (left column) and storm 2 (right column).

3.5. RESULTS

3.5.1. SPATIAL EVOLUTION OF THE SPECTRUM AND BISPECTRUM

This section discusses the spatial evolution of the spectrum, bispectrum, and associated wave statistics. First, results are shown for a single burst on 4th October, 12:00 (Figure 3.3) representing storm conditions with a H^{nb} of 1.9 m, a T_p of 10 s, and a mean direction θ_w of $-72°$ around slack tide. Subsequently, all bursts are combined in order to analyze general trends and the variability from these trends for all locations (Figure 3.4).

Figure 3.3 shows the wave spectra (panels (a–d)) as well as the real (panels (e–h)), and imaginary (panels (i–l)) parts of the bispectra at four locations along the main transect (see Figure 3.3p for the position of the selected sensors). As expected in these energetic conditions, waves break when they reach the outer slope of the ebb-tidal shoal resulting in significantly lower variance levels at the shallowest sensors P2 and P4 (Figure 3.3c,d) than at F4 and F5 (Figure 3.3a,b). In addition to the primary sea-swell peak at f_{peak} = 0.1 Hz, two secondary peaks can be clearly identified at the deepest selected locations, one in the infragravity range ($f < f_{peak}/2$), reaching maximum variance below 0.02 Hz, and another one around 0.2 Hz, i.e., at $2f_{peak}$. The large (absolute) values of the real and imaginary part of the bispectra around (f_m, f_n) = (0.1 Hz,0.02 Hz) and (0.1 Hz,0.1 Hz) indicate that variance at these secondary peaks is, at least partly, nonlinearly coupled to the sea-swell primary peak. In the following, we focus on interactions between sea-swell frequencies as they are responsible for the buildup of the bound super harmonic variance. This means that interactions involving infragravity waves are excluded from further analysis. The importance of properly separating infragravity and sea-well variance can be understood by looking at the bispectrum at for instance F4. Including interactions containing one frequency in the infragravity wave range and one in the sea-swell range (blue part in Figure 3.3e and red part in Figure 3.3i) would lead in this case to a lower (higher) integrated value for $\Re\{B\}$ ($\Im\{B\}$), modifying not only skewness and asymmetry but also the bound wave height estimate (see Equations (8), (9), (24), and (25)).

The magnitude of the real and imaginary parts of the bispectrum varies significantly along the transect (see changes in color scale in Figure 3.3e–l). At F4 and F5, the real part of the bispectrum is positive over the entire sea-swell range and of considerably larger magnitude than the imaginary part. This suggests that sea-swell waves are skewed, but not asymmetric, which is common for waves in deeper water that are not close to the breaking limit. At P2, the real and imaginary parts of the bispectrum are of the same order of magnitude, with $\Re\{B\}$ positive over the full sea-swell frequency range and $\Im\{B\}$ mostly negative. This means that waves are both skewed and asymmetric (saw-tooth shaped) at this location. Moreover, the consistently negative value of $\Im\{B\}$ around (f_{peak}, f_{peak}) at F4, F5, and P2 indicates that variance is being transferred from f_{peak} to the sum frequency $2f_{peak}$ along most of the transect [3], including at P2 where waves are already breaking. This nonlinear energy transfer contributes to the observed growth in variance of the first higher harmonic ($2f_{peak}$) from F4 to P2, although other processes, such as (linear) shoaling and the changes in wave-induced pressure attenuation with depth also play a role. Finally, at

[3] Different sign conventions can be found in the literature for the imaginary part of the bispectrum. In the present chapter, we adopt the same representation as Norheim et al. (1998), in which a negative value of $\Im\{B(f_1, f_2)\}$ is indicative of an energy transfer from f_1 and f_2 to $f_1 + f_2$. Note that the opposite convention is used in, e.g., Herbers & Burton (1997) and De Bakker et al. (2015).

P4, i.e., landward of the shallowest point of the ebb-tidal shoal, the magnitude of both $\Im\{B\}$ and $\Re\{B\}$ has significantly decreased while the total variance stays close to the one observed at P2. This suggests a weaker nonlinear coupling, and thus a decrease in bound wave variance, as well as more linear wave shapes.

These trends are confirmed when looking at the evolution of the integrated wave statistics for all nine sensors (Figure 3.3m–o). Initially, the total sea-swell wave height H^{nb} very gradually increases from P1 to F5 before significantly decreasing from F5 to P2 (Figure 3.3m). The bound superharmonic wave height, $H^{nb}_{b,obs}$, increases at a much higher rate than H^{nb} as waves propagate over decreasing water depth (Figure 3.3n), which is consistent with the variance increase observed at $2f_{peak}$ in Figure 3.3a–c. Interestingly, $H^{nb}_{b,obs}$ keeps increasing beyond F5, while the total sea-swell wave height H^{nb} is already decreasing due to breaking. $H^{nb}_{b,obs}$ finally decreases from P2 to P4 while H^{nb} stays almost constant. This suggests a release of bound higher harmonics over the shoal, as was observed under laboratory conditions by Beji & Battjes (1993).

Finally, the evolution of the dimensionless wave shape parameters is visualized in Figure 3.3o. The skewness (Sk_p) gradually increases while moving into shallower water towards a maximum at P2 before it starts decreasing. In contrast, the asymmetry (As_p) is near-zero for most locations and is only of significance at P7 and P2, the two locations where the wave height is significantly decreasing and where the portion of breaking waves is expected to be the largest. As a consequence, the combined nonlinearity parameter S_p is close to the Sk_p except for P7 and P2, where the contribution of the As_p makes S_p slightly higher than Sk_p.

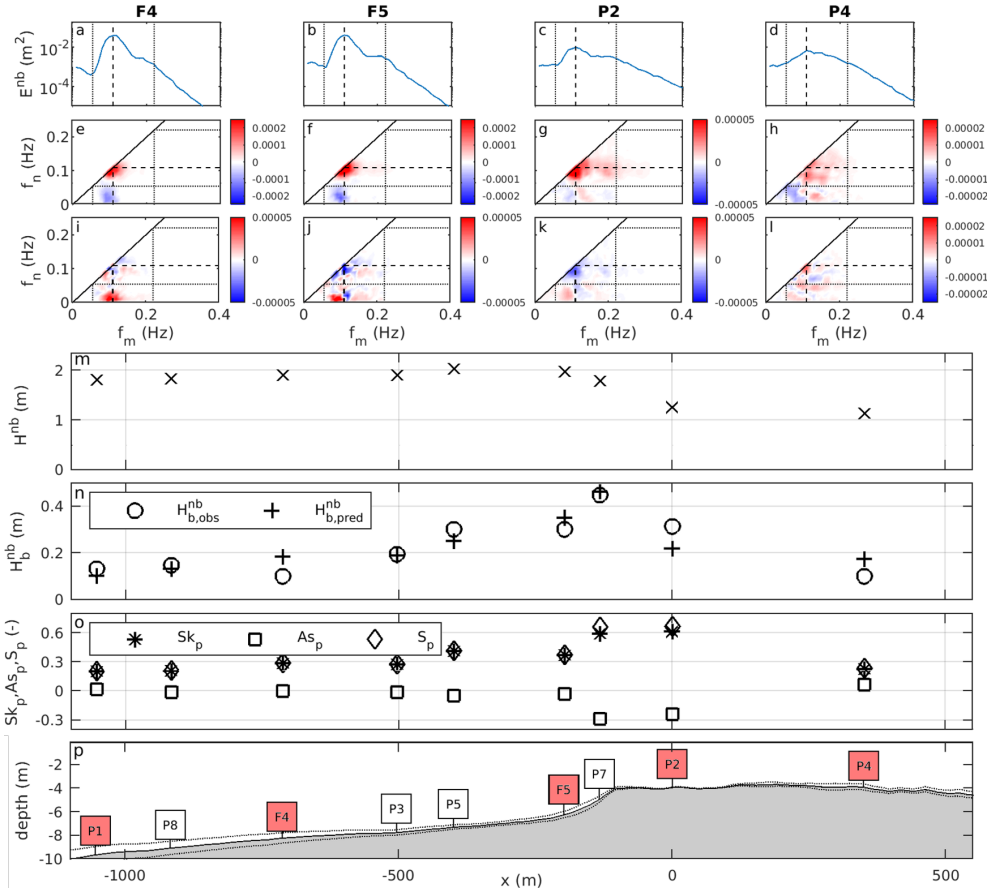

Figure 3.3: Characterization of the wave field for a selected burst on 4 October 2017 at 12:00. Panels (a–l) show the spectrum (a–d), real part of the bispectrum (e–h) and imaginary part of the bispectrum (i–l) at locations F4, F5, P2, and P4. Panels (m–p) show the evolution of the sea-swell wave height H^{nb} (m); the observed and predicted bound wave height in the super harmonics, $H^{nb}_{b,obs}$ and $H^{nb}_{b,pred}$ (n); and dimensionless sea-swell wave shape parameters Sk_p, As_p, and S_p (o) at all locations (see panel (p) for information on the deployment depths). The dashed lines in the spectra and bispectra indicate f_{peak}, the dotted lines $f_{peak}/2$ and $2f_{peak}$. The thick black diagonal lines in the bispectra are the symmetry lines. Note that the limits of the color scales for the bispectral plots are not all the same. The bathymetry of the main transects is shown in panel p, with ± one standard deviation indicated by black dashed lines representing bathymetric variability for cases with non-oblique incoming wave directions ($-45^\circ < \theta_w < 45^\circ$). Sensor locations are indicated by the red (if sensor is on main transect) and white boxes (if sensor is not on main transect; sensor is placed such that the mean depth is the same as the depth on the main transect).

The data analysis as presented above for the single case on 4th October is performed for all cases and the wave statistics and their variability is shown in Figure 3.4. The data is divided in two groups based on the significant wave height at the most offshore location (P1). Group 1 (black lines in Figure 3.4) contains all cases with $1 \leq H^{nb}_{P1} \leq 2$ m and Group 2 (red lines in Figure 3.4) contains all cases with $H^{nb}_{P1} \geq 2$ m. As expected, larger offshore waves (Figure 3.4a) lead to larger bound waves (Figure 3.4b) and more nonlinear wave

shapes (Figure 3.4d). This figure also confirms the difference in the spatial evolution of H^{nb} and $H^{nb}_{b,obs}$ observed already for the single data burst presented above. It shows that for the energetic cases (Group 2), the maximum value of $H^{nb}_{b,obs}$ is systematically found in the area where H^{nb} is already decaying due to breaking.

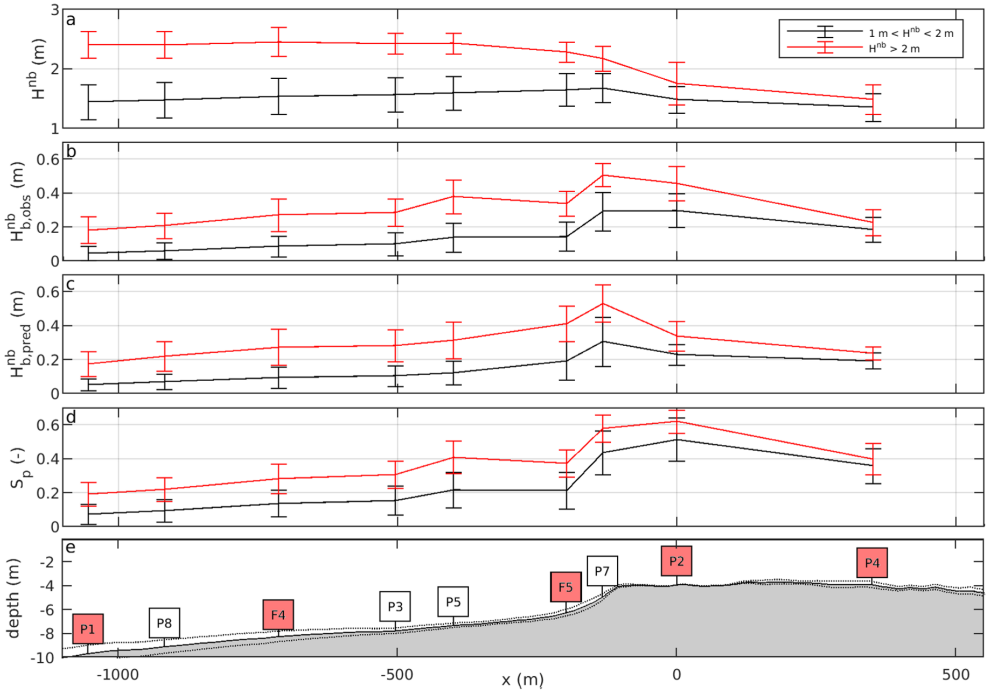

Figure 3.4: The spatial evolution of averaged wave statistics: H^{nb} (**a**), $H^{nb}_{b,obs}$ (**b**), $H^{nb}_{b,pred}$ (**c**), and S_p (**d**) along the main transect (**e**) for Group 1 (black lines, 1 m $\leq H_{P1} \leq$ 2 m) and Group 2 (red lines, $H^{nb}_{P1} \geq$ 2 m). The error bars indicate ± one standard deviation. For a description of the bathymetric transect (**e**) see the caption of Figure 3.3.

3.5.2. PREDICTED AND OBSERVED BOUND WAVE HEIGHT

The evolution of $H^{nb}_{b,pred}$ across the measurement transect is displayed in Figure 3.3n for the earlier selected burst and in Figure 3.4c for the entire dataset. From these figures, it can be seen that $H^{nb}_{b,pred}$ increases at a similar rate as $H^{nb}_{b,obs}$ up to sensor P7, where they both reach their maximum values but that the mismatch between predicted and observed bound wave heights increases when the depth decreases. After P7, the trends exhibited by $H^{nb}_{b,obs}$ and $H^{nb}_{b,pred}$ differ more significantly, with in particular a much stronger decrease in $H^{nb}_{b,pred}$ than in $H^{nb}_{b,obs}$ when waves propagate from P7 to P2.

Overall, these first comparisons suggest that the ability of the Hasselmann (1962) theory to predict the bound wave height, as implemented in Section 3.3.1, varies spatially. To examine this in more detail, the data is clustered in three regions: the shelf (P1, P8, F4, P3, and P5), the seaward slope (F5 and P7), and the ebb-tidal shoal (P2 and P4). Figure 3.5

shows the observed bound wave height as a function of the predicted bound wave height for these different regions.

At the shelf (Figure 3.5a), the predicted bound wave height is very similar to the observed bound wave height with a strong correlation coefficient ($R^2 = 0.94$) and a linear regression slope of 0.96 suggesting that the observed bound wave response is in equilibrium with the local sea-swell forcing. At the steeper seaward slope (Figure 3.5b), the correlation between the predicted and observed bound wave height is still high ($R^2 = 0.93$), but the slope of 1.11 reveals a slight overestimation of the predicted bound wave height. This over prediction is consistent with non-equilibrium conditions where at the steeper part of the slope waves experience rapid changes in depth inhibiting the higher harmonics to fully develop.

On top of the shoal and right behind it (Figure 3.5c) the predicted bound wave height deviates significantly from the observed bound wave height (lower correlation coefficient $R^2 = 0.72$ and a slope of 0.80). Although this linear regression slope indicates an underestimation of the predicted bound wave height on average, Figure 3.5c shows that the predicted bound wave height is both under- and overestimated, depending on the conditions. At these relatively shallow locations the changes in sea-swell conditions are controlled by wave breaking, rapid refraction and wave current interaction and as such the equilibrium theory of Hasselmann (1962) is not expected to hold. The errors introduced by currents, wave breaking, and directionality, and their effects on the predicted bound wave height are further discussed in Section 3.6.1.

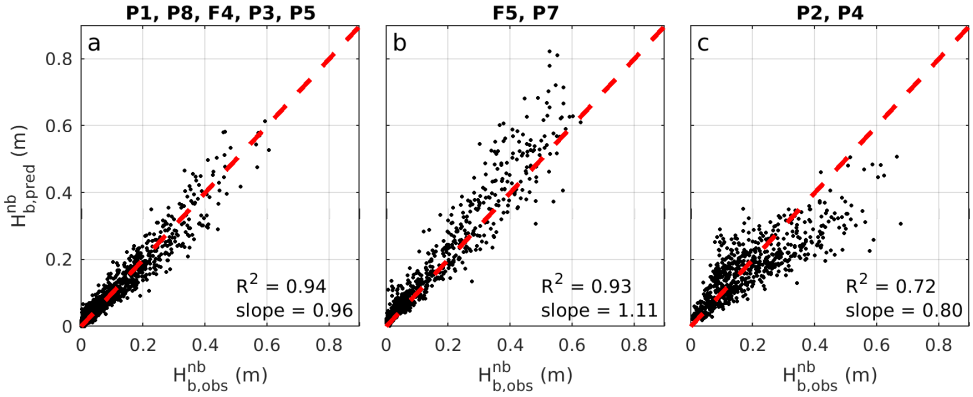

Figure 3.5: Predicted bound wave height as a function of the observed bound wave height at the shelf (panel **a**: P1, P8, F4, P3, and P5), the seaward slope (panel **b**: F5 and P7), and the ebb-tidal shoal (panel **c**: P2 and P4). The red dashed line has slope 1.

3.5.3. WAVE SHAPE AS A FUNCTION OF OBSERVED BOUND WAVE HEIGHT

The relationship between the wave shape and bound wave height is examined next. Figure 3.6 shows the dimensionless combined wave shape parameter S_p as a function of the dimensionless predicted and observed bound wave height over sea-swell wave height ratios $H^{nb}_{b,obs}/H^{nb}$ and $H^{nb}_{b,pred}/H^{nb}$, respectively. There is a very strong correlation, $R^2 = 0.99$, between the wave shape and the observed bound to total wave height ratio (Fig. 3.6a). This strong relation between S_p and $H^{nb}_{b,obs}/H^{nb}$ was expected, as S_p and $H^{nb}_{b,obs}/H^{nb}$

are both computed by summing over the bispectrum and subsequently normalizing by the variance to some power. More specifically, S_p is obtained after dividing by the variance to the power 3/2 (see Equations (3.12) and (3.13)), while the bound wave height ratio is obtained after division by the significant wave height, i.e., the variance to the power 1/2. The strong relation between S_p and H_b^{nb}/H^{nb} suggests a mathematical connection between the two variables that still needs to be established. The small scatter around the best fit line can be partly explained by the reliability of the estimated spectrum and bispectrum. Additional tests (not shown) have indeed revealed that the scatter decreases for increasing number of degrees of freedom (DOFs). Although this relationship between dimensionless wave shape and bound wave height may seem trivial, to the authors knowledge, it has not been presented before.

The correlation between wave shape and bound wave height deteriorates significantly using the predicted bound wave height, $H_{b,pred}^{nb}$ (right panel of Figure 3.6) with $R^2 = 0.80$. The observed scatter is related to the mismatch in predicted bound wave height with respect to the observed bound wave height (presented in Figure 3.5). Although scatter is present, the predicted value is reasonable for cases with a low proportion of predicted bound wave height $H_{b,pred}^{nb}/H^{nb} < 0.15$. For cases with a higher proportion of predicted bound wave height, the scatter increases, and thus the predictive skill decreases accordingly. It is for those cases where other commonly used wave shape parametrizations based on equilibrium conditions (Isobe & Horikawa, 1982; Doering & Bowen, 1995; Ruessink et al., 2012) also struggle to accurately predict the wave shape. Here, improvements in wave shape predictions can be readily obtained with better model predictions of the bound wave height ratio, as is evident from the comparison of the panels in Figure 3.6. Once the error in the predicted bound wave ratio is understood, it opens up the avenue for future modeling perspectives as discussed in the next section.

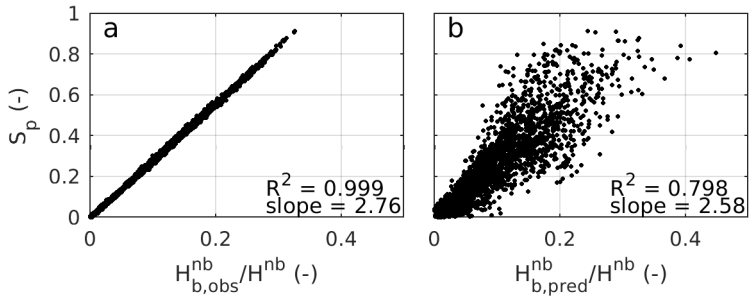

Figure 3.6: Dimensionless wave shape as a function of the dimensionless observed bound wave height (**a**) and the dimensionless predicted bound wave height (**b**) for all locations combined.

3.6. DISCUSSION

3.6.1. ERRORS IN DETERMINING THE PREDICTED BOUND WAVE HEIGHT

Despite the fact that there is an acceptable agreement between the predicted and observed bound wave height in deeper water, a significant mismatch between the two is observed once it gets shallower (see Figure 3.5). In this latter part, the effects of direc-

tional spreading, ambient currents, and wave breaking on the prediction of the bound wave height are prevalent and discussed next.

DIRECTIONAL SPREADING

A source of uncertainty is introduced by the assumptions required to obtain the frequency directional spectrum at the locations where velocities were not measured. A marginal spatial difference in directional spreading is observed between F4 and F5 (root mean squared difference is 4°), from which it can safely be assumed that the directional distribution at the other deeper located pressure sensors (P1, P8, P3, and P5) will not be too different. At the shallower locations (P7, P2, and P4), however, significant changes in depth and currents could lead to both an increase or decrease of the directional spreading. Easy ways to compute the refraction commonly rely on parallel depth contours are not applicable in this study due to the complex bathymetry. Therefore, this section discusses the effect a larger or smaller directional spreading has on the subsequent computation of $H^{nb}_{b,pred}$ (Equation (3.16)).

A study by Herbers et al. (1999) observed a maximum difference in directional spreading of 10° along a cross-shore transect in the nearshore zone. This study was conducted in shallower and more nonlinear environment than our field campaign. Therefore, it is assumed that a mismatch of 10° in directional spreading is an upper limit. The normalized directional distribution Θ is adapted such that the observed directional spreading is varied by plus or minus 10°. This is achieved by taking the observed directional distribution to the power P and subsequently normalize it again to ensure that the sum of Θ is one for each frequency bin and hence the frequency distribution of the variance is not being affected:

$$\Theta_{new} = \frac{\Theta^P}{\sum \Theta^P}. \tag{3.23}$$

$P > 1$ gives more weight to the energetic directional bins, making the directional distribution narrower and thus decreasing the directional spreading. Conversely, $P < 1$ results in an increased directional spreading. For each burst, P is obtained using an optimization routine to obtain the desired 10 degree increase or decrease in the observed directional spreading. Figure 3.7 shows that an increased or decreased directional spreading of 10° leads to an underestimation of 8% and an overestimation of 9% of $H^{nb}_{b,pred}$, respectively. Because a difference in directional spreading of 10 degrees is expected to be an upper limit in this location, the error introduced by using a wrong directional distribution is less than 9%.

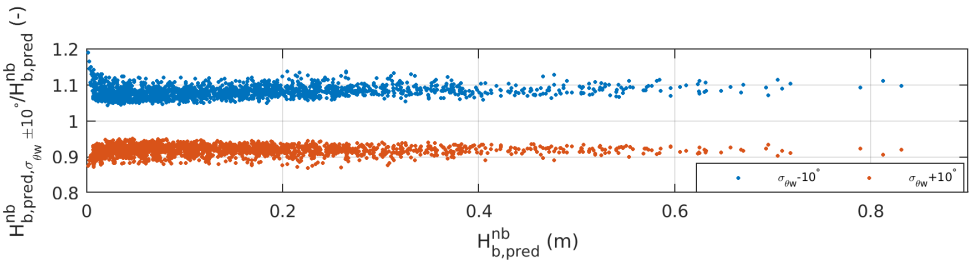

Figure 3.7: Predicted bound wave height $H^{nb}_{b,pred,\sigma_{\theta_w}\pm10^{\circ}}$ calculated for an increased (red: $+10^o$) and decreased (blue: -10^o) directional spreading over the original bound wave height prediction $H^{nb}_{b,pred}$ as a function of $H^{nb}_{b,pred}$ for all sensors.

3

CURRENT

Tidal inlets are characterized by strong ebb and flood currents. It is known that these currents affect the wave dynamics due to wave current interaction and lead to a Doppler shift. This Doppler shift describes the difference between the absolute frequency ω (as observed at one fixed location) and the relative frequency σ (as observed in a frame of reference moving with the current):

$$\omega = \sigma + kU_n \tag{3.24}$$

in which U_n is the current magnitude in direction of wave propagation. In absence of an ambient current $\sigma = \omega$, whereas in presence of following ($U_n > 0$) and opposing ($U_n < 0$) currents $\sigma < \omega$ and $\sigma > \omega$, respectively. A given observed absolute frequency thus results in a smaller wavenumber k for following than for opposing currents.

The nonlinear interaction coefficient D, as used in Equation (3.16), is higher for longer waves (lower σ and k) than for shorter waves. However, as no reliable estimates of the current magnitude and direction were available at most measurement locations, ω and the corresponding k were used to obtain $H^{nb}_{b,pred}$ without taking into account the tidal current. This could lead to an over or underprediction of $H^{nb}_{b,pred}$ depending on the current direction.

The influence of the current on the over and under prediction of $H^{nb}_{b,pred}$ is visualized in Figure 3.8, where the color of the data points indicates following currents (red dots: $U_n > 0.1$ m/s), no currents (gray dots: -0.1 m/s $< U_n < 0.1$ m/s), and opposing currents (blue dots: $U_n < -0.1$ m/s). The current direction, magnitude, and wave direction at F4 are used to distinguish the different current conditions because the most reliable directional estimates were obtained at that location.

At the deeper sensor F4, no clear correlation is seen between the over and under prediction of $H^{nb}_{b,pred}$ and U_n (Figure 3.8a). However, the shallower it gets, the more evident the effect of the current on the over- and underprediction of $H^{nb}_{b,pred}$ is (Figure 3.8b–d). The reason why the influence of the ambient current is more significant in shallower water is related to the relative importance of the Doppler shift. This importance is described by the ratio kU_n/σ or as U_n/c in which c is the wave celerity. In deeper water, the current

magnitude is lower and the celerity is higher, resulting in a marginal influence of the current. However, in shallower water, the current magnitude increases whereas the celerity decreases, making the importance of including the current more and more important.

To separate the possible effect of wave breaking from current effects in shallower water, sensor P4, located in a deshoaling zone and as such only marginally affected by wave breaking, is examined in more detail. At P4 (Figure 3.8d), for cases with a following current, on average the ratio of $H^{nb}_{b,pred}/H^{nb}_{b,obs}$ is 0.78, whereas for cases with an opposing current this ratio is 1.38. Therefore, a significant part of the scatter observed in Figure 3.5c is related to the under- and overestimation of $H^{nb}_{b,pred}$ for opposing and following conditions, respectively. $H^{nb}_{b,pred}$ is under predicted in following current conditions, as the waves are actually longer than measured at the fixed measurement location. These longer waves should have a higher D and thus a higher predicted bound wave height. Vice versa, in opposing current conditions, the waves are shorter than measured, so $H^{nb}_{b,pred}$ is overpredicted.

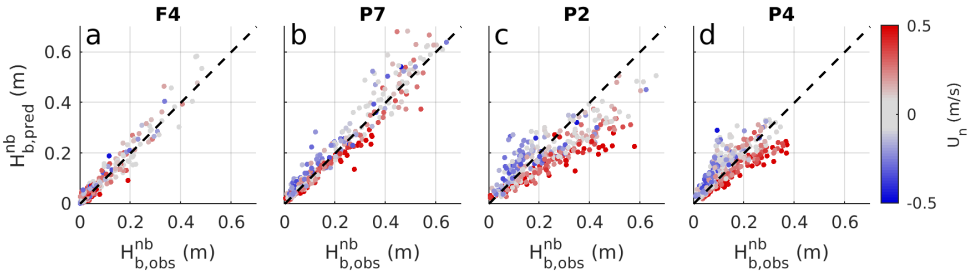

Figure 3.8: $H^{nb}_{b,pred}$ as a function of $H^{nb}_{b,obs}$ at F4 (a), P7 (b), P2 (c), and P4 (d) where the color indicates the current in direction of wave propagation U_n (blue = opposing currents, red = following currents).

WAVE BREAKING

In the following, (near-)breaking conditions are defined as bursts for which $As_p < -0.2$. Using this criterion most wave breaking is observed at P7 and P2. To eliminate the previously discussed effect of the current at these two locations, a subset of 175 bursts is considered where the current in direction of wave propagation is negligible ($|U_n| < 0.1$m/s), of which 53 and 50 meet the breaking criteria at P7 and P2, respectively. At P7, $H^{nb}_{b,pred}$ is higher than $H^{nb}_{b,obs}$ for 43 out of 53 breaking cases with an average over estimation of 13% (see Figure 3.9a). In contrast, at P2 $H^{nb}_{b,pred}$ is lower than $H^{nb}_{b,obs}$ for 47 out of 50 cases with an average under estimation of 23% (see Figure 3.9b).

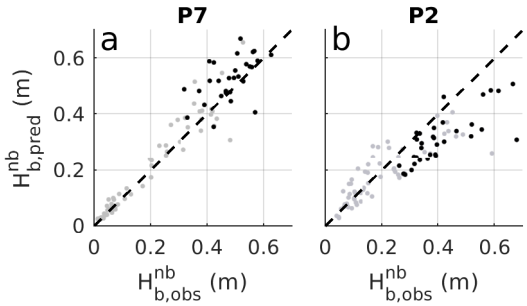

Figure 3.9: $H^{nb}_{b,pred}$ as a function of $H^{nb}_{b,obs}$ at P7 (a) and P2 (b) for the subset of data with small currents ($|U_N| < 0.1$ m/s) with black markers for (near-)breaking conditions ($As < -0.2$) and gray markers for non-breaking conditions.

A probable cause for the overestimation of the breaking waves at P7 was already discussed in Section 3.5.2, where it was explained that the wave shape can not instantly change in the rapidly changing bathymetry. The underestimation at P2 also seems to be related to the rapidly changing conditions. Due to wave breaking, significant energy loss is seen in the primary wave components. As $H^{nb}_{b,pred}$ is proportional to the primary wave energy (Equation (3.16)), it decays at approximately the same rate as H^{nb}. It is known, however, that breaking conditions coincide with negative asymmetry, thus a negative imaginary part of the bispectrum, and as a result nonlinear energy transfers towards the bound higher harmonics. Therefore, although H^{nb} is decaying due to wave breaking, this positive energy transfer can lead to a growth of $H^{nb}_{b,obs}$. Additional support for this explanation can be found in Figure 3.4. Here, for the highly energetic cases (red lines) only a minor decrease in $H^{nb}_{b,obs}$ is observed from P7 towards P2, whereas the decay in H^{nb} and $H^{nb}_{b,pred}$ is much stronger. The fact that $H^{nb}_{b,obs}$ decreases does not conflict with the earlier mentioned positive nonlinear energy transfer because the spatial change in variance is also affected by wave breaking, shoaling, and depth attenuation of the pressure signal.

OVERALL VALIDITY OF EQUILIBRIUM BOUND WAVE HEIGHT THEORY

In the previous sections it is shown that a small amount of error in $H^{nb}_{b,pred}$ is introduced by the unknown directional distribution at the shallow sensor but that more error is introduced when strong currents are present or when conditions are (near-)breaking. However, even when excluding cases with a strong current or (near-)breaking conditions, still a significant under or over estimation of $H^{nb}_{b,pred}$ is observed. This is related to the validity region of the wave theory used by Hasselmann (1962).

Many different definitions can be found in literature for the applicability region of the second order wave theory. Most of these describe the validity as a function of the Ursell number (e.g., Stokes, 1880; Ursell, 1953; Longuet-Higgins, 1956), a dimensionless nonlinearity parameter. Here, we follow the definition as provided by Ruessink et al. (2012):

$$Ur = \frac{3}{8}\frac{H}{k^2 d^3} \tag{3.25}$$

Le Méhauté (1976) showed that second order theory is only valid for $Ur < 0.1$. Both Madsen (1971) and Guza & Thornton (1980) state a different value of $Ur = 0.25$, based on the argument that second order theory performs well as long as the secondary amplitude is at least 4 times smaller than the primary amplitude. According to Hedges (1995), however, second-order Stokes theory can be used until $Ur = 0.38$. To investigate the consistency between the second order wave theory validity regions and the findings from our study, the RMSE between $H^{nb}_{b,pred}/H^{nb}$ and $H^{nb}_{b,obs}/H^{nb}$ is calculated for cases with low nonlinearity ($Ur < 0.25$) and high nonlinearity ($Ur > 0.25$). The threshold of 0.25 is used as it is an average of values found in literature. It is chosen to present the RMSE between the dimensionless wave height as this is used as a predictor for the wave shape. Cases with ambient currents and (near-)breaking conditions are excluded for the calculation of the RMSE. The RMSE between $H^{nb}_{b,pred}/H^{nb}$ and $H^{nb}_{b,obs}/H^{nb}$ is only 0.012 for cases with $Ur < 0.25$ whereas it is 0.050 for cases with $Ur > 0.25$, showing that the validity of second order wave theory also restricts the predictive skills of the bound wave shape.

In conclusion, it can be said that the wave shape can be accurately predicted using second order wave theory as long as waves are not breaking and nonlinearity is not too high. Furthermore, a proper prediction of the bound wave height requires directional information and, in presence of strong currents as in this study, information about the current field to properly account for the effect of the Doppler shift on the wavenumber.

3.6.2. APPLICABILITY IN DIFFERENT AREAS

The disadvantage of many wave shape parametrizations is that they are site-specific, which means that they are only applicable for certain locations or conditions. In order to test the applicability of the findings of this chapter, two additional datasets are analyzed. Although the SEAWAD dataset covers a wide range of conditions, it is limited in two ways: First, the shallowest sensors were in a mean water depth of 4 m, which limits kd to a minimum value of 0.4. Second, the wave periods observed during the campaign were rather short due to the fetch-limited conditions which are typically found in the North Sea. The two datasets that are used to validate the relationship between bound wave height and wave shape are the COAST3D (Soulsby, 1999; Ruessink et al., 2001; Van Rijn et al., 2002) and SandyDuck (Birkemeier et al., 1997; Reniers et al., 2004) campaigns.

The COAST3D data was collected during a 6-week field campaign that took place at the beach of Egmond aan Zee in the Netherlands. It is thus mostly dominated, as SEAWAD, by wind-sea waves (T_p = 6–12 s) but includes data in shallower depths. The SandyDuck dataset includes on the other hand 5 weeks of measurement along the North Carolina coast, and is therefore characterized by longer and more regular swell waves (T_p = 12–20 s).

For both datasets, all bursts corresponding to a mean water depth below 0.5 m are discarded to exclude data that could be intermittently dry. For COAST3D, this selection results in a total of 5015 one-hour long pressure timeseries collected at nine locations in a mean depth ranging between 2.1 and 5.2 m. For SandyDuck, this means that a total of 1115-hour-long time series from seven pressure sensors are analyzed, covering a water depth range from 0.7 to 4.0 m.

The relationship between the dimensionless observed bound wave height and the dimensionless wave shape is presented in Figure 3.10 for the three campaigns. Note that

observations at multiple locations are combined per campaign. For all campaigns the correlation coefficients are larger than 0.98, confirming the relationship between the bound wave height and wave shape. Furthermore, the slope of the linear regression line is fairly similar, between 2.7 and 2.8, indicating that the relationship between these two parameters is not specific to a certain area or conditions. This shows that the wave shape is known if it is possible to predict the bound wave height, independently of the area or conditions. The best linear fits between S_p and $H^{nb}_{b,obs}$ (red lines in Figure 3.10) are presented for each field campaign. It can be seen that slightly more scatter is present for data points from the shallower field campaigns. The points that deviate the most from the relationship are shallow cases, in which significant infragravity variance was present in the spectrum (not shown).

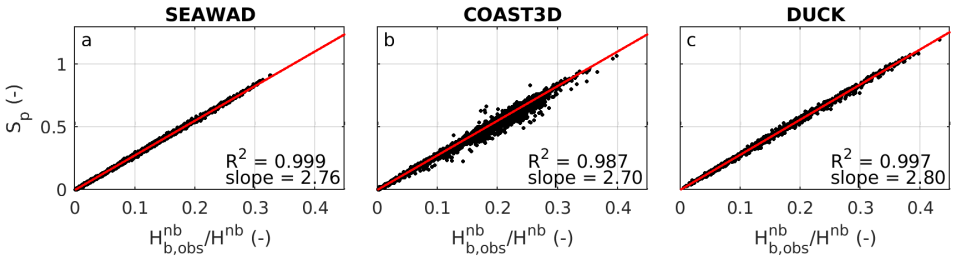

Figure 3.10: Dimensionless wave shape as a function of the dimensionless observed bound wave height for the SEAWAD (**a**), COAST3D (**b**), and SandyDuck (**c**) field campaigns. The red lines are the best linear fit through the origin per campaign.

3.6.3. FUTURE MODELING PERSPECTIVE

This chapter shows that there is a direct relationship between the bound wave height and the wave shape regardless of location or type of conditions (see Figure 3.6). Therefore, with a properly predicted spatial and temporal evolution of the bound wave height the wave shape is known, which would in turn be instrumental for accurate calculations of the wave shape induced sediment transport (Roelvink & Stive, 1989; Hoefel & Elgar, 2003; Drake & Calantoni, 2001). Predictions of the equilibrium-bound wave height using second-order finite depth wave theory (Hasselmann, 1962) proved to be accurate in relatively linear conditions ($Ur \lesssim 0.25$). In more nonlinear conditions, and where significant changes in bathymetry and wave conditions are observed, there is a clear mismatch between the predicted and observed bound wave height. Although using higher order wave theories to predict the bound wave height might stretch the applicability region, it will not be able to capture non-local aspects that influence the bound wave height and associated wave shape. This omission can be overcome by using an evolution equation for the bound wave height taking into account bathymetric variability. In the following we discriminate between large scale phase-averaged models and more detailed phase-resolving models.

The effects of waves in large-scale morphodynamic models are commonly accounted for by phase-averaged spectral models (e.g., Benoit et al., 1997; Booij et al., 1999), which calculate the evolution of the variance spectrum in time and space. The energy transfers to the higher harmonics due to nonlinear triad interactions can be included using a source

term function S_{nl3}. This source term has been derived from the bispectral evolution equations and is a function of the variance spectrum and a parametrized form of the biphase (e.g., Doering & Bowen, 1995; Eldeberky, 1996). The S_{nl3} source term is extensively studied in recent years and has led to more and more reliable predictions of the nonlinear energy transfers in spectral wave models (Becq-Girard et al., 1999; Salmon et al., 2016). Therefore, essentially, the variance that is transferred to the higher harmonics (bound variance) is known and the bound wave height can be estimated by integrating this energy transfer in the down-wave direction. In this way, the evolution of the bound wave height is taken into account with the expectation that this will lead to a significant improvement of wave shape predictions in the shoaling zone, where the proportion of bound harmonics is consistently growing. When the bound higher harmonics are released and/or their variance decays due to wave breaking, this simple integrative approach is expected to yield less accurate results. Further improvements in estimating the wave shape can be achieved by modeling the effects of these processes on both the spectrum and bispectrum in order to be able to more accurately predict the bound wave height in all areas and conditions.

Alternatively, the evolution of the bound wave height can be obtained from more detailed phase-resolving models. These can be divided in time-domain and bispectral models. The former resolve the spatial evolution of the surface elevation, pressure, and velocities in time (e.g., Wei et al., 1995; Madsen et al., 1997; Bonneton et al., 2011; Zijlema et al., 2011; Ma et al., 2012; Tissier et al., 2012). The latter resolve the spatial evolution of the spectrum and bispectrum (e.g., Herbers & Burton, 1997; Norheim et al., 1998; Eldeberky & Madsen, 1999). For these type of models, the computation of the bound wave height as a wave shape predictor is unnecessary as the skewness and asymmetry can directly be obtained from the time series or bispectra that are provided by these models. Unfortunately, high computational times of such models prevent their usage to drive large-scale morphodynamic models. However, these detailed models can be used to study in detail the release of higher harmonics and (bi)spectral decay due to wave breaking and their effect on the evolution of the bound wave height. Subsequently, these effects can be included in the phase-averaged spectral models by modifying the S_{nl3} source term to improve bound wave height and wave shape predictions in complex systems where equilibrium conditions do not hold.

3.7. CONCLUSIONS

This chapter shows that bispectral analysis of time series can be used to calculate the observed bound superharmonic wave height. In this study the method is applied to near-bed pressure time series, but it is also applicable for surface elevation or velocity time series. Despite several references in literature that such a methodology is not straightforward (McComas & Briscoe, 1980; Elgar & Guza, 1985; Young & Eldeberky, 1998; Sénéchal et al., 2002), we found that summing over the bispectrum in a similar way as is done by Herbers et al. (1994) for the bound subharmonic wave height, provides sufficient statistical reliability to obtain the bound superharmonic wave height from one hour time series. This does require that the methodology is restricted to the sea-swell frequencies and that this part of the bispectrum is dominated by positive sum interactions determining the bound wave height. In case difference interactions or negative sum interactions of crossing sea states contribute significantly to the bispectrum, the methodology should be

treated with more care because the positive and negative contributions to the bispectrum might cancel each other out leading to an underestimation of the observed bound wave variance.

By using measurements at nine locations in the vicinity of an ebb-tidal shoal, a clear relationship ($R^2 = 0.99$) is found between the normalized observed bound wave height and the dimensionless sea-swell wave shape: $S_p \approx 2.75 \frac{H^{nb}_{b,obs}}{H^{nb}}$. As the same relationship is found for two other data sets that were collected along sandy beaches respectively dominated by wind-sea and sea-swell wave conditions, we conclude that it is insensitive to the environmental conditions. Thus, the wave shape is known at locations where we know the bound wave height. Knowing the wave shape at any given location would significantly increase morphological modeling capabilities because the wave shape induced sediment transport is resolved more accurately. However, as time series are not available in commonly used phase-averaged models, the bound wave height can not directly be computed. As an alternative, the bound wave height can be predicted using second-order wave theory by assuming equilibrium conditions (Hasselmann, 1962). From the analysis of the field data, it is concluded that the method of Hasselmann (1962) is accurate in deeper water, but fails to accurately predict the bound wave height in (near-)breaking conditions or when nonlinearity is so high that second order wave theory is invalid. The accuracy of the predicted bound wave height is significantly improved if besides pressure also velocity measurements are known as the estimates are strongly dependent on the directional spread of the incoming sea-swell wave field.

To improve future model capabilities, a next step is to add the evolution equation of the bound wave variance to spectral wave models. By including this evolution equation the bound wave height will be better predicted than using the method of Hasselmann (1962) because it allows deviations from equilibrium conditions, which is key when considering wave transformation over rapidly changing bathymetry. The triad source term S_{nl3}, which is already included in such models, can be used as a source term for the bound wave variance. One of the challenges ahead is how to take into account the decrease of bound wave variance due to wave breaking and the release of bound superharmonics.

APPENDICES

3.A. ACCURACY OF BOUND WAVE HEIGHT FORMULATIONS

Two formulations were presented in Section 3.3.2 to estimate the bound superharmonic wave height from measured wave records, based on the work of Kim & Powers (1979) (KP79, Equation (3.19)) and of Herbers et al. (1994) (HEG94, Equation (3.22)). In the following, we evaluate the accuracy of these methods using a synthetic dataset of known bound variance content. The methodology followed to create the synthetic data is outlined in Appendix 3.A.1. As both formulations involve integrations over the spectrum and bispectrum, the outcome is expected to depend on the reliability of the (bi-)spectral estimates and thus on the number of degrees of freedom (DOFs) in their calculations. The accuracy of the bound wave height formulations is thus evaluated in Appendix 3.A.2 for varying degrees of freedom.

3.A.1. SYNTHETIC TIMESERIES

Several realizations of a nonlinear sea-state, chosen to be representative of the conditions typically measured at our field site, are generated using second-order wave theory. Each of these realizations has a duration of 100 s and is written as:

$$\eta(t) = \eta_{primary}(t) + \eta_{super}(t)$$

in which $\eta_{primary}$ and η_{super} are the surface elevation time series corresponding to the primary wave field and its first harmonics, respectively. The primary wave field is generated such that the variance E'_m at each discrete frequency f_m follows a JONSWAP shape with $H = 1$ m, $T_p = 6$ s, and an enhancement factor $\gamma_{spec} = 3.3$. From the variance spectrum the complex amplitudes are constructed as $C_m = A_m e^{i\phi_m}$ with $A_m = \sqrt{E'_m}$ and for each realization the phase at each frequency ϕ_m is randomly picked between $-\pi$ and π using a random-phase model. Eventually, the primary wave surface elevation is generated as

$$\eta_{primary}(t) = \sum_{m=-N}^{N} \left(\frac{1}{2} C_m e^{-2\pi i f_m t} + \frac{1}{2} C_m^* e^{2\pi i f_m t} \right) \tag{3.26}$$

where $f_m = m\Delta f$ with $\Delta f = 0.01$ Hz and $N = 500$. The super harmonics are then generated using the second-order theory of Hasselmann (1962):

$$\eta_{super}(t) = \sum_{m=-N}^{N} \sum_{n=-N}^{N} D(f_m, f_n, 0, 0, d) \left(\frac{1}{2} C_m C_n e^{-2\pi i f_{m+n} t} + \frac{1}{2} C_m^* C_n^* e^{2\pi i f_{m+n} t} \right) \tag{3.27}$$

where D is the interaction coefficient introduced in Equation (3.15), calculated for a depth $d = 5$ m. The target bound wave height of the time series is computed as

$$H_b^{nb} = 4 \sqrt{\sum_{m=-N}^{N} \sum_{n=-N}^{N} D^2 E(f_m) E(f_n)} \tag{3.28}$$

It should be noted that the bound wave height directly computed from the variance of the constructed time series (Equation (3.27)) slightly deviates from the target bound wave height, because it is only a single realization of finite duration. However, when averaged over a sufficient amount of independently constructed time series, the ensemble-averaged bound wave height from those time series is the same as the target bound wave height.

3.A.2. FORMULATIONS AND DEGREES OF FREEDOM

When working with observations, the number of degrees of freedom is typically increased by subdividing the measured timeseries in blocks before performing the spectral analysis or applying frequency merging (Elgar & Guza, 1988; Elgar & Sebert, 1989). Here, the use of synthetic data allows us to generate several realizations of our sea-state to estimate the expected values in the spectrum and bispectrum. The number of degrees of freedom is therefore increased by increasing the number of synthetic time series used in the calculations. The bound wave heights using Equations (3.19) and (3.22) for different DOFs are compared to the a priori known bound wave height from the time series in Figure 3.11.

A common way to characterize the statistical reliability of the bispectrum and bicoherence spectrum is to define the 95% bicoherence confidence interval, calculated as $b^2_{95\%} = \sqrt{6/d.o.f.}$. If $b^2(f_m, f_n) > b^2_{95\%}$, $B(f_m, f_n)$ and $b^2(f_m, f_n)$ are considered statistically reliable (e.g., Sénéchal et al., 2002; Guedes et al., 2013; De Bakker et al., 2015; Mahmoudof et al., 2016). To see what the effect of the bicoherence confidence interval is, Equations (3.19) and (3.22) are additionally applied with and without discarding bispectral estimates with $b^2 < b^2_{95\%}$ (solid vs dashed lines in Figure 3.11).

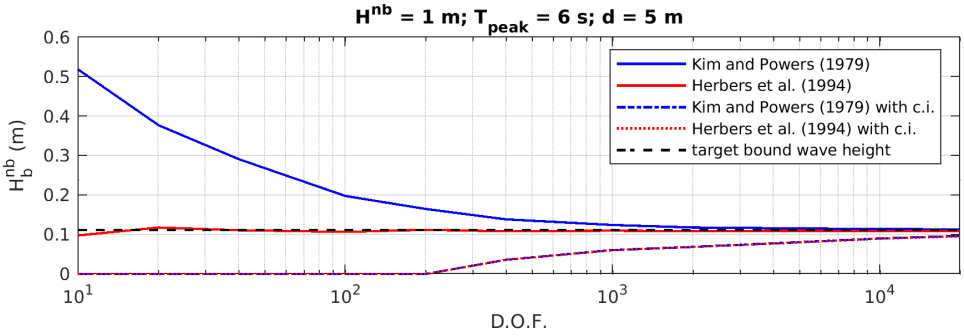

Figure 3.11: Calculated bound wave height using KP79 (Equation (3.19); blue line), HEG94 (Equation (3.22); red line), KP79 with confidence interval (Equation (3.19); blue dashed-dotted line), and HEG94 with confidence interval (Equation (3.22); red dotted line) as a function of the number of degrees of freedom. Note that the blue dashed-dotted and red dotted line are on top of each other. The black dashed line represents the a priori bound wave height.

It can be seen that the KP79 method (blue lines) needs many more DOFs to converge to the correct solution than the HEG94 method (red lines). This is because by first summing the bispectrum and energies individually instead of summing the bicoherences, additional averaging is applied, leading to more reliable estimates for less degrees of freedom. If the bicoherence 95%-confidence interval is used to discard values, both KP79 and

HEG94 underestimate H_b. The underestimation is larger for few DOFs, because of the large $b^2_{95\%}$-value that leads to the exclusion of many interactions where actual bound variance is present (all of them for the smallest values). Reasonable estimates of the bound wave height are only obtained with these methods for extremely large DOF values (>10^4).

The opposite behavior is seen for KP97 without a confidence interval. In that case the bound wave height is overestimated for all considered DOF values. This overestimation originates from the fact that, in this formulation, all interactions are considered, even the non-statistically significant ones, and that all of these interactions contribute positively to the bound wave height estimate as it depends on b^2 (Equation (3.17)).

4

WAVE SHAPE FROM A BOUND WAVE EVOLUTION MODEL

In spectral wave models, the nonlinear triad source term accounts for the transfer of energy to the bound higher harmonics. This chapter presents an extension to commonly used spectral models that resolves the evolution of the bound wave energy by keeping track of the energy that has been bound by triad interactions. This extension is referred to as the bound wave evolution (BWE) model. From this the spatial evolution of the bound wave height is obtained, which serves as a proxy for the nonlinear wave shape. The accuracy of these bound wave height and thus wave shape predictions is highly dependent on the accuracy of the triad source term. Therefore, in this study the capability of the LTA and SPB triad formulations to capture the growth of the bound wave height is evaluated. For both these formulations it is found that slope dependent calibration parameters are required. Overall, despite being computationally more expensive, the SPB method proves to be significantly more accurate in predicting the bound wave evolution. In the shoaling zone, where the bound wave energy is dominated by triads, the BWE model is well capable of predicting the nonlinear waves shape. In the surf zone, however, where a combination of triads and wave breaking control the spectral evolution, the BWE model over predicts the bound wave height. This is a result of an inaccurate representation of the spectral shape in shallower waters, affecting the proportionality factor between the bound wave height and wave shape. Nevertheless, this chapter shows the promising capabilities of spectral models to predict the nonlinear wave shape.

4.1. INTRODUCTION

In deep oceanic waters, sea-swell surface waves can generally be described by Gaussian statistics where all primary harmonics are linear and independent of each other, provided the waves are not too steep. When the waves propagate towards the coast, nonlinear interactions occur under the influence of decreasing water depth and variable ambient currents. This changes the initially harmonic wave shape into a nonlinear wave shape due to the presence of bound waves accompanying the freely propagating primary waves. The nonlinear wave shape ranges from skewed waves with steeper crests and flatter troughs to asymmetric waves where the wave front has pitched forward creating a saw-tooth wave shape at breaking. This deformation of the wave shape is also present in the near-bed velocity signal resulting in a net-onshore transport due to both skewness (Bowen, 1980; Henderson et al., 2004; Roelvink & Stive, 1989; Henriquez et al., 2010) and asymmetry (Drake & Calantoni, 2001; Hoefel & Elgar, 2003). This wave-shape induced sediment transport can be the dominant transport mechanism under certain conditions and is instrumental in properly predicting the evolution of bars (Gallagher et al., 1998; Ruessink et al., 2007) and tidal deltas (Chen et al., 2015; Reniers et al., 2019).

Morphodynamic process models are more and more applied to study the design of harbours and their access channels, the maintenance strategy of beaches and the effect of human interventions on the coastal system. In these models the wave-shape induced sediment transport is generally parameterized for computational efficiency. For instance in Delft3D initially the approach by Isobe & Horikawa (1982) was adopted, that estimates the bound wave and associated non-linear wave shape using a combination of fifth order Stokes and third order cnoidal wave theory. More recently, the wave shape parametrization of Ruessink et al. (2012), obtained from near-bed velocity data from various locations, was incorporated in the model and led to a significant improvement, as was shown by Boechat Albernaz et al. (2019). The latter parametrization predicts the wave shape as a function of the Ursell number, which is a nonlinearity parameter based on the local wave height, wave period and depth. Averaged over time and space, this parametrization generally provides a good estimate of the wave shape (De Wit et al., 2019). However, the effect of beach slope (Norheim et al., 1998; Rocha et al., 2017), spectral shape (Rocha et al., 2017), and non-equilibrium conditions (De Wit et al., 2019; de Wit et al., 2020) are not included, which are all known to influence the development of higher harmonics and thus resulting in an inaccurate prediction of the wave shape. A more accurate non-parametric alternative to estimate the wave shape is given by de Wit et al. (2020) provided that the bound sea-swell wave height or energy is known.

The previously mentioned wave shape parametrizations rely on local estimates of the significant wave height and period, which are commonly provided by spectral wave models. Various spectral wave models are available such as WAM (Monbaliu et al., 2000), WaveWatch (Tolman, 1991), TOMAWAC (Benoit et al., 1997) and SWAN (Booij et al., 1997, 1999; Ris et al., 1999). These models are all based on the concept that the wave energy propagates with the group velocity obtained from linear wave theory and that the effect of nonlinear processes such as wind growth, breaking, friction and non-linear wave interactions are accounted for by source and sink terms. This can include the transfer of energy from the free primary waves to the bound secondary waves in the case of triad interactions (Eldeberky, 1996; Becq-Girard et al., 1999; Salmon et al., 2016). However, the amount of

energy that has been transferred is not stored in the present models and thus the proportion of bound wave energy and therefore wave shape at a given instance in time and space is unknown.

To overcome this problem, in this Chapter, a bound wave evolution (BWE) equation is added to the existing wave model SWAN not only to resolve the evolution of the free primary wave spectrum, but also the evolution of the bound super-harmonic secondary wave spectrum. From this the bound wave height can be computed, which in turn can be used as a proxy for the wave shape (as shown in Chapter 3), thereby removing the need for a parameterization.

Section 4.2 introduces the spectrum, bispectrum and the wave parameters that are derived from these spectra. The incorporation of the bound wave height evolution equation is described in Section 4.3, including the underlying assumptions. The model set-up and test simulations are explained in Section 4.4. In Section 4.5 the performance of two existing triad source term formulations is evaluated, as well as the eventual prediction of the bound wave height and wave shape. Section 4.6 provides a discussion on the uncertainties associated with the modelling and Section 4.7 gives the conclusions.

4.2. THE SPECTRUM, BISPECTRUM AND WAVE SHAPE

Spectral changes in variance, the triad source term and the wave shape are all related to each other via the bispectrum. This section describes how the spectrum and bispectrum are defined, and how the wave shape and bound wave height can be obtained from those.

The surface elevation is defined as a summation of harmonics with discrete frequencies:

$$\eta(t) = \sum_{m=-N}^{N} \frac{1}{2} C_m e^{-2\pi i f_m t} + \frac{1}{2} C_m^* e^{2\pi i f_m t} \tag{4.1}$$

in which C_m and C_m^* are the complex amplitude and its complex conjugate at the discrete frequency $f_m = m\Delta f$ with Δf being the frequency resolution, i is the imaginary number, and t is time. The number of discrete spectral estimates is $2N+1$, which are bound by the Nyquist frequencies: $\pm f_N = \pm f_s/2$, in which f_s is the discrete sampling frequency of the surface elevation time series. The complex amplitudes are obtained by applying a discrete fast Fourier transformation on the surface elevation.

4.2.1. THE SPECTRUM

The double sided discrete variance spectrum is obtained from the complex amplitudes as:

$$E'_m = \mathbf{E}[C_m C_m^*] \qquad \text{for: } -N \le m \le N \tag{4.2}$$

in which **E[...]** denotes the expected value. For convenience, readability and computational efficiency the variance spectrum is instead presented as a single sided discrete variance spectrum:

$$E_m = 2E'_m \qquad \text{for: } 0 \le m \le N \tag{4.3}$$

The corresponding variance density spectrum is:

$$E(f_m) = \frac{E_m}{\Delta f} \qquad \text{for: } 0 \leq m \leq N \tag{4.4}$$

from this the sea-swell spectral moments can be calculated as:

$$m_j = \sum_{m=i_{min}}^{i_{max}} f_m^j E(f_m) \Delta f \tag{4.5}$$

in which m_j is the j-th order spectral moment and in which i_{min} and i_{max} are indices corresponding to the sea-swell frequency range. These are defined in this study as $f_{i_{min}} = f_{peak}/2$ in order to separate the sea-swell waves from the infragravity waves (Roelvink et al., 2009) and $f_{i_{max}} = f_N$. The spectral moments are used to obtain the significant wave height and spectral period estimates:

$$H = 4\sqrt{m_0} \tag{4.6a}$$

$$T_{m_{0,1}} = \frac{m_0}{m_1} \tag{4.6b}$$

$$T_{m_{0,2}} = \sqrt{\frac{m_0}{m_2}} \tag{4.6c}$$

4.2.2. THE BISPECTRUM

Analogous to the double sided variance spectrum, the discrete bispectrum is defined as:

$$B_{m,n} = \mathbf{E}[C_m C_n C_p^*] \qquad \text{for: } p = m + n \text{ and } -N \leq m, n, p \leq N \tag{4.7}$$

As a single sided form leads to awkward conventions (Hasselmann et al., 1963) the double sided form is retained here. The bispectral density is defined as:

$$B(f_m, f_n) = \frac{B_{m,n}}{(\Delta f)^2} \tag{4.8}$$

From the bispectrum the biphase can be obtained as:

$$\beta(f_m, f_n) = \frac{\Im\left(B(f_m, f_n)\right)}{\Re\left(B(f_m, f_n)\right)} \tag{4.9}$$

in which $\Re$ and $\Im$ denote the real and the imaginary parts.

4.2.3. WAVE SHAPE AND BOUND WAVE HEIGHT

From the spectrum and bispectrum, the normalized sea-swell wave shape, which represents the combination of skewness Sk_η and asymmetry As_η, can be obtained from:

$$S_\eta = \frac{\sqrt{Sk_\eta^2 + As_\eta^2}}{m_0^{3/2}} = \frac{6\left|\sum_{p=i_{b,min}}^{i_{b,max}} \sum_{m=i_{min}}^{p-i_{min}} B(f_m, f_{p-m})(\Delta f)^2\right|}{m_0^{3/2}} \tag{4.10}$$

in which $i_{b,min}$ and $i_{b,max}$ are the indices referring to the lower and upper frequency bound of the bound superharmonic frequencies.

Following Chapter 3, based on the work of Herbers et al. (1994), the total amount of bound variance associated with super harmonics can be obtained using:

$$\sum_{p=i_{b,min}}^{i_{b,max}} E_b(f_p)\Delta f = 4\frac{\left|\sum_{p=i_{b,min}}^{i_{b,max}}\sum_{m=i_{min}}^{p-i_{min}} B(f_m,f_{p-m})(\Delta f)^2\right|^2}{\sum_{p=i_{b,min}}^{i_{b,max}}\sum_{m=i_{min}}^{p-i_{min}} E(f_m)E(f_{p-m})(\Delta f)^2} \tag{4.11}$$

in which the factor 4 originates from the single sided variance densities used in this equation instead of double sided variance densities. Analogous to the wave height, the bound wave height can be obtained from the bound variance density:

$$H_b = 4\sqrt{\sum_{p=i_{b,min}}^{i_{b,max}} E_b(f_p)\Delta f} \tag{4.12}$$

in which $i_{b,min}$ and $i_{b,max}$ are indices corresponding to the the lower and upper frequency limits over which the bound wave height is computed.

4.3. SPECTRAL EVOLUTION EQUATIONS FOR TOTAL AND BOUND VARIANCE DENSITY

This Section describes how information extracted from SWAN is used to solve the evolution equation for the bound wave variance density. As SWAN does not distinguish between free and bound waves, it is referred to as the total wave evolution equation. The evolution equation for the bound wave variance density is the novel part introduced in this chapter that allows us to keep track of the evolution of the bound wave height and wave shape. For reading purposes, the equations are presented here in a 1D form, consistent with unidirectional normally incident waves propagating over an alongshore uniform profile.

4.3.1. TOTAL AND BOUND WAVE ENERGY BALANCE

The 1D evolution equation for the total variance density in stationary conditions, computed by SWAN, is:

$$\frac{dE(f,x)c_g(f,x)}{dx} = S_{nl3}(f,x) + S_{break}(f,x) \tag{4.13}$$

where $E(f,x)$ represents the variance density as a function of frequency f and cross-shore distance x, and in which c_g is the group celerity, which is computed using the linear dispersion relationship. This implicitly assumes that, in such models, all energy is freely propagating. Source terms are used to account for growth, dissipation and redistribution of energy due to nonlinear processes. S_{nl3} and S_{break} are source terms accounting for the effect of nonlinear triad wave interactions and wave breaking, respectively (discussed in more detail in Sections 4.3.2-4.3.3). Other commonly used source terms (wind, quadruplet, whitecapping and friction) are ignored in this study to simplify the analysis. Furthermore, their effects are expected to be negligible compared to S_{nl3} and S_{break} in the intermediate water depth and over the limited propagation distance investigated in this study.

In the following, the bound fraction is separated from the total energy balance. The S_{nl3} source term accounts for nonlinear triad wave interactions, which are energy transfers from two free harmonics towards a third bound harmonic. It is positive at frequencies towards which (bound) energy is transferred and negative at the frequencies this energy originates from. A detailed description of this source term is provided in Section 4.3.2. For the bound energy equation, only the positive part of S_{nl3} is considered as a source term. Furthermore a wave breaking source term $S_{b,break}$ is added to account for the dissipation of bound wave energy. Subsequently, the evolution equation for the propagation of bound variance density in steady conditions reads:

$$\frac{dE_b(f,x)c_g(f,x)}{dx} = max(0, S_{nl3}(f,x)) + S_{b,break}(f,x) \tag{4.14}$$

in which $E_b(f,x)$ is the bound variance density. For consistency with the evolution equation for the total variance (Eq. 4.13), it is also assumed here that the bound variance propagates at the free wave group celerity c_g.

The bound wave height can be obtained by integrating the bound variance density (Eq. 4.12). Normalized by the significant wave height, as was recently shown in Chapter 3, this can be used as a proxy for the normalized wave shape:

$$S_\eta = \Psi \frac{H_b}{H} \tag{4.15}$$

in which Ψ is a proportionality coefficient obtained by substitution of Equations (4.6a and 4.10-4.12) into Equation (4.15):

$$\Psi = 3\frac{\sqrt{\sum_{p=i_{b,min}}^{i_{b,max}} \sum_{m=i_{min}}^{p-i_{min}} E(f_m)E(f_{p-m})(\Delta f)^2}}{m_0} \tag{4.16}$$

The fraction on the right hand side of Equation (4.16) equals 1 (and thus $\Psi = 3$) if the sums are evaluated over the full frequency range. However, if only part of the integrals are included, for instance in our case by only including sea-swell frequencies, this fraction is smaller than 1. In shallow water, where relatively more energy is present in the infragravity frequency band and in the high-frequency tail, this fraction decreases. The formulation for Ψ in Equation (4.16) is consistent with the empirically-derived constant values (Ψ between 2.70 and 2.80) found by de Wit et al. (2020) (Chapter 3) using data collected from 3 different field sites.

4.3.2. NONLINEAR TRIAD ENERGY TRANSFERS S_{nl3}

Triad wave-wave interactions are nonlinear interactions between three wave components with frequencies f_m, f_n, and f_p satisfying: $f_p = f_m \pm f_n$. Within these interactions, a distinction can be made between sum interactions ($f_p = f_m + f_n$) and difference interactions ($f_p = f_m - f_n$). When certain near-resonant conditions are met, a nonlinear energy transfer from free components m and n towards bound component p takes place (Phillips, 1960; Hasselmann, 1962). In fully resonant conditions the same relationship is found for the wave numbers as for the frequencies: $k_p = k_m \pm k_n$. However, this condition is only satisfied in shallow water for non-dispersive waves. Nonlinear energy transfers also occur in

near-resonant conditions ($k_p = k_m \pm k_n + \Delta k$) in finite water depth (Armstrong et al., 1962; Bretherton, 1964), with their strength being inversely proportional to the wave number mismatch Δk.

Different formulations are available for the S_{nl3} source term in spectral models (Eldeberky, 1996; Becq-Girard et al., 1999; Salmon et al., 2016; Janssen et al., 2006), which are all derived from the following equation relating energy transfers due to triad interactions to the imaginary part of the bispectrum:

$$S_{nl3}(f_p) = 2\pi c_{g,p}\left[\int_0^{f_p} W_{m,p-m}\Im(B(f_m, f_{p-m}))df_m - 2\int_0^{\infty} W_{-m,p+m}\Im(B(f_m, f_p))df_m\right] \tag{4.17}$$

in which $W_{m,p-m}$ is the nonlinear interaction coefficient for two interacting components with indices m and $n = p - m$. The first term on the right hand side of Equation 4.17 account for the sum interactions whereas the second term accounts for the difference interactions.

In this section we discuss two commonly used formulations that are both implemented in SWAN, the LTA method (Eldeberky, 1996) and the SPB method (Becq et al., 1998; Becq-Girard et al., 1999). Both methods use the same nonlinear interaction coefficient derived by Madsen & Sørensen (1993), based on Boussinesq wave theory (Madsen & Sørensen, 1992):

$$W_{m,p-m} = \frac{(k_m + k_{p-m})^2[\frac{1}{2} + c_m c_{p-m}(gd)^{-1}]}{-2(k_p d)^2[\frac{2}{15} + (k_p d)^{-2} - \frac{2}{5}c_p^2(gd)^{-1}]} \tag{4.18}$$

in which g is the gravitational acceleration, c and k are the wave celerity and wave number according to linear wave theory, with the subscripts indicating the frequency for which these are calculated, and d the local water depth.

These two formulations differ in the number of nonlinear interactions that are accounted for and in the way the imaginary part of the bispectrum is estimated. More specifically, the bispectral estimate needed in Eq. (4.17) is derived from the evolution equation for the bispectrum, which itself depends on the trispectrum. Estimating the bispectrum therefore requires a closure approximation in which the trispectrum is expressed in terms of lower order spectra, hence the spectrum and bispectrum.

LTA METHOD

The Lumped Triad Approximation (LTA) is a computationally efficient method that assumes that the energy transfer to a certain frequency as a result of many interactions can be represented by the self-self interaction only. LTA further relies on the quasi-normal closure approximation (Benney & Saffman, 1966), in which the trispectrum is expressed in terms of the variance spectrum only. Based on these two assumptions, an approximation is found for the absolute value of the bispectrum, which is multiplied by a parametrized form of the biphase to get an estimate for the imaginary part of the bispectrum(Eldeberky, 1996):

$$S_{nl3,LTA}(f_p) = \alpha_{LTA} c_{g,p} c_p \left[W_{p/2,p/2}\tilde{Q}(f_{p/2}, f_{p/2}) - 2W_{p,p}\tilde{Q}(f_p, f_p)\right] sin(\beta_{\widehat{Ur}}) \tag{4.19}$$

in which α_{LTA} is a calibration coefficient, $\tilde{Q}$ consists of variance cross-products:

$$\tilde{Q}(f_{p/2}, f_{p/2}) = W_{p/2,p/2}\left[E(f_{p/2})^2 - 2E(f_p)E(f_{p/2})\right]. \tag{4.20}$$

$\beta_{\widehat{Ur}}$ is a parametrized form of the biphase based on the spectral Ursell number:

$$\beta_{\widehat{Ur}} = \frac{\pi}{2} tanh\left(\frac{Ur_{crit}}{\widehat{Ur}}\right) - \frac{\pi}{2} \tag{4.21}$$

with

$$\widehat{Ur} = \frac{gH}{8\sqrt{2}}\left(\frac{T_{m_{0,1}}}{\pi d}\right)^2. \tag{4.22}$$

This parametrization ensures a smooth transition from $\beta_{\widehat{Ur}} = 0$ (no energy transfer) for low $\widehat{Ur}$ to a maximum value of $\beta_{\widehat{Ur}} = -\pi/2$ for high $\widehat{Ur}$-numbers. Ur_{crit} is a calibration coefficient that controls how fast $\beta_{\widehat{Ur}}$ evolves, for which a wide variety of values is found in literature e.g., 0.20 by Eldeberky & Battjes (1994), 0.63 by Doering & Bowen (1995). Similarly, many variations for α_{LTA} are found in literature, (e.g., 0.05 (Van der Westhuysen, 2007), 0.1 (Holthuijsen, 1999), 0.25 (Booij et al., 1999), 0.5 (Ris, 1997) 1.0 (Eldeberky, 1996), and most recently 0.87 (Salmon et al., 2016)). Presently, in the most recent version of SWAN (version 41.31), the default values are $Ur_{crit} = 0.2$ and $\alpha_{LTA} = 0.87$.

4

SPB METHOD

An alternative approach is the SPB method (Stochastic Parametrized Boussinesq). In contrast to the LTA method, the SPB method takes all co-linear sum and difference interactions into account and relies on Holloway (1980)'s closure approximation that assumes that the trispectrum is expressed in terms of the variance spectrum and the bispectrum. The resulting expression is:

$$S_{nl3,SPB}(f_p) = 4\alpha_{SPB} c_{g,p} K \left[\int_0^{f_p} \frac{W_{m,p-m} Q(f_m, f_{p-m})}{\Delta k_{m,p-m}^2 + K^2} df_m - 2\int_0^{\infty} \frac{W_{-m,p+m} Q(f_m, f_p)}{\Delta k_{m,p}^2 + K^2} df_m \right], \tag{4.23}$$

with

$$Q(f_m, f_{p-m}) = W_{m,p-m} E(f_m) E(f_{p-m}) - W_{p,-m} E(f_p) E(f_m) - W_{p,m-p} E(f_p) E(f_{p-m}). \tag{4.24}$$

α_{SPB} is a proportionality factor which is 1 for unidirectional waves and lower then 1 for directional waves to compensate for not all interactions being co-linear. $\Delta k_{m,p-m} = k_p - k_m - k_{p-m}$ is the wave number mismatch in which the individual wave numbers are computed with the linear dispersion relationship as being freely propagating components and K is a calibration factor, with dimension 1/m.

The connection between Equations (4.17) and (4.23) relies on the fact that for the SPB method the imaginary part of the bispectrum is expressed as :

$$\Im(B_{SPB}(f_m, f_{p-m})) = 2Q(f_m, f_{p-m}) \frac{K}{\Delta k_{m,p-m}^2 + K^2}. \tag{4.25}$$

In the SPB formulation, K is commonly taken as a linear function of the spectral peak wave number k_{peak}:

$$K = a * k_{peak} + b \tag{4.26}$$

where a and b are calibration constants. Becq-Girard et al. (1999) presented a form in which $K = 0.95k_{peak,offshore} - 0.75$ based on a single laboratory calibration study (Becq, 1998). Because it is hard to define the offshore peak wave number $k_{peak,offshore}$ for field cases and to prevent negative values of K, Salmon et al. (2016) proposed to use a different expression: $K = 0.95k_{peak,local}$ in which $k_{peak,local}$ is the local peak wave number. This is presently the default setting in SWAN.

ENERGY CONSERVATION CORRECTION FOR THE SPB METHOD

The presented expression for SPB (Eq. (4.23)) is exactly as described by Becq-Girard et al. (1999) and as implemented in the default SWAN version (Salmon et al., 2016). As was mentioned by Eldeberky (1996), a triad source term function based on the Holloway (1980) closure approximation is not by definition energy (and energy flux) conservative, and can thus lead to an artificial decay or gain of energy. Although the difference between the frequency integrated positive and negative fluxes is expected to be small, over a longer distance it can lead to significant changes in energy flux. Therefore, a correction factor, as was suggested by Eldeberky (1996), is applied in this study. This factor reduces the positive $S^{+}_{nl3,SPB}$ contributions if $\int S^{+}_{nl3,SPB} df > -\int S^{-}_{nl3,SPB} df$, and reduces the negative $S^{-}_{nl3,SPB}$ contributions (in an absolute sense) if $-\int S^{-}_{nl3,SPB} df > \int S^{+}_{nl3,SPB} df$. In the following, results of the SPB method include this correction factor, even when referring to default SPB settings. The importance of including the energy conservation correction is shown in Appendix 4.A.

4.3.3. WAVE BREAKING S_{break}

Several source term formulations for the dissipation due to wave breaking are available. Here, the well-known Battjes & Janssen (1978) model is applied in which a constant breaker index γ defines the ratio of the maximum wave height over depth:

$$S_{break}(f,x) = -\frac{\alpha_{BJ} Q_b(x) \gamma^2 d(x)^2}{8\pi} \frac{m_1(x)}{m_0(x)^2} E(f,x) \tag{4.27}$$

in which α_{BJ} is a calibration constant taken equal to 1 in the following. Q_b is the fraction of breaking waves.

The amount of wave breaking for the bound wave height is assumed to be directly related to the total wave breaking source term:

$$S_{b,break}(f,x) = \alpha_{break}(f,x) S_{break}(f,x) \tag{4.28}$$

in which α_{break} defines how much of the breaking source term affects the bound harmonics, and thus indirectly also how much it affects the free harmonics. Here, it is assumed that:

$$\alpha_{break}(f,x) = E_b(f,x)/E(f,x) \tag{4.29}$$

such that there is no preference and the bound harmonics dissipate at the same rate as the free harmonics.

4.3.4. NUMERICAL IMPLEMENTATION

In this study, the spectral wave model SWAN is used to solve the energy evolution equation (Eq. (4.13)) and the source terms. Subsequently an offline post-processing routine is used

to compute the bound energy evolution equation (Eq. (4.14)). Therefore, there is only one way feedback, the SWAN model does influence the bound energy evolution equation, but not the other way around. The bound evolution equation for a given f is numerically resolved using a first order upwind numerical scheme:

$$E_b(x+\Delta x) = \frac{c_g(x)}{c_g(x+\Delta x)} E_b(x) + \frac{\Delta x}{c_g(x+\Delta x)} \left(S_{nl3}(x+\Delta x) + \frac{E_b(x)}{E(x)} S_{break}(x+\Delta x) \right) \quad (4.30)$$

with Δx as the constant grid spacing used in the SWAN computations. This post processing routine is referred to as the bound wave evolution (BWE) model.

4.4. TEST SIMULATIONS AND MODEL SET-UP

The performance of the BWE model is quantified by comparing to the SWASH model, a phase-resolving wave model (Zijlema et al., 2011). The governing equations for SWASH are the nonlinear shallow water equations including the non-hydrostatic pressure. It is proven to accurately capture short wave propagation and dispersion (Zijlema et al., 2011), wave-breaking (Smit et al., 2013), nonlinear wave dynamics (Smit et al., 2014), wave-induced currents (Rijnsdorp et al., 2017; de Wit et al., 2017; Rijnsdorp et al., 2021) and infragravity wave dynamics (Rijnsdorp et al., 2014, 2015; De Bakker et al., 2016).

The comparisons comprise computations of the spatial evolution of waves and bound waves over a 1D transect with a constantly sloping beach. For these simulations, JONSWAP wave spectra are imposed at the offshore boundary with an incoming significant wave height of 1 m and a varying peak period. As the bound wave height evolution is known to be affected by the incoming wave period and the bed slope, the model's performance is evaluated for four different peak wave periods (6, 8, 10, and 12 s) and four different bed slopes (1/20, 1/50, 1/100, and 1/200).

The performance of the SWAN simulations is quantified with the root mean squared errors (RMSE)[1] of the significant wave height H, bound wave height H_b and spectral wave period T_{m02}. For the evaluation of the S_{nl3} source term performance, the RMSEs are computed for the region between the offshore boundary and the mean breakpoint location, defined as the point where the wave height reaches its maximum, to exclude the region where $S_{break,b}$ significantly affects the bound wave height prediction. This region is in the remainder of this Chapter referred to as the shoaling zone, whereas the region beyond the mean breakpoint is referred to as the surf zone.

4.4.1. SWASH MODEL

A horizontal computational grid resolution Δx of 1 m is used to ensure enough grid points per wave length. 3 vertical sigma layers are used to ensure the accuracy of the models dispersive properties. The offshore boundary is located deep enough to ensure linearity at the wave maker boundary. The bound super-harmonics are presently not included

[1]

$$RMSE_\chi = \sqrt{\langle (\chi_{SWASH} - \chi_{SWAN})^2 \rangle} \quad (4.31)$$

in which χ is the parameter for which the RMSE is computed, $\langle ... \rangle$ denotes averaging over the relevant grid points.

at the offshore boundary in SWASH. Nevertheless, Fiedler et al. (2019) recently showed that ignoring the bound super-harmonics at the wave maker boundary, provided that it is deep enough, does not significantly influence the nearshore sea-swell third order statistics, such as bound wave energy, skewness and asymmetry. Eventually this results in a boundary depth of 20 m for the cases with T is 8, 10, and 12 s and 10 m for cases with T is 6 s. The latter is done to prevent high kd-numbers at the boundary, for which SWASH is known to be less accurate with a low number of layers (Zijlema et al., 2011). The simulations are performed with the Hydrostatic Front Approximation breaking routine in order to improve the wave breaking dissipation in case of a coarse vertical discretization (Smit et al., 2013). Simulations are performed for 75 min including 15 min of spin-up time in order to have 60 min of surface elevation output with a sampling frequency of 4 Hz that is used to generate statistically reliable estimates for the spectrum and bispectrum. The output timeseries are divided in 71 semi-overlapping blocks of each 100 s to generate ensemble averaged spectra and bispectra with a frequency resolution of 0.01 Hz and 142 degrees of freedom. These spectra and bispectra are subsequently used to obtain the bound superharmonic wave height using Equations (4.12-4.11) with $f_{i_{b,min}} = 1.5 f_{peak}$ and $f_{i_{b,max}} = 2.5 f_{peak}$.

4.4.2. SWAN MODEL

A horizontal grid resolution Δx is used of 1 m for 1/20 slope, 2.5 m for 1/50 slope, 5 m for 1/100 slope, and 10 m for 1/200 slope, such that the depth difference between subsequent grid cells is similar for all simulations. The spectrum is discretized using 71 frequencies between 0.01 and 0.5 Hz that are logarithmically distributed. Because SWAN solves for the frequency directional spectra, 45 directional bins of width $\Delta\theta = 4°$, varying between -90° and 90°, are used. Quasi unidirectionality is achieved by applying a cos^M directional distribution with $M = 300$ to the input spectrum. In order to compare simulations with exactly the same offshore spectrum, the SWASH spectrum at $x = x_{boundary}$ is imposed at the boundary for the SWAN simulations. Breaker parameter γ is optimized per simulation such that the decay of H from the SWAN simulations closely resembles the decay of H in SWASH. This results in γ ranging between 0.52 and 0.81 in which γ varies with the bed slope and wave period. Surface elevation spectra and S_{nl3} source term output are generated at all computational points and used to compute the bound wave energy spectrum and wave height using Equations (4.12) and (4.14) with $f_{i_{min}} = 1.5 f_{peak}$ and $f_{i_{max}} = 2.5 f_{peak}$.

Although S_{nl3} calibration studies have been performed before, their performance was commonly evaluated using error metrics for bulk wave parameters like significant wave height H and spectral wave period T_{m02}, instead of directly evaluating the bound wave height H_b as will be done in the following. Furthermore, the SPB-method has only been calibrated for laboratory scale experiments (Becq, 1998; Salmon et al., 2016), limiting the validity of the calibration for the dimensional parameter K. As there is no physical reason to add a dimensional number b in the parameterization of K (Eq. (4.26)), it is here chosen to follow the approach proposed by Salmon et al. (2016) to only vary a, such that K is a function of the local peak wave number only. The variations of the S_{nl3} calibration parameters considered in this study (α_{LTA} and Ur_{crit} for LTA and a and b to compute K for SPB) are given in Table 4.1. The range of values used is such that values presented in

previous calibration studies are covered resulting in a total of 182 SWAN simulations using the LTA source term and 46 using the SPB source term (see Table 4.1).

Table 4.1: Variations in conditions and calibration values applied for the SWAN calibration simulations for the S_{nl3} source term formulations using the LTA and SPB methods. Here default refers to the default parameter values in SWAN version 41.31.

slope	1/20, 1/50, 1/100, 1/200
T_{peak}	6, 8, 10, 12 s
α_{LTA}	0.1-1.0 (default = 0.87)
Ur_{crit}	0.0-1.0 (default = 0.2)
a	0.01-4.0 (default = 0.95)
b	0 (default = 0.0)

4.5. RESULTS

The evolution of the significant sea-swell wave height is accurately predicted both using default LTA and SPB triads (see Figure 4.1). Up to the break point, the RMSE$_H$ is at maximum 0.03 m for all SWAN simulations regardless whether LTA or SPB triads are used. Because of this accurate evolution of H, mismatches in the evolution of H_b in the following are assumed to be associated with the used triad formulations rather than with a mismatch of the evolution of the primary energy.

4.5.1. BOUND WAVE HEIGHT EVOLUTION

DEFAULT S_{nl3} SETTINGS

The evolution of H_b, predicted by SWASH and SWAN using both LTA and SPB triads with default calibration coefficients, is visualized in Figure 4.2 for the entire set of conditions (see overview in Table 4.1). Note that depth is represented on the horizontal axis in order to show simulations with a different slope in the same figure. The evolution of H_b using SPB triads (red lines in Fig. 4.2) closely resembles that of reference model SWASH (black lines), resulting in an average RMSE$_{H_b}$ of 0.041 m. With LTA triads (blue lines in Fig. 4.2), on the other hand, H_b is initially under predicted in deeper water, after which it overshoots and subsequently leads to a substantial over prediction. This is confirmed by a substantially higher RMSE$_{H_b}$ of 0.11 m.

A remarkable difference between the SWAN simulations and the SWASH reference simulations is the slope dependence of the predicted bound wave height evolution. For SWASH, no clear distinction is observed between the simulations with a different slope (black lines in Fig. 4.2 overlap). For the SWAN simulations with both LTA as well as SPB triads, a faster growth of H_b is observed for mild slopes (thick lines) than for the steeper slopes (thin lines), indicating that the effect of bottom slope is not properly included in the triad source terms.

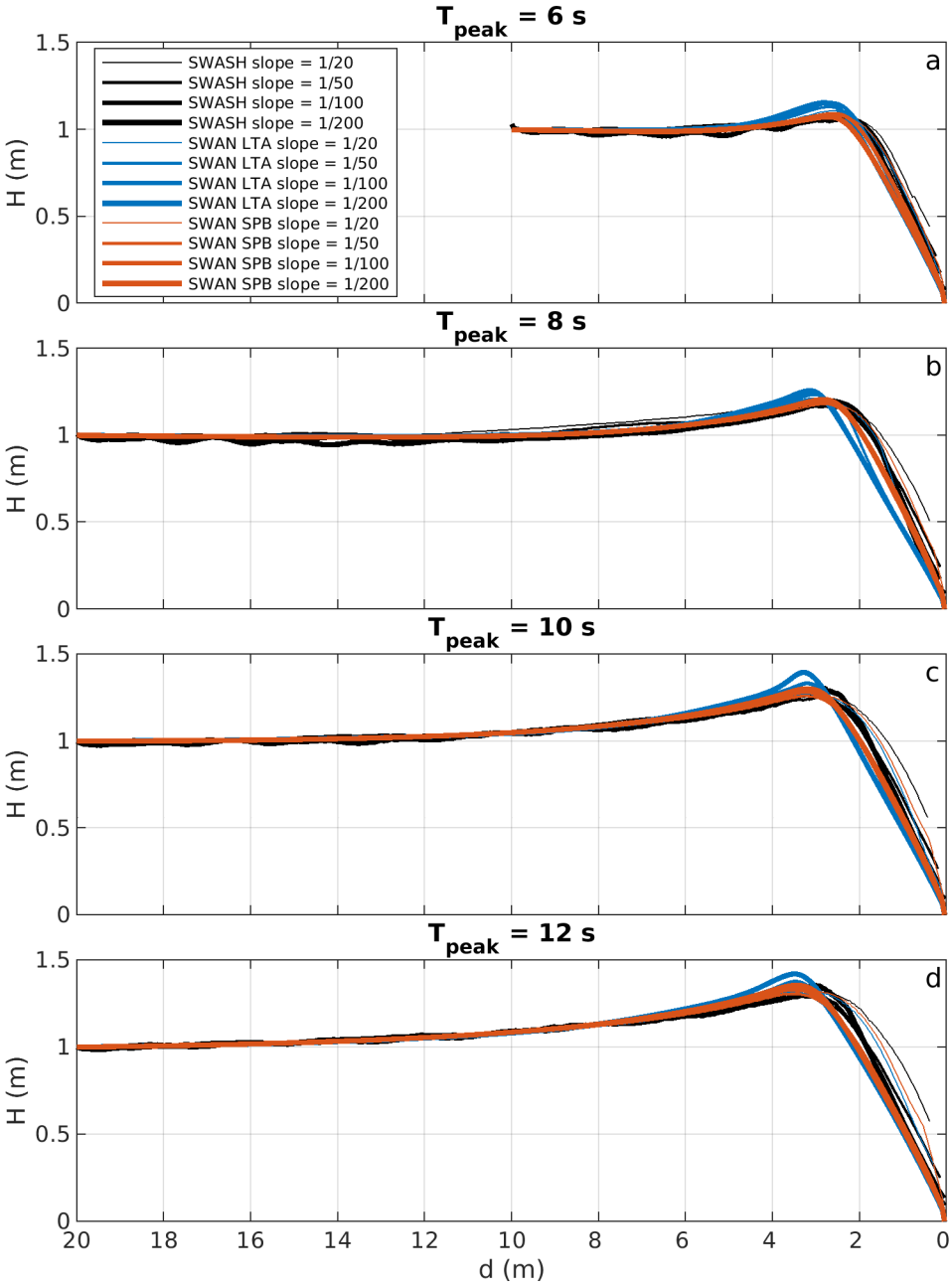

Figure 4.1: Evolution of H using SWASH (black lines), SWAN with default LTA (blue lines) and SWAN with default SPB (red lines) where different bed slopes are shown with different line widths. Different panels show the evolution of H for $T_{peak} = 6s$ (a), $T_{peak} = 8s$ (b), $T_{peak} = 10s$ (c), $T_{peak} = 12s$ (d).

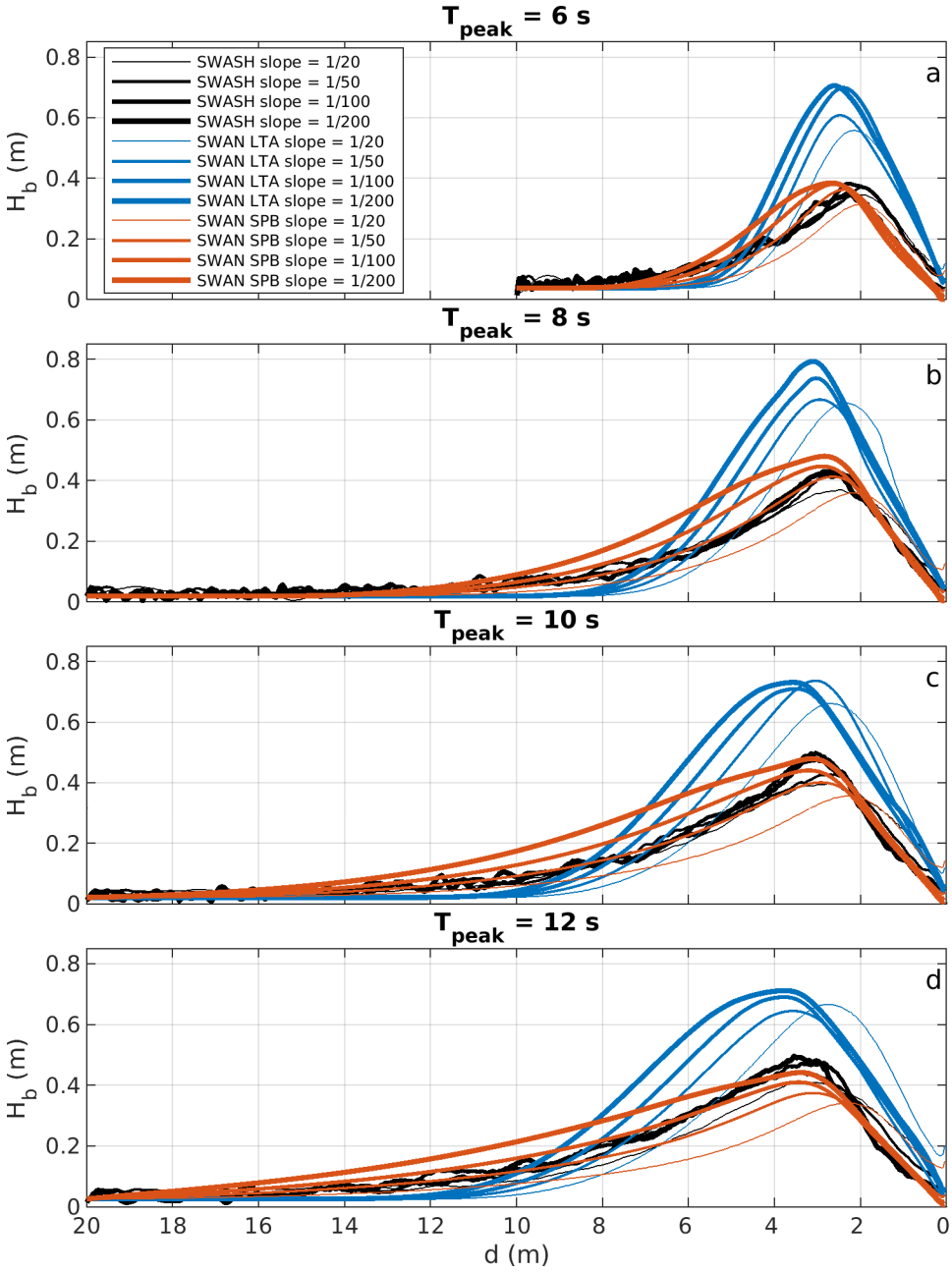

Figure 4.2: Evolution of H_b using SWASH (black lines), SWAN with default LTA (blue lines) and SWAN with default SPB (red lines) where different bed slopes are shown with different line widths. Different panels show the evolution of H for $T_{peak} = 6s$ (a), $T_{peak} = 8s$ (b), $T_{peak} = 10s$ (c), $T_{peak} = 12s$ (d).

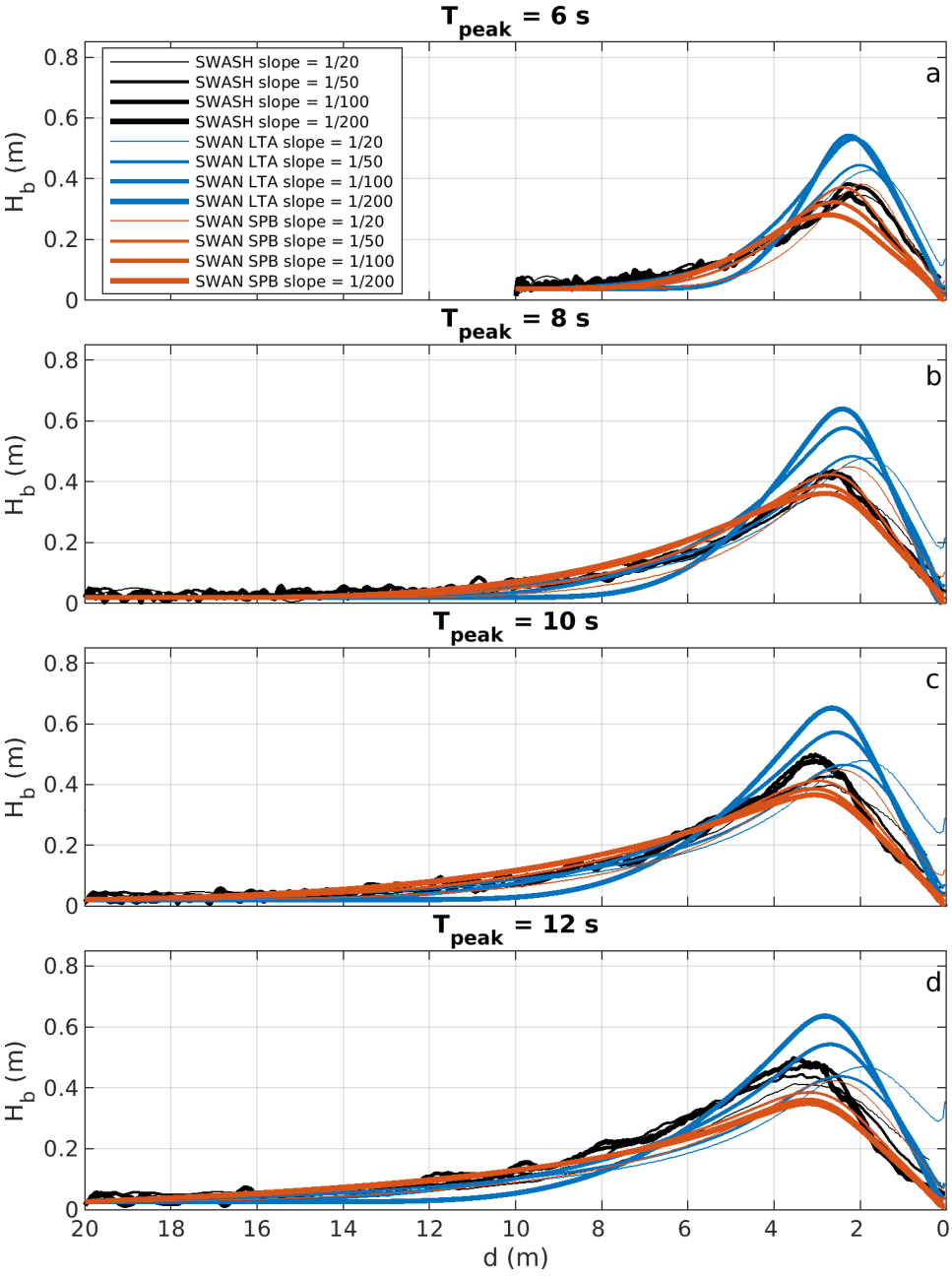

Figure 4.3: Evolution of H_b using SWASH (black lines), SWAN with optimized LTA (blue lines) and SWAN with optimized SPB (red lines) where different bed slopes are shown with different line widths. Different panels show the evolution of H for $T_{peak} = 6s$ (a), $T_{peak} = 8s$ (b), $T_{peak} = 10s$ (c), $T_{peak} = 12s$ (d).

OPTIMIZED LTA TRIADS

The LTA calibration parameters α_{LTA} and Ur_{crit} are first determined for each reference simulation (i.e. combination of peak period and bed slope) as the parameter values that minimize the shoaling zone RMSE$_{H_b}$ for this specific simulation (Fig. 4.4a). Notably, the optimal Ur_{crit} is low for all conditions, and even zero for 9 out of 16 conditions (see Fig. 4.4b). This means that the parametrized biphase leading to the best results is independent of the local Ursell number and equals $-\pi/2$ (Eq. (4.21)), corresponding to a fully imaginary bispectrum. Since the nonlinear energy transfer is proportional to the imaginary part of the bispectrum (see also $sin(\beta_{\hat{Ur}})$-dependence in Eq. (4.19)), this maximizes the energy transfers. This in turn explains the low values of the proportionality coefficient α_{LTA} (Fig. 4.4c) needed to compensate for the overestimation of the imaginary part of the bispectrum. In essence, this means that the uncertainty of Ursell-based biphase parametrization in the form presented in Equation (4.21) is so high that it is better to use a spatially constant value. As the optimal values are more sensitive to changes in slope than in period, only the slope-dependent optimized values for α_{LTA} and Ur_{crit} are retained (see Table 4.2). This leads to an improved match with the SWASH results compared to using the default values (compare blue lines in Figs 4.2 and 4.3). This improvement reduces the average RMSE$_{H_b}$ from 0.109 m to 0.031 m (see Table 4.3) .

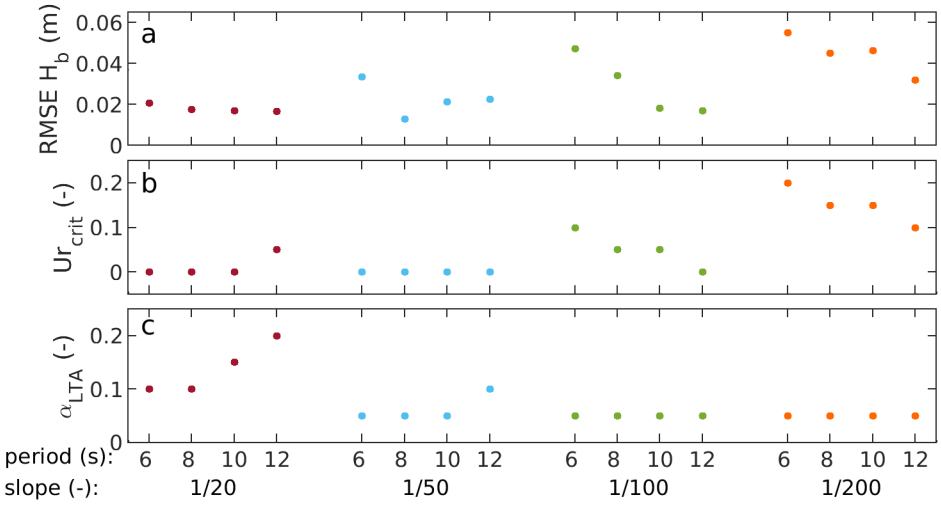

Figure 4.4: Overview of the errors and tuning parameters for SWAN LTA simulations with optimized settings for the different slopes and conditions. Panel a shows RMSE$_{H_b}$ for the simulation with the lowest RMSE, panels b and c show the corresponding optimal values for Ur_{crit} and α_{LTA}.

OPTIMIZED SPB TRIADS

To optimize the SPB triads, the shoaling zone RMSE$_{H_b}$ is calculated for all simulations with varying a-values (see Eq. (4.26)). As was found for the LTA optimization the error curves are similar for simulations with the same slope but different period (see Fig. 4.5). Therefore the slope-dependent optimal a-values are obtained from the wave period-averaged

error curves (black dashed lines in Fig. 4.5). Whereas for the simulations with a slope of 1/20 a clear single minimum is observed at $a = 0.45$, for the other slopes two local minima are observed in the error curves that move further apart for increasingly milder slopes (see Figure 4.5 and Table 4.2). As the global minimum in RMSE$_{H_b}$ is obtained for the larger a-values these will be used in the following. The significance of the secondary minimum will be discussed in Section 4.6.1. By applying the slope-dependant, optimized a-values, the prediction of H_b in the shoaling zone is improved (compare Figs. 4.2 and 4.3) with a reduction of average $RMSE_{H_b}$ from 0.041 m to 0.024 m compared with the default values.

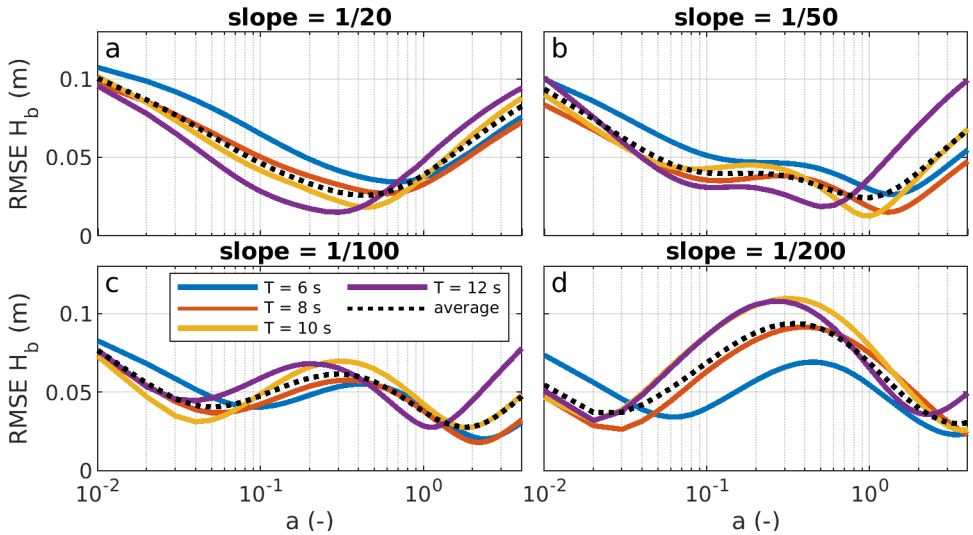

Figure 4.5: RMSE$_{H_b}$ for simulations over a constant bed slope of 1/20 (panel a), 1/50 (panel b), 1/100 (panel c), 1/200 (panel d) as a function of SPB tuning parameter a. Different colors indicate simulations with different incoming peak wave periods, the black dashed line indicates the average over the four simulations with different period.

Table 4.2: Slope-dependant calibration parameters for LTA and SPB triads (optimized based on RMSE$_{H_b}$-values in the shoaling zone). Note that for the SPB method the a-values corresponding to both local minima in RMSE$_{H_b}$ are presented for the slopes ≤ 1/50. For these cases, the a-values corresponding to the global minima are indicated by an asterisk.

	LTA triads	SPB triads
slope = 1/20	$\alpha_{LTA} = 0.10$, $Ur_{crit} = 0.0$	$a = 0.45$
slope = 1/50	$\alpha_{LTA} = 0.05$, $Ur_{crit} = 0.0$	$a = 0.12$ and $a = 0.90^*$
slope = 1/100	$\alpha_{LTA} = 0.05$, $Ur_{crit} = 0.05$	$a = 0.05$ and $a = 1.7^*$
slope = 1/200	$\alpha_{LTA} = 0.05$, $Ur_{crit} = 0.15$	$a = 0.03$ and $a = 3.4^*$

Table 4.3: RMSE$_H$, RMSE$_{H_b}$ and RMSE$_{T_{m02}}$ in the shoaling zone for LTA and SPB with default and optimized calibration parameters per slope (see Table 4.2 for their values).

	RMSE$_H$ (m)	RMSE$_{H_b}$ (m)	RMSE$_{T_{m02}}$ (s)
LTA default	0.025	0.109	0.30
LTA optimized	0.016	0.031	0.32
SPB default	0.016	0.041	0.25
SPB optimized	0.016	0.024	0.22

4.5.2. WAVE SHAPE PREDICTION

The wave shape is directly obtained from SWASH with Equation (4.10) and estimated from the SWAN simulations with Equation (4.15) in two ways. One with Ψ according to Equation (4.16) and one with $\Psi = 2.75$, following the empirical relationship of de Wit et al. (2020). As an example the evolution of S_η is presented for the case with $T_{peak} = 8$ s and a slope of 1/50 as this is the case with the best prediction of H_b for both LTA and SPB (see Fig. 4.6a). Using a constant Ψ of 2.75 the development of S_η is accurately predicted by simulations with both triad formulations in the shoaling zone (see dashed lines in Fig. 4.6b). In contrast, within the surf zone ($d < 3$ m) S_η is clearly over predicted by both LTA and SPB formulations, even though using SPB triads results in a close match with H (not shown here) and H_b from SWASH in the surf zone (Fig. 4.6a). Accounting for the spectral shape through Eq. (4.16) results in an improved match with the SWASH results (compare dashed and solid lines in Fig. 4.6b). Remaining errors are related to differences in the spectral shapes between the SWAN and SWASH predictions discussed in Section 4.6.2 and to the over prediction of H_b in case of LTA triads (Fig.4.6a).

Next the SWAN-predicted wave shape S_η using the optimized slope dependent parameters (see Table 4.2) and the spectral shape dependent value of Ψ (Eq. 4.16) are compared with the SWASH benchmark for all slopes and wave periods. Using LTA, the wave shape in the shoaling zone is under predicted for low S_η but over predicted for high S_η (Fig. 4.7a). This results in a RMSE$_{S_\eta}$ of 0.08 and a R^2 of 0.91. Improved results are obtained when SPB triads are used (Fig. 4.7b) with a reduction in RMSE$_{S_\eta}$ to 0.05 and a R^2 of 0.94. In the surf zone, both LTA and SPB triads over predict S_η (Fig. 4.7c-d) with a concurrent increase in RMSE$_{S_\eta}$ to 0.46 and 0.21 for LTA and SPB, respectively. This over prediction is partly caused by the aforementioned spectral differences between SWAN and SWASH and their impact on Ψ. The larger mismatch for the LTA results are related to the persistent over prediction of H_b within the surfzone (see Fig.4.3).

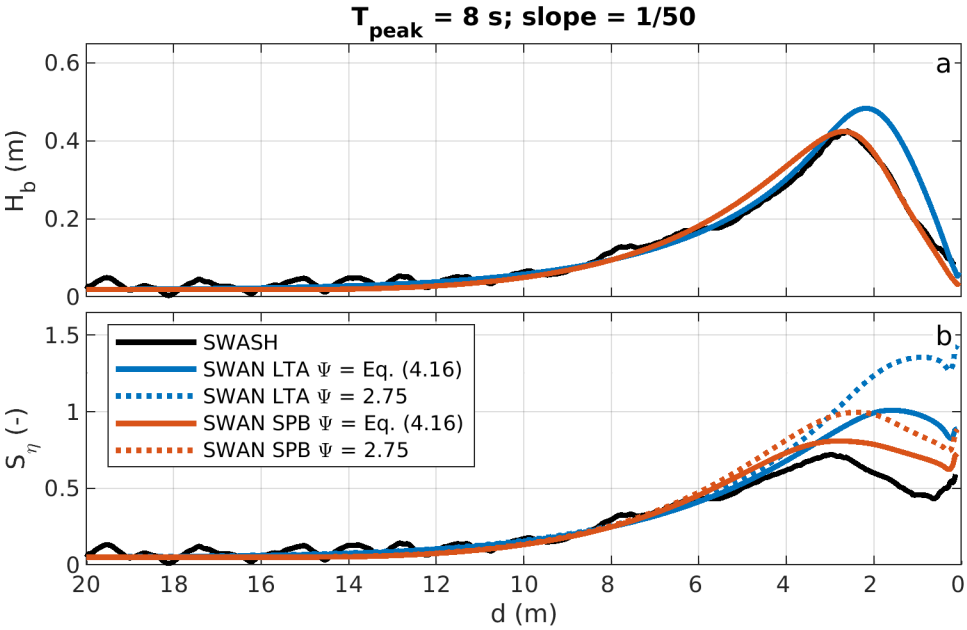

Figure 4.6: Spatial evolution of the bound wave height (panel a) and normalized wave shape (panel b) using reference model SWASH (black lines), SWAN with LTA triads with optimized settings (blue lines) and SWAN with SPB triads with optimized settings (red lines)

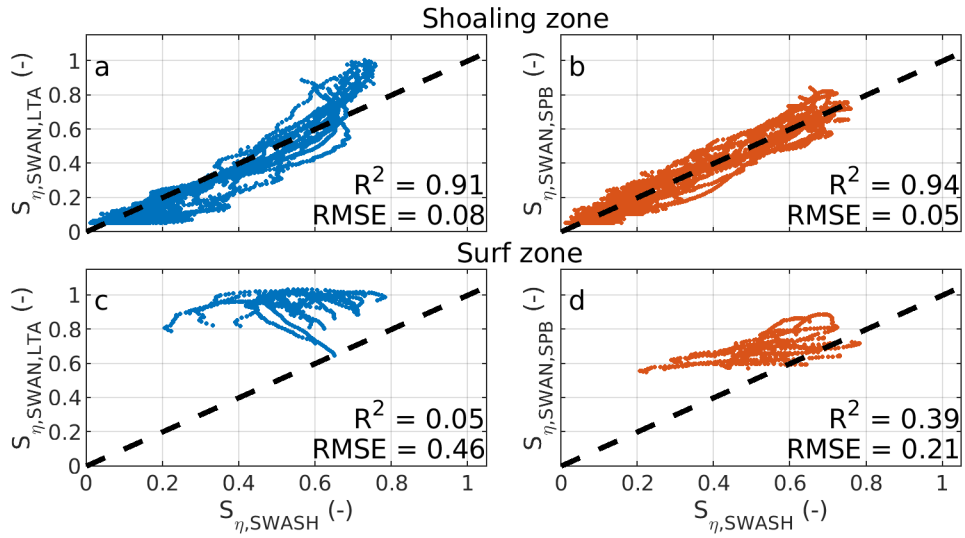

Figure 4.7: SWAN predicted normalized wave shape using LTA (a) and SPB (b) triads in the shoaling zone and LTA (c) and SPB (d) triads in the surf zone as a function of normalized wave shape from reference model SWASH.

4.6. DISCUSSION

4.6.1. UNCERTAINTIES ASSOCIATED WITH THE S_{nl3} TRIAD FORMULATIONS

PARAMETRIZATION OF β IN LTA

In Section 4.5.1, it is shown that by using the optimal calibration settings for SWAN simulations with LTA triads (see Table 4.2) the biphase estimates (Eq. (4.21)), are almost independent on Ursell, given the very low values of Ur_{crit}. For SWAN simulations with a steeper slope Ur_{crit} is in fact zero (see Table 4.2) corresponding to an Ursell-independent biphase of $-\frac{\pi}{2}$. To further investigate this dependence, the behaviour of the biphase is examined using the SWASH simulations. A reliable estimate of the biphase at (f_{peak}, f_{peak}) is obtained from the SWASH bispectra by applying an energy-weighted average of all biphases (Eq. (4.9)) that satisfy $0.5f_{peak} < f_m, f_n < 1.5f_{peak}$. The biphase for all SWASH simulations is visualized in Figure 4.8. The large scatter in biphase for $Ur < 0.05$ is explained by the fact that for linear waves the biphase is expected to be randomly distributed between $-\pi$ and π (because the real and imaginary part of the bispectrum are both very close to 0). In contrast to the SWAN simulations, for higher Ur-numbers, the SWASH derived biphase estimates do show a clear dependence on the Ursell number.

Furthermore, consistent with previous research (Norheim et al., 1998; Dong et al., 2014; Rocha et al., 2017; Chen et al., 2018), a clear bed slope dependence is observed for the biphase from the SWASH simulations, with an increase in absolute biphase values for simulations with steeper slopes (Fig. 4.8). The Ursell-based biphase parameterizations of Eldeberky & Battjes (1994) and Doering & Bowen (1995) are independent of the bed slope, which partly explains the wide range of values for Ur_{crit} found in literature. Note also that the period dependence of the biphase is not accurately represented by the local Ursell number (see the vertical spread in lines of the same color in Fig. 4.8) consistent with the findings in Section 2.3.3, thereby adding to the scatter.

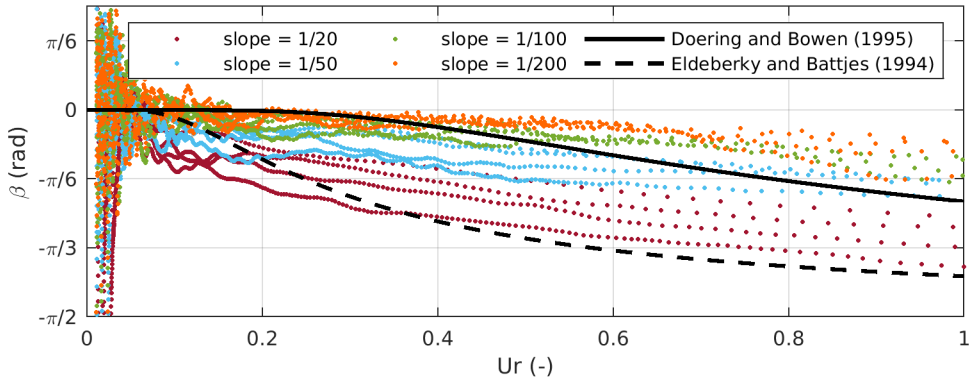

Figure 4.8: Estimated biphase $\beta(f_{peak}, f_{peak})$ from SWASH simulations (each color indicate the results for all peak wave periods on a given bed slope) and parametrized biphase using Equation 4.21 with $Ur_{crit} = 0.68$ (solid black line) and $Ur_{crit} = 0.20$ (dashed black line) as a function of the Ursell number.

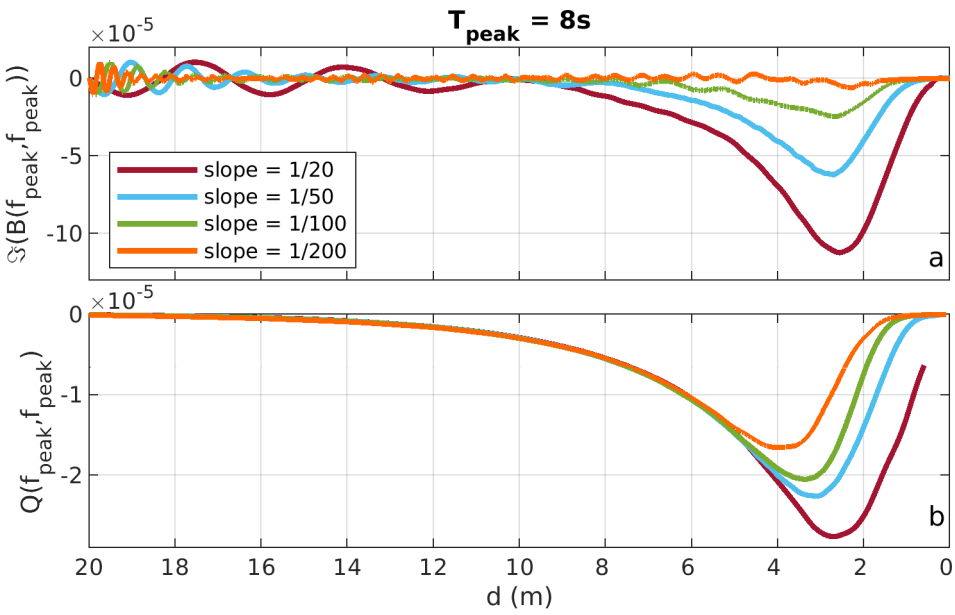

Figure 4.9: Evolution of $\Im(B(f_{peak}, f_{peak}))$ and $Q(f_{peak}, f_{peak})$ for the SWASH simulation with $T_{peak} = 8s$ and varying bed slopes.

4

PARAMETRIZATION OF K IN SPB

K is the only tunable parameter in the SPB method controlling the strength of the nonlinear triad interactions (Eq. (4.23)) and is related to a through Equation (4.26). Using default SPB parameter settings erroneous slope dependent results for the evolution of H_b are obtained (see Fig. 4.2). Consequently the optimized a-values display a strong slope dependence to minimize the errors (see Table 4.2).

To further analyse this slope dependence, the behavior of the SWASH-derived $\Im(B)$ (which is reflective of S_{nl3}) is examined for varying beach slopes. To get a more reliable estimate of the bispectrum, the ensemble-averaged bispectrum is obtained from 50 similar SWASH simulations with different random phases imposed at the offshore boundary. These results show that the spatial evolution of $\Im(B(f_{peak}, f_{peak}))$ for simulations with a peak period of 8 s is much stronger for steeper than for milder slopes (see Figure 4.9a).

In the SPB formulation $\Im(B(f_{peak}, f_{peak}))$ is proportional to $Q(f_{peak}, f_{peak})$ with a proportionality factor that depends on K and $\Delta k_{peak,peak}$ (Eq. (4.25)) only. Given the fact that the peak wave period is the same in these four SWASH simulations, the $\Delta k_{peak,peak}$ for a given depth does not change and hence only the dependence on K remains.

It is then evident from the depth-dependent distribution of $Q(f_{peak}, f_{peak})$ (shown in Fig. 4.9b) that a slope-independent proportionality factor K cannot properly predict the corresponding $\Im(B(f_{peak}, f_{peak}))$ (shown in Fig. 4.9a) as this factor should be much smaller for milder slopes than for steeper slopes. This implies that K cannot be proportional to the local peak wave number only, as expressed in Equation (4.26).

Other methods to parameterize K were explored in this study (not shown), but did

not improve the predictive skill of the SPB method. Amongst those methods are parameterizing K as a small constant value (suggested by Eldeberky, 1996), as a function of the offshore peak wave number (suggested by Becq et al., 1998; Becq-Girard et al., 1999) or as a function of the minimum of the three interacting wave numbers (suggested by Janssen et al., 2006). In none of these parameterizations the slope effect is accounted for and hence they are not expected to remove this dependency.

Furthermore, two slope dependent local minima are observed for the milder slopes (see Fig. 4.5). Taking the simulation with T_{peak} = 8 s and slope = 1/200 as an example, Figure 4.10a shows the prediction of H_b for both local minima. It shows that depending on the choice of a, H_b is either overestimated between d = 10 m and d = 4 m and underestimated between d = 4 to d = 3 m or the other way around. This suggests that even for a given slope a spatially varying value of a and thus K should be used that is not linearly proportional to the local k_{peak}.

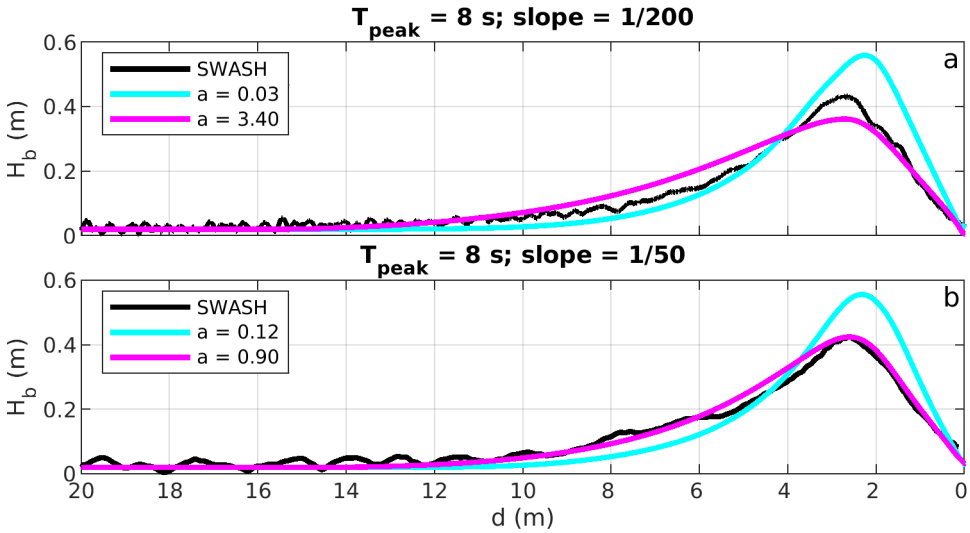

Figure 4.10: Spatial evolution of the bound wave height for T_{peak} = 8 s and a slope of 1/200 (panel a) and a slope of 1/50 (panel b) for reference model SWASH (black line) and SWAN with SPB triads for the a-values corresponding to the two local error minima listed in Table 4.2 (coloured lines)

4.6.2. BOUND WAVE PREDICTION IN THE SURF ZONE

Whereas S_η is accurately predicted in the shoaling zone using SPB triads, an over prediction is found in the surf zone, even for the cases where the evolution of H and H_b is accurately predicted in the surf zone (see for example Fig. 4.6 with T= 8 s and a slope of 1/50). This indicates that the over prediction is caused by an over prediction of Ψ, which itself depends on the prediction of the spectral shape. This is confirmed by calculating Ψ for the SWASH and the SWAN spectra for this case, showing that between d = 4 and d = 1 m, Ψ from SWAN is on average 23% higher with a maximum over estimation of 44%. The same simulation with LTA triads also considerably overestimates Ψ (average 17% and maximum 24%).

The mismatch in Ψ using the SPB triads is examined next by looking in more detail at the spectra in the surf zone for this case (see Fig. 4.11). It is seen that before breaking ($d = 4$ m), there is a good agreement between the SWASH and SWAN spectral shape as the secondary super harmonics and the high frequency tail are properly resolved (compare magenta and black lines). When the water depth decreases the SWAN spectra maintain their initial shape while the total energy reduces as a result of dissipation due to breaking. In contrast, the SWASH spectrum gradually transforms into a saturated spectrum towards shallower water. So even though the bulk energy transfer and decay due to triads and breaking is properly captured by SPB (see Fig. 4.10b), the distribution over the frequencies is not. As Ψ is based on the spectral shape (see Eq. (4.16)), this leads to errors in the estimated wave shape (Figs. 4.6 and 4.7).

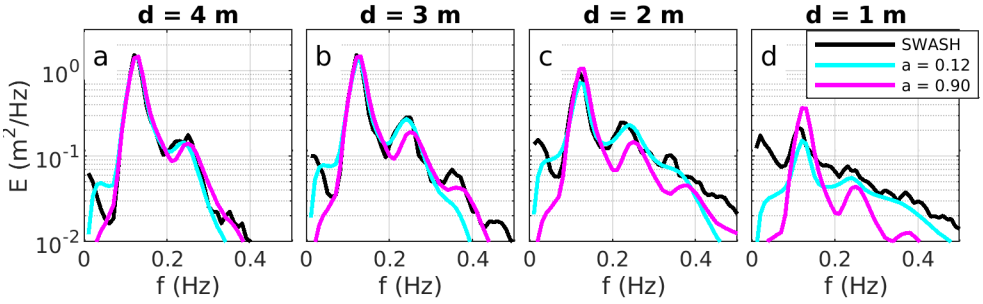

Figure 4.11: Variance density spectra for the simulation with T_{peak} = 8 s and slope is 1/50 at depths of 4, 3, 2, 1 m. Black lines represent the SWASH simulations, whereas the blue and red lines represent SWAN using SPB triads with a-values of 0.12 and 0.90, respectively.

Interestingly, the spectra predicted by SWAN using the a-value corresponding to the secondary local minimum in RMSE_{H_b} (see Table 4.3), do become more saturated with decreasing depth (compare blue and black lines in Fig. 4.11). From Equation (4.13) it can be seen that in absence of breaking the spatial flux gradient and the triad source term should be equal. Both the SWASH and SWAN simulations indicate that the influence of breaking is negligible at the surfzone edge at 4 m water depth. Therefore, the differences in the spectral evolution for the two a-values can be understood by comparing the SWAN triad source terms with the SWASH-inferred spatial gradient in flux dEc_g/dx (see Fig. 4.12). In case of the larger a-value the source term is relatively narrow with two distinct peaks moving energy from the primary spectral peak to a well defined secondary peak at twice the primary frequency. As S_{nl3} is relatively weak and dissipation by breaking in the current formulation is linearly proportional to the energy density the spectral shape is conserved throughout the surfzone. For the smaller a-value the non-linear transfer to the secondary super-harmonic spectrum is wider and significantly stronger. This results in a broadening and subsequent saturation of the high frequency part of the spectrum ($f > f_p$), more consistent with the SWASH results (Fig. 4.11). However, this is accompanied by a significant transfer of energy to the lower frequencies ($f < f_p$), erroneously adding energy at half the peak frequency (compare blue and black lines at $f = 0.063Hz$ in Fig. 4.12). This effect is exacerbated for milder slopes (not shown). Again it is likely that the mismatch within the surfzone between the SPB-SWAN and SWASH spectra can be reduced using a locally

optimized a value confirming the need for a spatially varying K value.

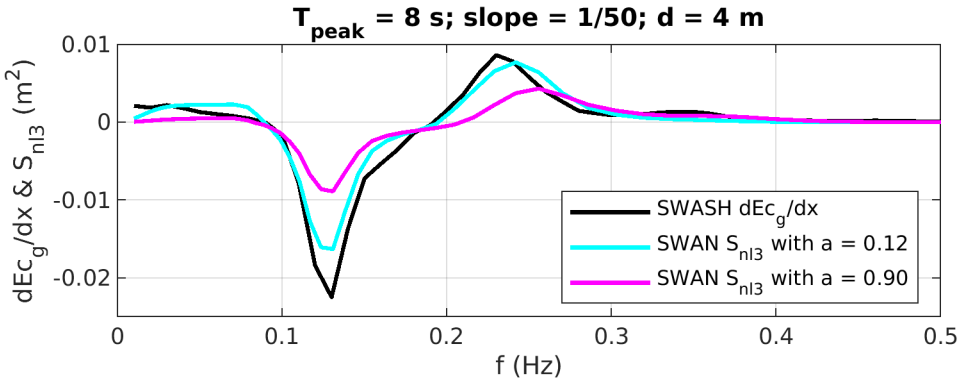

Figure 4.12: SWAN S_{nl3} source term and SWASH flux gradient (dEc_g/dx) for the simulation with T_{peak} = 8 s and slope is 1/50 at a depth of 4 m. Cyan and magenta lines represent SWAN simulations using SPB triads with a-values of 0.12 and 0.90, respectively.

4.6.3. OUTLOOK

Since K is the only tunable parameter in the SPB method in this study, mismatches in H_b and thus S_η are mainly associated with the choice for K. Currently K is optimized for the shoaling zone as this is the area where the wave shape plays a dominant role in the sediment transport (Henriquez et al., 2014; Henderson et al., 2004; Hoefel & Elgar, 2003). This approach leads to sub-optimal results for the surf zone (see Fig. 4.10). Ideally, a generic paramaterization of K performs well in both. It should be kept in mind, however, that the assumptions on the nonlinear interaction coefficients (Eq. (4.18)) and bispectral estimates also contribute to this mismatch. A way forward addressing all of these aspects is by creating ensemble averages using multiple SWASH simulations with different random phases, from which accurate stochastic estimates can be retrieved for the variance spectrum, bispectrum and even trispectrum. From these (higher order) spectra, the assumptions on the closure approximation can be validated per triad and location. These findings can subsequently be used to obtain improved expressions for K, the nonlinear interaction coefficients, and the imaginary part of the bispectrum and thereby extending the domain for which reliable predictions for the bound harmonics and the wave shape can be obtained.

4.7. CONCLUSION

In this chapter, a new method is presented that allows phase-averaged spectral wave models to predict the nonlinear wave shape. The spatial evolution of bound variance density spectra is resolved using source term functions extracted from spectral wave model SWAN that account for the influence of nonlinear energy transfers and wave breaking. By integrating the bound variance density spectra, the bound wave height is obtained. Using the proportionality factor, derived in Equations (4.15-4.16), this bound wave height can serve as a proxy for the nonlinear wave shape. As the BWE model skill to predict the bound wave

height and wave shape is predominantly determined by the accuracy of the triad source term, the performance of the LTA and SPB triad formulations is evaluated. This is done by comparing bound wave height predictions from the integrated bound evolution equation to those obtained from a detailed phase-resolving wave model (SWASH) using bispectral analysis. Although computationally more expensive, the SPB method proved to be significantly more accurate in predicting the bound wave height for all test simulations that cover a range of bed slopes and peak periods. The performance of the SPB source term can be further improved by optimizing tuning parameter K. This study already shows that different optimal K-values are found for different bed slopes, but more research is required to find a generally applicable formulation for K. Nevertheless, using the SPB method, the predicted wave shape agrees very well with the wave shape directly obtained from the reference model SWASH in the shoaling zone (R^2 = 0.96 and RMSE_S = 0.07). In the surf zone, however, an over prediction of the wave shape is observed. This arises when the proportionality factor is computed in shallow water and because there is no source term accounting for the release of bound harmonics. Overall, this chapter shows the promising capability of a wave-averaged spectral wave model to predict the nonlinear wave shape. Due to the limited additional computational effort used by the added evolution equation, this can be used in large-scale morphological models to improve the wave-shape induced sediment transport formulations.

APPENDICES

4.A. ENERGY CONSERVATION SPB

The importance of applying the energy conservation correction while using SPB triads (described in Section 4.3.2) is outlined in this appendix. By applying this correction, the evolution of H is in good agreement with reference model SWASH (compare green and black lines in Fig. 4.13). Not accounting for it, however, can lead to a significant under (or over) estimation of H in the shoaling zone where $S_{nl3,SPB}$ starts to play a prominent role (red line in Fig. 4.13). The RMSE$_H$ for default SPB settings (averaged over the 16 conditions) is decreased from 0.08 to 0.02 m by applying the correction. Furthermore, the average absolute mismatch of H at the location of maximum H is decreased from 17% to 3%.

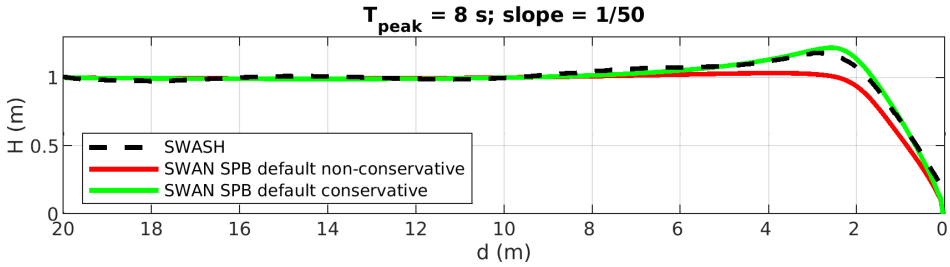

Figure 4.13: Spatial evolution of wave height for an input spectrum with incoming significant wave height of 1 m and T_{peak} = 8 s over a constantly sloping bathymetry with a slope of 1/50. Different lines indicate the outcome of the phase-resolving model SWASH (black dashed), and spectral model SWAN with default SPB settings without energy conservation correction (red), and spectral model SWAN with default SPB settings with energy conservation correction (green).

5

FIELD SCALE APPLICATION OF THE WAVE SHAPE MODEL

In this Chapter, the performance of the BWE model, presented in Chapter 4, to predict the wave shape is investigated for a field scale application. The measured wave shape is obtained from near-bed pressure measurements from nine locations in the vicinity of an ebb-tidal shoal seaward from the Ameland Inlet (Chapters 2-3). The modeled wave shape is compared to the field measurements and to two wave shape parameterizations. On the seaward slope of the ebb-tidal delta and on the shoal, the BWE model provides an accurate estimate of the wave shape. However, beyond this region, where depth is increasing after the shoal, further research is required to accurately predict the wave shape. This further research involves a better representation of the source terms for triads, breaking and the release of higher harmonics over a flat bathymetry.

5.1. INTRODUCTION

Chapter 4 showed the potential of predicting the nonlinear wave shape with the spectral wave model SWAN for synthetic cases with unidirectional waves normally approaching a constantly sloping beach. Here the potential of this modeling approach is assessed for more realistic conditions in terms of bathymetry and incoming wave field. This is done by comparing the modelled wave shape with the measurements obtained during the KG2/SEAWAD campaign at the Ameland Inlet (van Prooijen et al., 2020), that were described and analyzed in Chapters 2-3. As Chapter 4 showed that the model performance is highly dependent on the choice of the S_{nl3} source term, here again the LTA and SPB method are applied, to study the implications of the choice for a certain S_{nl3} source term on the skill to predict the wave shape. To put it in perspective, the modelled quantities are also compared to estimates obtained from two parameterizations for the nonlinear wave shape.

The main data processing steps are repeated in Section 5.2.1 for ease of reference. The SWAN model set-up and the post-processing steps applied to the numerical outputs to allow comparison with the field data are discussed in Section 5.2.2. The method to obtain the parameterized wave shape from the model output is provided in Section 5.2.3. Subsequently, the comparison between measured, modelled and parameterized wave parameters is presented in Section 5.3 after which current model limitations and future improvements are discussed in Section 5.4. This Chapter ends with conclusions in Section 5.5.

5.2. METHODS

5.2.1. DATA

In this chapter the numerical model will be compared to the data obtained at and around the main measurement transect in the vicinity of the Ameland ebb-tidal inlet (see an overview of the 9 measurement locations in Figure 2.1). Measurement locations that were not situated on the main transect are included in the analysis similarly as in Chapters 2 and 3 (see also transect representation in Figure 2.2). Hourly near-bed pressure time series are converted to near-bed pressure head time series by dividing by ρg, in which ρ is the sea-water density such that the dimension is in meters of water column. These time series are then divided in 71 semi-overlapping blocks of 100 s, which are detrended and used to compute the spectrum and bispectrum using Equations (4.4) and (4.8) with 142 degrees of freedom. Subsequently the near bed pressure derived significant wave height H^{nb}_{obs} (Eq. (4.6a)), bound wave height $H^{nb}_{b,obs}$ (Eq. (4.12)), and wave shape $S_{p,obs}$ (Eq. (4.10)) are computed. Note that for this part of the study all these wave heights are near-bed pressure head heights, indicated with the superscript *nb*.

Three selection criteria are defined to determine which cases will be run and analysed in the following. Firstly, wave conditions need to be such that there is some evolution of bound wave height, hence $H^{nb}_{b,obs} > 0.1$ m for at least one of the sensors. Secondly, only cases are considered where the depth averaged current magnitude at F5 was lower than 0.25 m/s. The methodology presented in this chapter should also be applicable in presence of currents, with the only difference that not the energy balances but the action balances need to be resolved (Bretherton & Garrett, 1968). However, the uncertainty in

the current magnitude and direction over the ebb tidal shoal is so large that accounting for it introduces significant errors in the wave number estimate and hence the related wave statistics (see Figure 2.5 and Appendix 2.A). Therefore, only cases with mild current conditions are considered. Thirdly, only the cases where the difference angle between the main transect orientation and the mean incoming wave angle is smaller than 30 degrees are considered. This is done to minimize 3D effects as SWAN will be applied to the main bathymetric transect only (see Figure 2.2). Based on these three criteria, a total of 91 cases are considered for further analysis corresponding to varying conditions (see overview in Figure 5.1).

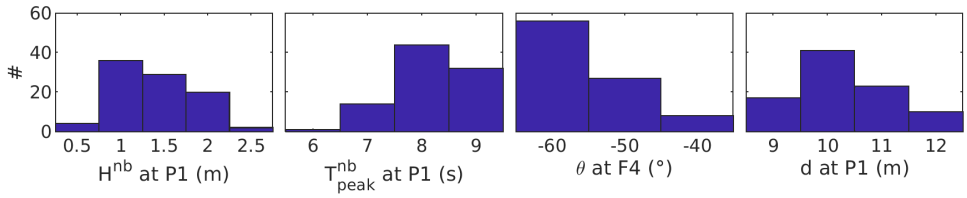

Figure 5.1: Histograms of measured near bed pressure wave height, peak period, direction and depth at the deepest available locations (P1 for wave height, period and depth, F4 for wave direction, see Figure 3.1) for the 91 cases selected for modelling.

5

5.2.2. MODEL SET-UP AND POST-PROCESSING OF THE OUTPUTS

NUMERICAL SET-UP

The SWAN model is used to simulate wave propagation over the main transect starting at P1 (Fig. 2.2). The numerical model setup is thus 1D, with a domain length of 1500 m and a grid resolution Δx of 5 m. A standard logarithmic frequency axis is used to discretize the spectrum with 71 frequency bins between 0.01 and 0.5 Hz. 45 directional bins, varying between -90° and 90°, are used ($\Delta\theta = 4°$). For every case, the actual water level is accounted for by setting the water level at the boundary to the measured water level at P1.

Model simulations are performed with three different S_{nl3} settings obtained from the slope-dependant calibration procedure performed in Chapter 4 (see Table 4.2), using the average bed slope along the main transect (1/200). These parameters are $\alpha_{LTA} = 0.05$ and $Ur_{crit} = 0.15$ for the LTA method and with $a = 0.03$ and $a = 3.4$ for the SPB method. Two calibration parameters are considered for the SPB method because they led to comparable error metrics in Chapter 4 (see the two local minima in Fig. 4.5d) but seemed to perform better in different parts of the domain (e.g., Fig. 4.10).

For the breaking source term S_{break}, the Battjes & Janssen (1978)'s model is applied (Eq. (4.27)) with $\gamma = 0.55$ based on a brief calibration procedure that showed a similar decay rate of the modelled and observed wave height in the breaking zone.

BOUNDARY CONDITIONS

SWAN predicts the evolution of the surface elevation variance and therefore needs to be forced with a surface elevation variance density spectrum. This spectrum needs to be estimated from the measured near-bed pressure signal at the most offshore sensor P1, located in a depth between 9 and 12 m depending on the tide and surge level (see Fig.

5.1).

Reconstructing the surface elevation spectrum from the pressure spectrum in such depths likely results in large inaccuracies (Guza & Thornton, 1980; Bishop & Donelan, 1987; Bonneton & Lannes, 2017), particularly in the high frequency part of the spectrum. As S_{nl3} and thus the evolution of H_b are sensitive to the initial spectral shape, an alternative approach is adopted to define the wave spectrum at the boundary. The input spectrum for SWAN, $E_{mod,P1}$, is defined as the summation of a free and a bound component:

$$E_{mod,P1}(f,\theta) = E_{mod,P1,free}(f)\Theta_{obs,F4}(f,\theta) + E_{mod,P1,bound}(f,\theta), \tag{5.1}$$

where $E_{mod,P1,free}(f)$, instead of being directly reconstructed from the measured near-bed pressure spectrum at P1, is assumed to follow a standard JONSWAP shape (enhancement factor of 3.3) with a peak frequency $f_{peak}(P1)$ and significant wave height $H(P1)$ estimated from the data at P1. $f_{peak}(P1)$ is directly obtained from the near-bed pressure spectrum and $H(P1)$ is obtained after integration over the sea-swell frequency range of the reconstructed spectrum:

$$E_{P1}(f) = E^{nb}_{P1}(f)/K^2_{att}(f) \tag{5.2}$$

in which $K_{att}(f)$ follows linear wave theory for frequencies smaller than $f_c = 0.2$ Hz, i.e. $K_{att}(f) = cosh(k(d+z))/cosh(kd)$, with for this study $d+z = 0.5$ m the sensor height from the bed, and is kept constant for larger frequencies, i.e. $K_{att}(f > f_c) = K_{att}(f_c)$. This way of accounting for the attenuation factor above the cut-off frequency was recently shown to lead to the smallest error when considering bulk parameters such as the significant wave height (Mouragues et al., 2019).

As discussed in Section 3.6.1, the 1D spectrum $E_{mod,P1,free}(f)$ is then multiplied by the normalized directional distribution $\Theta_{obs,F4}(f,\theta)$ estimated from the measurements at F4 which was the most offshore frame where velocity data was available (about 350 m away from P1, see Fig. 2.1).

The resulting 2D spectrum is finally used to calculate $E_{mod,P1,bound}(f,\theta)$ according to equilibrium second order wave theory (Hasselmann, 1962, see Eq. 3.15) which is known to be accurate in these conditions (Dean, 1970; Le Méhauté, 1976; Fenton, 1990). This estimate of the bound energy spectrum is then used as a boundary condition for the evolution equation of the bound variance density.

POST-PROCESSING OF THE MODEL OUTPUTS

The near bed pressure head spectra for total and bound variance density are obtained from the model outputs by attenuating the surface elevation spectra towards the bed using frequency-dependant attenuation factors:

$$E^{nb}_{free}(f) = (E(f) - E_b(f))K^2_{att}(f) \tag{5.3}$$

$$E^{nb}_{b}(f) = E_b(f)K^2_{att,b}(f) \tag{5.4}$$

The expression for the attenuation factor of the bound harmonics $K_{att,b}(f)$ is less straightforward than for the free components. As detailed in Appendix 5.A, the bound wave harmonics consist of three terms, that all attenuate at a different rate (Smit et al., 2017). Often

the bound wave energy is assumed to attenuate with $K_{att}(f)$ but with the bound wave number instead of the free wave number. In surf zone conditions and for longer waves (low kd-numbers) this assumption appears to be valid (see Appendix 5.A.2, Fig. 5.4). For conditions with higher kd-numbers, however, other terms with a different attenuation factor start to play a role. In these conditions, the error associated with the incorrect attenuation factor can be up to 100%. An overview of the different terms, their attenuation and the eventual bound attenuation factor is given in Appendix 5.A. For each case the following wave parameters are computed from the reconstructed near-bed pressure head spectra E^{nb}_{free} and E^{nb}_{b}: the modelled total significant wave height H^{nb}_{mod} (Eq. (4.6a)), bound wave height $H^{nb}_{b,mod}$ (Eq. (4.12)), and wave shape $S_{p,mod}$ (Eq. (4.15)).

5.2.3. PARAMETRIZATIONS

As mentioned at the beginning of this Chapter, the measured and modelled bound wave heights and wave shapes are also compared to two local parametrizations. These are calculated using the default SWAN modelled variance density spectrum (so without interference by the BWE model) and presented below.

WAVE SHAPE: RUESSINK ET AL. (2012)

The modelled wave shape is first compared to the parametrization derived by Ruessink et al. (2012) from a large number of near-bed velocity measurements:

$$S_{u,rue} = \frac{0.857}{1 + e^{\frac{-0.471 - log_{10}(Ur)}{0.297}}} \tag{5.5}$$

in which $e^{\cdots}$ is the natural exponent, $log_{10}(...)$ is the logarithm and Ur is defined as:

$$Ur = \frac{3}{8}\frac{H}{k^2_{-1,0}d^3} \tag{5.6}$$

in which $k_{-1,0}$ is the wave number based on spectral wave period $T_{m-1,0}$.

EQUILIBRIUM WAVE SHAPE: HASSELMANN (1962)

Additionally, based on the second-order finite depth equilibrium wave theory (Hasselmann, 1962), the parameterized equilibrium dimensionless wave shape is defined as:

$$S_{p,hass} = \Psi\frac{H^{nb}_{b,hass}}{H^{nb}} \tag{5.7}$$

in which $H_{b,hass}$ is the equilibrium bound wave height following Equation (3.16) and Ψ is computed according to Equation (4.16). It should be noted that the computational effort to obtain the parametrized bound wave height is approximately ten times larger than running the BWE model due to the fourfold summation in Equations (3.15-3.16).

5.3. RESULTS

The evolution of the observed, modelled and parametrized wave heights and wave shapes is first visualized for a single case on 14 September 2017 at 21:00 in Figure 5.2. For this

case, the evolution of the total wave height H_{mod}^{nb} is captured fairly well by the BWE model regardless of the triad settings (Fig. 5.2a). The evolution of the bound wave height $H_{b,mod}^{nb}$, however, is more sensitive to the triad formulation (Fig. 5.2b). Using LTA (blue line) leads to a systematic over prediction of the bound wave height. For SPB we initially see a slight under prediction using $a = 0.03$ and an over prediction using $a = 3.4$ (see red and yellow lines until $x = 950m$). The contrary is observed beyond this point where $a = 0.03$ leads to a higher bound wave height than $a = 3.4$. Independently from the triad formulations, the 3 simulations significantly overestimate the bound wave height at P4. Potential causes for this over prediction are discussed in Section 5.4.

The modelled wave shape S_p (Fig. 5.2c) depends on H_{mod}^{nb} and $H_{b,mod}^{nb}$ through Equation (4.15). Therefore, until $x = 950$ m, the wave shape is reasonably well predicted using both SPB settings while an over estimation is seen for LTA. Beyond this point, the over prediction of $H_{b,mod}^{nb}$ is also reflected in an over prediction of S_p.

The observed wave shape is further compared to the parametrizations by Ruessink et al. (2012) and Hasselmann (1962) in Figures 5.2d and 5.2e, respectively. Different triad settings lead to different spectral evolution (see also Section 4.6.2), and thus to slightly different evolution of the parametrized wave shapes. Nonetheless, the parameterizations by Ruessink et al. (2012) and Hasselmann (1962) both capture very accurately the initial growth of the nonlinear wave shape ($x \leq 950m$). These local parameterizations, however, fail to predict the wave shape at P2 where the highest nonlinearity is observed. Remarkably, the over prediction at P4 is much less when using these local parameterizations.

These trends are confirmed in Figure 5.3, which shows the modelled and parametrized wave shapes as a function of the observations for all 91 cases. Here the overestimation at P4 is also clearly visible (shown by the grey dots) and reflected by high $RMSE_S$-values (see Table 5.1). When considering all other locations (colored dots), a systematic overestimation of the modelled wave shape is seen using LTA (Fig. 5.3a), which is reflected in a $RMSE_S$ of 0.17. If $a = 0.03$ is applied for SPB, the observed and modelled wave shape match well ($RMSE_S = 0.09$) although the prediction contains significant scatter (Fig. 5.3b). On the other hand when using $a = 3.4$, the model over predicts the wave shape for $S_{p,obs} < 0.5$ whereas it under predicts for $S_{p,obs} > 0.5$ (Fig. 5.3c) resulting in a slightly higher error ($RMSE_S = 0.12$). Using the parameterization based on Hasselmann (1962), the wave shape is reasonably well predicted, although for high values of the wave shape parameter significant scatter is observed (Fig. 5.3d-f). Ruessink et al. (2012)'s parameterization under predicts the wave shape nonlinearities for cases with $S_{p,obs} > 0.5$ (Fig. 5.3g-i). Both parameterizations have a reasonably low error ($RMSE_S$ between 0.09 and 0.11), which can also be achieved with the BWE model, provided that the correct triads are applied. The predictive skill of the parameterizations is much better than the BWE model at P4 ($RMSE_S$ between 0.10 and 0.14).

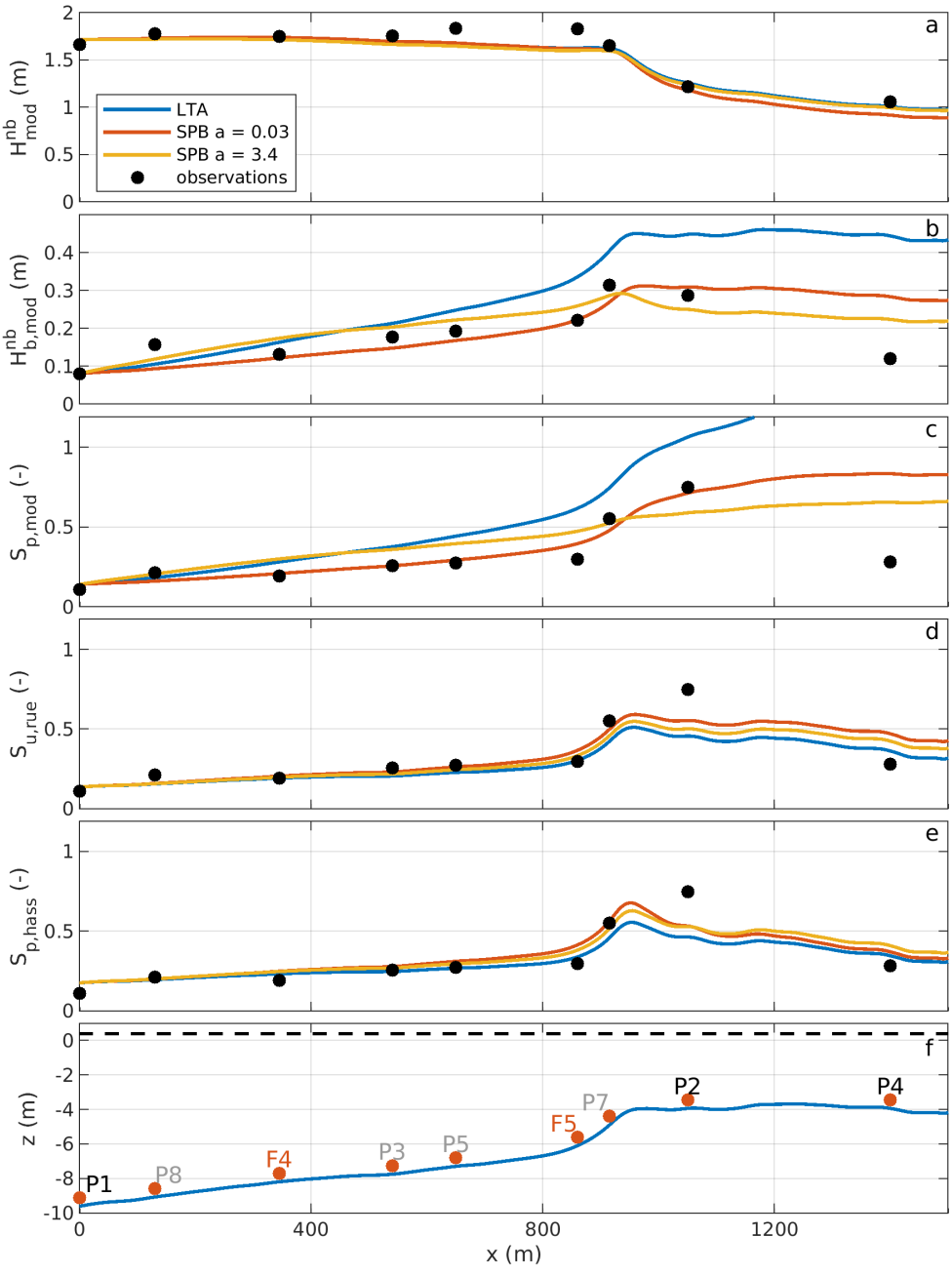

Figure 5.2: Spatial evolution of the wave height (a), bound wave height (b) and wave shape (c) from the model, the parameterized wave shape by Ruessink et al. (2012) (d) and Hasselmann (1962) (e). LTA (blue), SPB with $a = 0.03$ (red) and SPB with $a = 3.4$ (yellow) model settings are used to compute the modelled and parameterized wave parameters, black dots show the observed data points. Panel f shows the bathymetric transect (blue line), the mean water level (black dashed lines) and the position of the instruments (red dots). Black sensor names indicate pressure sensors located on the main transect, red sensor names indicate frames on the main transect and grey sensor names indicate pressure sensors located on the side transects.

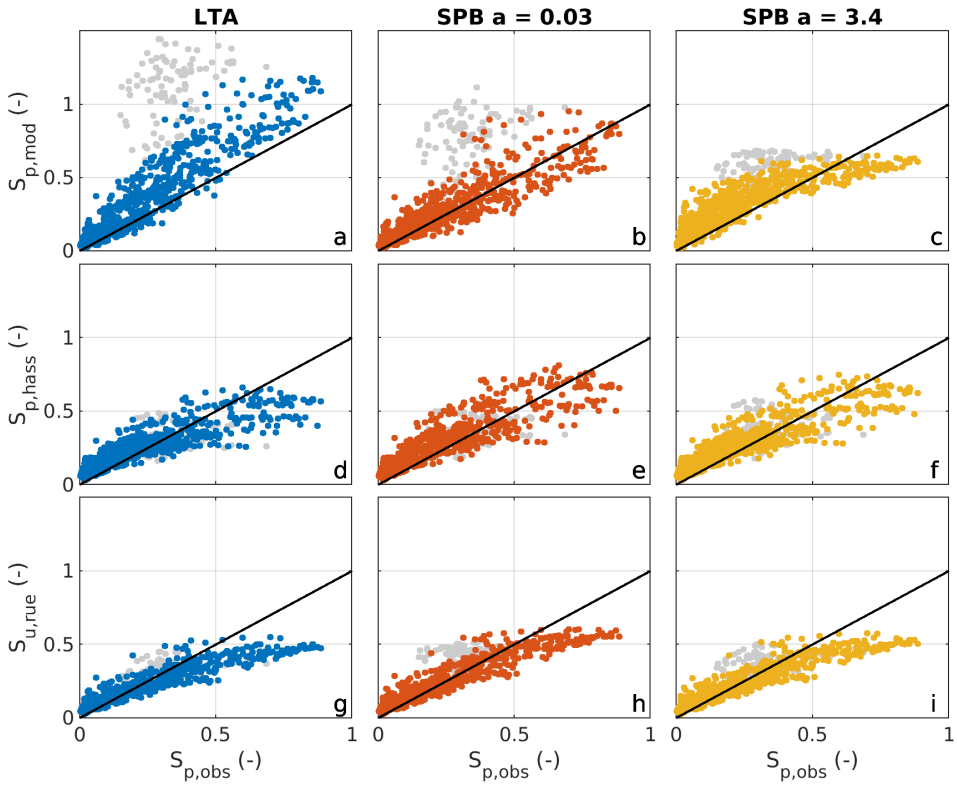

Figure 5.3: Modelled and parametrized wave shape predictions as a function of observations for the 91 cases and 9 locations. Grey dots are data points at P4, colored dots are all other locations (colors correspond to lines in Fig. 5.2). For the black lines the predictions equal the observations.

Table 5.1: RMSE of the modelled and parametrized wave shape for all 91 cases for all locations excluding P4, and for only location P4.

		All locations except P4	P4
$S_{p,mod}$	LTA	0.17	0.79
	SPB a = 0.03	0.09	0.47
	SPB a = 3.4	0.12	0.28
$S_{p,hass}$	LTA	0.11	0.12
	SPB a = 0.03	0.11	0.12
	SPB a = 3.4	0.10	0.13
$S_{u,rue}$	LTA	0.11	0.10
	SPB a = 0.03	0.09	0.14
	SPB a = 3.4	0.10	0.11

5.4. OVERESTIMATION OF THE BOUND WAVE HEIGHT OVER FLAT BATHYMETRY

A clear overestimation of the modelled bound wave height is observed at location P4, which consequentially results in an overestimation of the wave shape (see Figs. 5.2 and 5.3). Whereas the wave evolution is dominated by triads on the foreshore of the ebb-shoal ($x < 925m$) and later on by wave breaking for a confined area ($925 < x < 1050m$), identifying the dominant process between P2 and P4 is not straightforward. As discussed below, it is likely that, in this area, the bound wave height evolution is governed by a number of physical processes with similar orders of magnitude, which complicates defining the exact cause for the over prediction of the bound wave height at P4. In the following it is discussed what these processes are, how they are accounted for by the present BWE model, and how this could explain the over prediction of the bound wave height.

First of all, some depth-induced wave breaking is expected to occur between P2 and the shallowest point of the bathymetric transect (at $x = 1200m$, see Fig. 4.6f), provided that conditions are such that waves break on the foreshore of the ebb-tidal shoal. Shortcomings in the parametrization of the breaking-induced dissipation could thus contribute to the relatively poor prediction of the bound wave height at P4. Through Equation (4.28) it is assumed that the free and bound harmonics dissipate at the same rate, which proved to give reasonable dissipation rates of the bound harmonics in Chapter 4 for a constantly sloping beach. It might be that in nature, during the wave breaking process there is a preferential dissipation of the bound harmonics. If such a preferential dissipation would be applied in the BWE model, it would result in a decrease of the bound wave height at P4. Alternatively, the over prediction might be associated with the chosen breaking formulation (Battjes & Janssen, 1978), in which the dissipation is proportional to the energy distribution and is frequency independent. It has been suggested by others, however, that higher frequencies should dissipate at a faster rate, for instance using a frequency or kd dependent dissipation rate (Mase & Kirby, 1992; Kaihatu & Kirby, 1995; Chen et al., 1997; Smit et al., 2014; Salmon & Holthuijsen, 2015; Salmon et al., 2015, e.g.,). This would also lead to an increase of the breaking-induced dissipation for the bound super harmonics. In that way, even without the above mentioned preferential dissipation of the bound harmonics this would result in a stronger decrease of H_b than H. However, Figures 3.3, 3.4 and 4.6 all show a faster decay rate for the total wave height than for the bound wave height in the area where most wave breaking occurs (between P7 and P2). Hence applying a preferential dissipation of the bound harmonics or a frequency-dependent formulation for the breaking-induced dissipation could increase the agreement at P4, but would result in an under estimation of the bound wave height at P2.

The near constant depth between P2 and P4 suggests that the release of higher harmonics might also play a role in this area. Experimental (Beji & Battjes, 1993; Luth et al., 1994) and numerical studies (Beji & Battjes, 1994; Ohyama & Nadaoka, 1994) show that over a bar, bound higher harmonics are released from their primary harmonics, regardless whether breaking is occurring or not. Over the past decades there has been significant debate whether the released bound energy is further propagating as free secondary harmonics (Ohyama & Nadaoka, 1994; Masselink, 1998) or that it is transferred back to the primary harmonics by nonlinear triad interactions. The latter is in literature commonly

referred to as recurrence (Elgar et al., 1990; Chen et al., 1999; Kaihatu, 2009). Recently, a numerical study by Eldrup & Andersen (2020) showed that over flat bathymetries and mildly decreasing slopes, bound energy is transferred back towards the primary harmonics, whereas for more sudden changes in bathymetry they are released. For bound sub harmonics, this energy transfer back to the primary harmonics was found to also occurs in breaking conditions (Henderson et al., 2006; Baldock, 2012). Here the wave breaking of the primary wave energy led to a non-equilibrium condition between the primary harmonics and sub-harmonics, resulting in the energy transfer back. As the release of higher harmonics is not yet accounted for by the BWE model, this might cause the over estimation of the bound harmonics. Furthermore, as the triad models applied in this study are only validated for constantly sloping bathymetries and since only positive energy transfers towards the higher harmonics are accounted for, the recurrence process is also not included. Before being able to include the above two processes in the BWE model, further research is required to investigate which of these processes occurs, to determine the location and rate at which the bound harmonics are released and to study what parameters influence this rate.

Overall, it should be concluded that it is hard to pinpoint which (combination) of the above mentioned physical processes causes in the over prediction of the bound wave energy. Based on these two distinct locations it is impossible to identify whether it is the wave breaking source term, the triad source term, the lack of release, or a combination thereof. Therefore further research is required to increase understanding of the processes that affect the proportion of free and bound energy in the vicinity of wave breaking and at constant or increasing depth. This research can be done using phase-resolving models such as the non-hydrostatic model SWASH (as applied in Chapter 4) or the even more detailed VOF (Torres-Freyermuth et al., 2010) and CFD models (Jacobsen et al., 2012). Subsequently at every grid cell, the proportion of total, free an bound wave height can be evaluated (using the methods presented in Section 3.3.2), in order to improve understanding of the physics in this area. This can further guide the development of the BWE model.

5.5. CONCLUSIONS

This chapter demonstrates the potential of predicting the sea-swell wave shape with the spectral wave model SWAN on a field scale. By including the bound wave evolution equation the models predictive capabilities are increased such that not only second order statistics (wave height and wave period) but also third order statistics (bound wave height and wave shape) are predicted. The added value of this method over using a local parametrization for the wave shape is that the history of the waves before reaching a certain location is accounted for, making it more applicable in non-equilibrium conditions. It should still be noted that the accuracy of this model is highly dependent on the accuracy of the source terms used, in particular the one used to account for triad interactions.

Overall, the wave shape predictions from deep towards breaking conditions obtained from the BWE model are comparably accurate as the parameterizations, provided that a correct triad source term is applied. This is an important finding as this is the area where the wave-shape induced sediment transport plays the most prominent role. In the region beyond wave breaking, where the wave nonlinearity decreases again, the BWE model systematically over predicts the wave shape. In order to further increase the model accuracy

in this region, the effect of triads, breaking and the release of higher harmonics over a flat bathymetry should be better represented by the source terms. With these improvements it is anticipated that the wave shape can be accurately predicted by a phase-averaged spectral wave model. The more accurate prediction of the wave shape will contribute to improving morphological modelling exercises where wave shape induced sediment transport plays a role.

APPENDICES

5.A. NONLINEAR INTERACTION COEFFICIENTS AND ATTENUATION WITH DEPTH OF BOUND COMPONENTS

In this appendix, we first present a general formulation for the nonlinear interaction coefficient that links bound pressure head variance at an elevation z to the free surface elevation variance and highlight that it consists of three main terms that all attenuate at a different rate with depth (section 5.A.1). This information is then used in Section 5.A.2 to derive an expression for an attenuation factor for the bound variance. The attenuation factor is applied in Section 5.2.2 to translate the bound (surface elevation) variance predicted by the BWE model into a nearbed variance that can be compared with the nearbed measurements.

5.A.1. FORMULATIONS FOR THE NONLINEAR INTERACTION COEFFICIENT

In literature, a number of slightly different formulations for the nonlinear interaction coefficients are available, depending on whether they are used to calculate the bound spectrum for the surface elevation (Hasselmann, 1962; Herbers & Burton, 1997), the pressure head at the bed (Herbers et al., 1994) or at an arbitrary depth (Smit et al., 2017), and whether it relates the free variance density at the surface or bed to the bound variance density at the surface or the bed. Here a generalized formula is presented, which is a slight adaptation of Smit et al. (2017), that links all different theories. In the following, we express the bound pressure-head variance density $E_b(z,f)$ at elevation z as a function of the free surface elevation variance density E:

$$E_b(z,f_p) = \frac{1}{2}\sum_{r=1}^{N_\theta}\sum_{s=1}^{N_\theta}\sum_{m=i_{min}}^{p-i_{min}} D^2(z,f_m,f_n,\theta_r,\theta_s)E(f_m,\theta_r)E(f_{p-m},\theta_s)\Delta f(\Delta\theta)^2 \tag{5.8}$$

so if instead of the free surface elevation variance density, the near-bed pressure-head variance densities are known, these should first be de-attenuated using $E(f_m) = E^{nb}(f_m)/K_{att}^2(f_m)$. The full expression of the nonlinear interaction coefficient

reads:

$$D(z,f_m,f_n,\theta_r,\theta_s) = \underbrace{\frac{\sigma_p^2}{\sigma_{b,p}^2-\sigma_p^2}\left(\frac{\sigma_m^2+\sigma_n^2+\sigma_m\sigma_n}{2g}-\frac{gk_mk_ncos(\Delta\theta)}{\sigma_m\sigma_n}-g\frac{k_m^2\sigma_n+k_n^2\sigma_m}{2\sigma_m\sigma_n\sigma_p}\right)}_{D_1}\underbrace{\frac{cosh(k_{b,p}(d+z))}{cosh(k_{b,p}d)}}_{K_{att,b,1}} \underbrace{-\frac{gk_mk_ncos(\Delta\theta)}{2\sigma_m\sigma_n}}_{D_2}\underbrace{\frac{cosh(k_m(d+z))}{cosh(k_md)}\frac{cosh(k_n(d+z))}{cosh(k_nd)}}_{K_{att,b,2}} + \underbrace{\frac{\sigma_m^2+\sigma_n^2+\sigma_m\sigma_n}{2g}}_{D_3}\underbrace{\frac{sinh(k_m(d+z))}{sinh(k_md)}\frac{sinh(k_n(d+z))}{sinh(k_nd)}}_{K_{att,b,3}} \tag{5.9}$$

in which σ is the intrinsic radial frequency, $cos(\Delta\theta) = |\theta_r - \theta_s|$, $k_{b,p} = \sqrt{k_m^2+k_n^2+2k_mk_ncos(\Delta\theta)}$, and $\sigma_{b,p} = \sqrt{gk_{b,p}tanh(k_{b,p}d)}$.

This expression can be split in three main terms, each of them attenuating at a different rate with z ($K_{att,b,1}$, $K_{att,b,2}$ and $K_{att,b,3}$ in Equation (5.9). At the surface ($z = 0$), $K_{att,b,1} = K_{att,b,2} = K_{att,b,3} = 1$, resulting in the expression that is equivalent to Hasselmann (1962) and Herbers & Burton (1997):

$$D(z=0,f_m,f_n,\theta_r,\theta_s) = \underbrace{\frac{\sigma_p^2}{\sigma_{b,p}^2-\sigma_p^2}\left(\frac{\sigma_m^2+\sigma_n^2+\sigma_m\sigma_n}{2g}-\frac{gk_mk_ncos(\Delta\theta)}{\sigma_m\sigma_n}-g\frac{k_m^2\sigma_n+k_n^2\sigma_m}{2\sigma_m\sigma_n\sigma_p}\right)}_{D_1} \underbrace{-\frac{gk_mk_ncos(\Delta\theta)}{2\sigma_m\sigma_n}}_{D_2}+\underbrace{\frac{\sigma_m^2+\sigma_n^2+\sigma_m\sigma_n}{2g}}_{D_3} \tag{5.10}$$

At the bed ($z = -d$), the numerator of the attenuation factors of the first two terms becomes 1 ($cosh(0) = 1$), whereas it becomes 0 for the third term ($sinh(0) = 0$). This results in the interaction coefficient at the bed, equal to the one presented by Herbers et al. (1994):

$$D(z=-d,f_m,f_n,\theta_r,\theta_s) = \underbrace{\frac{\sigma_p^2}{\sigma_{b,p}^2-\sigma_p^2}\left(\frac{\sigma_m^2+\sigma_n^2+\sigma_m\sigma_n}{2g}-\frac{gk_mk_ncos(\Delta\theta)}{\sigma_m\sigma_n}-g\frac{k_m^2\sigma_n+k_n^2\sigma_m}{2\sigma_m\sigma_n\sigma_p}\right)}_{D_1}\underbrace{\frac{1}{cosh(k_{b,p}d)}}_{K_{att,b,1}\text{ at z=-d}} \underbrace{-\frac{gk_mk_ncos(\Delta\theta)}{2\sigma_m\sigma_n}}_{D_2}\underbrace{\frac{1}{cosh(k_md)}\frac{1}{cosh(k_nd)}}_{K_{att,b,2}\text{ at z=-d}} \tag{5.11}$$

5.A.2. ATTENUATION OF THE BOUND WAVE AMPLITUDES AND VARIANCE DENSITY

The bound variance density obtained by the BWE model needs to be transformed into a near-bed (pressure head) bound variance density to allow for comparison with the data. Therefore, an attenuation factor needs to be defined for the bound variance. As a first step, we define this attenuation for the bound complex amplitude C_b.

Using the interaction coefficient introduced in Equation (5.9), and assuming unidirectional waves for the sake of simplicity, $C_b(z,f)$ can be expressed as a function of the complex amplitude of the primary component $C(z,f)$ as:

$$C_b(z,f_p) = \sum_m D(z,f_m,f_{p-m})C(z,f_m)C^*(z,f_{p-m}). \tag{5.12}$$

We have seen that the interaction coefficient D at elevation z consisted of three contributions with their own attenuation factors. Using the variables introduced in Equation (5.9), the interaction coefficient can be re-written as:

$$\begin{aligned} D(z,f_m,f_n) = {} & D_1(f_m,f_n)K_{att,b,1}(z,f_m,f_n) + D_2(f_m,f_n)K_{att,b,2}(z,f_m,f_n) \\ & + D_3(f_m,f_n)K_{att,b,3}(z,f_m,f_n) \end{aligned}$$

Factorizing by $D(0,f_m,f_n)$, interaction coefficient at the surface, and introducing the variables $\chi_i(f_m,f_n) = D_i(f_m,f_n)/D(0,f_m,f_n)$ (with i=1:3) which represent the relative contribution of each of the three terms to the total interaction coefficient, D can be re-written as:

$$\begin{aligned} D(z,f_m,f_n) = {} & (\chi_1(f_m,f_n)K_{att,b,1}(z,f_m,f_n) + \chi_2(f_m,f_n)K_{att,b,2}(z,f_m,f_n) \\ & + \chi_3(f_m,f_n)K_{att,b,3}(z,f_m,f_n))\, D(0,f_m,f_n) \end{aligned}$$

and thus

$$D(z,f_m,f_n) = K_{att,b}(z,f_m,f_n)D(0,f_m,f_n), \tag{5.13}$$

with

$$K_{att,b} = \chi_1 K_{att,b,1} + \chi_2 K_{att,b,2} + \chi_3 K_{att,b,3}. \tag{5.14}$$

$K_{att,b}$ can be seen as an attenuation factor applied to obtain D at elevation z from its value at the surface ($z=0$). Using this definition, Equation (5.12) is now rewritten as:

$$C_b(z,f_p) = \sum_m K_{att,b}(z,f_m,f_{p-m})D(0,f_m,f_{p-m})C(0,f_m)C^*(0,f_{p-m}). \tag{5.15}$$

Assuming $K_{att,b}(z,f_m,f_{p-m}) \approx K_{att,b}(z,f_{p/2},f_{p/2})$, i.e. that the bound energy at frequency f_p attenuates with depth at the same rate as the bound energy resulting from the self-interaction at $f_{p/2}$, Equation (5.15) becomes:

$$\begin{aligned} C_b(z,f_p) &\approx K_{att,b}(z,f_{p/2},f_{p/2}) \sum_m D(0,f_m,f_{p-m})C(0,f_m)C^*(0,f_{p-m}) \\ &\approx K_{att,b}(z,f_{p/2},f_{p/2})C_b(0,f_p), \end{aligned} \tag{5.16}$$

or, in terms of bound variance:

$$E_b(z,f_p) \approx K^2_{att,b}(z,f_{p/2},f_{p/2})E_b(0,f_p). \tag{5.17}$$

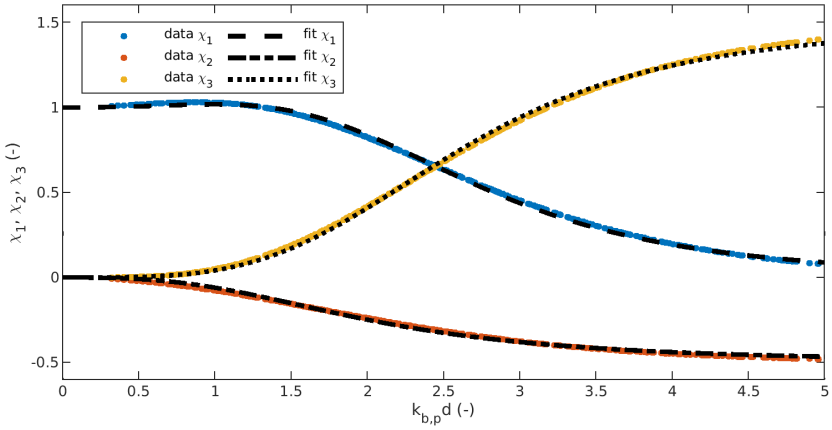

Figure 5.4: Computed (colored dots; Equation (5.10)) and estimated (black lines; Equations (5.18)-(5.20)) $\chi_1(f_{p/2}, f_{p/2})$, $\chi_2(f_{p/2}, f_{p/2})$ and $\chi_3(f_{p/2}, f_{p/2})$ as a function of $k_{b,p}d$

The (pressure-head) bound variance at elevation z can thus be estimated from bound variance at the surface if the attenuation factor $K_{att,b}(z, f_{p/2}, f_{p/2})$ is known. This attenuation factor is a function of the relative contributions of the three terms in the interaction coefficient $\chi_1(f_{p/2}, f_{p/2})$, $\chi_2(f_{p/2}, f_{p/2})$ and $\chi_3(f_{p/2}, f_{p/2})$. These $\chi-$terms could be directly calculated using Equation (5.10). However, this would be at the cost of significant computational effort. Instead it is shown in Figure 5.4 that χ_1, χ_2 and χ_3 can be expressed as a function of $k_{b,p}d$. For this visualization, the χ-terms were calculated for $0.08 \leq f_{p/2} \leq 0.25$ Hz and depths between 1 and 10 m. The shape of χ_2 and χ_3 as a function of $k_{b,p}d$ suggests a fit with the form of a Boltzman sigmoid. After an optimization routine, the following expressions are found and used to calculate $K_{att,b}$:

$$\chi_1 = 1 - \chi_2 - \chi_3 \tag{5.18}$$

$$\chi_2 = -\frac{0.5}{1 + \exp\left(\frac{0.303 - log(k_{b,p}d)}{0.152}\right)} \tag{5.19}$$

$$\chi_3 = \frac{1.5}{1 + \exp\left(\frac{0.416 - log(k_{b,p}d)}{0.117}\right)} \tag{5.20}$$

6

CONCLUSION

From a long term modelling perspective, there is a need to better capture the wave shape induced sediment transport. Therefore, this thesis aims to improve the accuracy of the nonlinear wave shape predictions in complex coastal systems. To achieve this aim, a combination of field measurements and numerical modelling is applied. Field measurements, obtained at the ebb-tidal delta seaward of the Ameland Inlet, are analyzed using timeseries analysis in Chapter 3 and bispectral analysis in Chapter 4. A new numerical modelling approach is presented in Chapter 5, which is validated with synthetic cases with unidirectional waves approaching a beach over a constant slope. Subsequently, in Chapter 6, the model is applied on field scale and compared to the aforementioned field measurements. This chapter provides an overview of the main conclusions of this thesis as well as a discussion on future developments.

6.1. CONCLUSIONS

Commonly, the wave shape is predicted based on the Ursell number, a dimensionless function of the local wave height, period and water depth. In this thesis the measured and modelled wave shape are compared to the wave shape from the Ursell based parameterization of Ruessink et al. (2012). Averaged over the 10 measurement locations ($4 < d < 11$ m) and all conditions ($0.5 < H < 6$ m and $5 < T_{peak} < 12$ s), the measured and parameterized wave shape are in good agreement. However, when considering a specific location or moment in time, significant over- or underestimations of the wave shape are observed. These mismatches can be ascribed to a number of reasons. Firstly, rapid changes in depth and currents have an immediate and significant effect on the Ursell number, whereas the response of the wave shape is less significant and slower. Secondly, even though longer waves are known to have a more pronounced nonlinear wave shape, lower longer waves with the same Ursell number as higher shorter waves (in a certain depth) have the same parameterized wave shape. Together this limits the predictive skill of Ursell based wave shape parameterizations and suggests on the one hand to adopt a non-local approach to predict the wave shape and on the other hand to better incorporate the effect of the wave length on nonlinear development.

By applying bispectral analysis to the field measurements, a clear relationship is found between the superharmonic bound wave height and the sea-swell wave shape. This implies that this relationship can be used to predict the wave shape if the spatial variation of the bound wave height is known. In phase-averaged models, the bound wave height can not be obtained using bispectral analysis. Alternatively, the bound wave height can be predicted using equilibrium second order wave theory. In deep water a near perfect match is found between the predicted and observed bound wave height. In presence of wave breaking, strong currents or strong nonlinearity, however, the second order theory fails to accurately predict the bound wave height, making it less suitable as a proxy for the wave shape.

The fact that triad source term formulations account for the energy transfer to the bound super (and sub) harmonics led to the idea that this source term can also be used to track the evolution of the bound wave energy (BWE). Source terms, extracted from the spectral wave model SWAN, are used to resolve an evolution equation for the bound variance density spectrum. Integration of this spectrum provides the modelled bound wave height, which can be used as a proxy for the wave shape. The model is validated for unidirectional, irregular waves propagating to the coast over a planar slope for varying peak wave periods and bed slopes. Comparing to results from the detailed wave-resolving model SWASH shows that the newly presented model is capable of resolving the evolution of the bound wave height and wave shape. The accuracy with which this is done, however, depends on the accuracy of the source terms and in particular that of the triad source term. Overall, the model's accuracy in predicting the bound wave height and the wave shape is higher in the shoaling zone (for which the model is optimized) than in the surf zone. To further increase the models performance in the surf zone, both the triad as well as the breaking source terms need to be further improved in these conditions.

The performance of the LTA (Eldeberky, 1996) and the SPB (Becq-Girard et al., 1999) triad source term formulations are tested for the above mentioned validation cases. SPB proves to be superior over LTA in predicting the amount of energy transferred to the higher harmonics, both using default calibration parameters as well as after optimization of these parameters. The optimal calibration settings for both formulations appear to be highly sensitive to the bed slope. LTA relies in particular on a parametrization of the biphase which does not account for the strong slope dependence. Also for SPB, a strong slope-dependence is found for the optimal calibration parameter K to estimate the imaginary part of the bispectrum. Furthermore, there is a strong suspicion that K should vary per interaction, but also that its spatial variability can be better represented than in the present SPB model. A further optimization of the dependence of K per interaction and in space is expected to improve both the magnitude and frequency-distribution of the nonlinear energy transfer, resulting in more accurate evolution of the spectral shape into the surf zone.

Finally, the model is applied on a field scale to verify to what extent it is capable of replicating the field measurements at the Ameland ebb-tidal delta. In contrast to the validation study, the simulations are performed with directionally spread waves coming in under an arbitrary angle instead of unidirectional waves perpendicularly approaching the coast. Furthermore, instead of using a planar slope, now the bathymetry measured along the main transect of the ebb-tidal delta is used. To compare near-bed measurements with

(free and bound) surface elevation variance density spectra obtained from the model, the modelled spectra are attenuated towards the bed. There is good agreement between the modelled and measured bound wave height and wave shape. In the shoaling and surf zone, the BWE model achieves the same accuracy as commonly used parameterizations. On top of the ebb-tidal shoal, where depth is constant or increasing again, the BWE model over predicts the bound wave height and wave shape. This is likely related to an erroneous estimate of the triad source term in this area as well as the absence of a source term accounting for the release of higher harmonics.

In conclusion, the BWE model presented in this thesis still needs further development before it is operationally applicable in morphodynamic models. Nevertheless, it is shown that resolving the bound energy evolution equation is a promising way to predict the spatial evolution of the nonlinear wave shape. This framework can be extended to 2D, currents can be added and other physical processes can be included through source term functions. This allows for the prediction of the wave shape in ebb tidal deltas.

6.2. OUTLOOK

6.2.1. SEPARATED SET OF MODEL EQUATIONS

Bound superharmonic waves are secondary (or higher) harmonics that are bound to their primary harmonics. This entails that their energy propagates with the group speed of the primary harmonics. Using the bound c_g for the bound evolution equation (Eq. (4.14)) would be formally more correct, but would be inconsistent with the governing equation of SWAN that assumes that the total energy (bound and free) propagates with the free c_g. Because the aim is to predict the bound proportion of the SWAN variance density, it was chosen to be consistent with SWAN and use the free c_g. Fortunately, before a substantial amount of the variance is bound it is relatively shallow water, where the difference between the free and bound c_g is less significant as waves become less dispersive.

In the future, we propose using two fully separated equations for the free and the bound energy evolution, in which energy propagates at their correct free or bound c_g, respectively. The triad source term would then remove energy from the free energy evolution equation and add it to the bound energy evolution equation (except in the case of recurrence where this would be the other way around). Furthermore, a source term can be added accounting for the release of higher harmonics and thus acting as a sink for the bound energy equation and as a source for the free energy equation.

Ideally, this two equation model is further extended to a three equation model where also the evolution of the bound subharmonics (bound infragravity waves) is resolved (following the method by Reniers & Zijlema (2022)). Similarly as for the super harmonics, the triad source term will act as a source for this evolution equation, provided that the SPB method or an alternative formulation is used that includes difference interactions. Eventually, additional source terms can be added accounting for the generation, release and breaking of infragravity waves.

Such sets of separated model equations are comparably fast as present spectral models, because the simulation time for solving an evolution equation is negligible in comparison to the calculation time of the source terms. The models capabilities are however much larger because it can predict the bound wave height, wave shape, and potentially

the infragravity wave height. A final advantage of this separated set of equations model, discussed in this Section, is that ongoing research on the source terms, in particular for the triads, will keep improving the accuracy of the model outcome.

6.2.2. IMPLICATIONS FOR SEDIMENT TRANSPORT MODELING

Although the evolution of waves into sharp crested and pitched forward shapes is a fascinating hydrodynamic process, the primary interest in the nonlinear wave shape is from a sediment transport perspective. From this perspective the main question is to link the quantity of transported sediment to the nonlinear wave shape. Whereas the scope of this Thesis is restricted to a better prediction of the nonlinear wave shape, this final Section discusses the implications of these findings on sediment transport and how to incorporate these findings in sediment transport modelling in the future.

One of the findings of this Thesis is that the wave shape does not instantly adapt to new conditions but needs time to adapt. This can be accounted for by using a delayed Ursell number (Chapter 2) or by applying an evolution equation for the wave shape (Chapters 4 and 5). This means that for an increase in Ur (e.g., for decreasing depth), the increase in Sk, As and concurrent sediment transport is more gradual. Vice versa, in case of a decrease in Ur (e.g., due to increasing depth or wave breaking), Sk and As do not instantly decrease but take a number of wave lengths to respond, resulting in a larger sediment transport compared to the instantaneous response. As morphological changes are a function of spatial gradients in sediment transport, the morphological changes are also expected to be smoother. Furthermore, the down-wave spatial delay in wave shape and associated sediment transport with respect to bed features like sand bars is expected to affect both the propagation speed and growth rate of these features (Hoefel & Elgar, 2003; Roelvink & Reniers, 2011).

In Chapter 2, it was shown that for a certain depth lower longer waves have the same Ur as higher shorter waves. This is in conflict with the theory of Hasselmann (1962), which shows that longer waves have stronger nonlinear interactions. Therefore, by using an Ur-based parameterization, the wave shape is underestimated for lower longer waves and overestimated for higher shorter waves (see Fig. 2.10b). This implies that also the associated sediment transport is erroneously predicted in the same way.

The above examples show qualitative differences in sediment transport predictions based on the findings in this thesis. In order to quantitatively predict wave-shape transport it is recommended to incorporate the BWE equation in a morphodynamic model that uses sediment transport formulas taking into account the combined effect of currents and nonlinear waves through the near-bed wave shape (e.g., Van Rijn, 2007; Dubarbier et al., 2015; Fernández-Mora et al., 2015). This requires one additional step, which is the translation of the wave shape at the sea-surface, as provided by BWE equation, to the shape of the near-bed velocity signal, which is eventually the driver of wave-shape transport. There are multiple ways this can be done. The first is using linear wave theory to translate pressure (or elevation) to near-bed velocity (as applied in Chapter 2). It is, however, incorrect to translate a nonlinear signal with linear theory. Alternatively, given that the amount of free and bound energy is known, a nonlinear translation method based on second order Stokes theory (e.g., Smit et al., 2017) can be applied (similar as presented in Appendix 5.A). Since all higher order Stokes wave theories are equilibrium theories, they only predict skewed

waves with zero asymmetry. To make the distinction between skewness and asymmetry, a biphase parameterization can be used. This final step allows for the BWE model to be applicable in combined morphodynamic wave-flow modelling.

REFERENCES

Aagaard, T., Hughes, M., Møller-Sørensen, R., & Andersen, S. (2006). Hydrodynamics and sediment fluxes across an onshore migrating intertidal bar. *Journal of Coastal Research*, 2006(222), 247–259.

Abreu, T., Silva, P. A., Sancho, F., & Temperville, A. (2010). Analytical approximate wave form for asymmetric waves. *Coastal Engineering*, 57(7), 656–667.

Abreu, T. A. M. A. (2011). *Coastal sediment dynamics under asymmetric waves and currents: measurements and simulations*. PhD thesis, Faculty of Sciences and Technology of the University of Coimbra.

Agnon, Y., Sheremet, A., Gonsalves, J., & Stiassnie, M. (1993). Nonlinear evolution of a unidirectional shoaling wave field. *Coastal Engineering*, 20(1-2), 29–58.

Armstrong, J., Bloembergen, N., Ducuing, J., & Pershan, P. S. (1962). Interactions between light waves in a nonlinear dielectric. *Physical review*, 127(6), 1918.

Bagnold, R. A. (1966). *An approach to the sediment transport problem from general physics*. US government printing office.

Bailard, J. A. (1981). An energetics total load sediment transport model for a plane sloping beach. *Journal of Geophysical Research: Oceans*, 86(C11), 10938–10954.

Baldock, T. E. (2012). Dissipation of incident forced long waves in the surf zone—implications for the concept of "bound" wave release at short wave breaking. *Coastal Engineering*, 60, 276–285.

Battjes, J. A. & Janssen, J. P. F. M. (1978). Energy loss and set-up due to breaking of random waves. In *Coastal Engineering 1978* (pp. 569–587). American Society of Civil Engineers.

Battjes, J. A. & Stive, M. J. F. (1985). Calibration and verification of a dissipation model for random breaking waves. *Journal of Geophysical Research: Oceans*, 90(C5), 9159–9167.

Becq, F. (1998). *Extension de la modélisation spectrale des états de mer vers le domaine côtier*. PhD thesis, Toulon.

Becq, F., Benoit, M., & Forget, P. (1998). Numerical simulations of directionally spread shoaling surface gravity waves. In *Coastal Engineering 1998* (pp. 523–536). American Society of Civil Engineers.

Becq-Girard, F., Forget, P., & Benoit, M. (1999). Non-linear propagation of unidirectional wave fields over varying topography. *Coastal Engineering*, 38(2), 91–113.

Beji, S. & Battjes, J. A. (1993). Experimental investigation of wave propagation over a bar. *Coastal Engineering*, 19(1-2), 151–162.

Beji, S. & Battjes, J. A. (1994). Numerical simulation of nonlinear wave propagation over a bar. *Coastal Engineering*, 23(1-2), 1–16.

Benney, D. J. & Saffman, P. G. (1966). Nonlinear interactions of random waves in a dispersive medium. *Proceedings of the Royal Society of London. Series A. Mathematical and Physical Sciences*, 289(1418), 301–320.

Benoit, M., Marcos, F., & Becq, F. (1997). Development of a third generation shallow-water wave model with unstructured spatial meshing. In *Coastal Engineering 1996* (pp. 465–478). American Society Of Civil Engineers.

Bijker, E. W. (1967). Some considerations about scales for coastal models with movable bed. *Delft Hydraulics Laboratory Publication 50*.

Birkemeier, W. A., Long, C. E., & Hathaway, K. K. (1997). Delilah, duck94 & sandyduck: Three nearshore field experiments. In *Coastal Engineering 1996* (pp. 4052–4065). American Society Of Civil Engineers.

Bishop, C. T. & Donelan, M. A. (1987). Measuring waves with pressure transducers. *Coastal Engineering*, 11(4), 309–328.

Boechat Albernaz, M., Ruessink, G., Jagers, B., & Kleinhans, M. (2019). Effects of wave orbital velocity parameterization on nearshore sediment transport and decadal morphodynamics. *Journal of Marine Science and Engineering*, 7(6), 188.

Bonneton, P., Barthélemy, E., Chazel, F., Cienfuegos, R., Lannes, D., Marche, F., & Tissier, M. (2011). Recent advances in serre–green naghdi modelling for wave transformation, breaking and runup processes. *European Journal of Mechanics-B/Fluids*, 30(6), 589–597.

Bonneton, P. & Lannes, D. (2017). Recovering water wave elevation from pressure measurements. *Journal of Fluid Mechanics*, 833, 399–429.

Booij, N., Holthuijsen, L. H., & Ris, R. C. (1997). The "swan" wave model for shallow water. In *Coastal Engineering 1996* (pp. 668–676). American Society of Civil Engineers.

Booij, N., Ris, R. C., & Holthuijsen, L. H. (1999). A third-generation wave model for coastal regions: 1. model description and validation. *Journal of geophysical research: Oceans*, 104(C4), 7649–7666.

Bosboom, J. & Klopman, G. (2001). Intra-wave sediment transport modelling. In *Coastal Engineering 2000* (pp. 2453–2466). American Society Of Civil Engineers.

Bowen, A. J. (1980). Simple models of nearshore sedimentation: Beach profiles and longshore bars. *The coastline of Canada*.

Brakenhoff, L., Kleinhans, M., Ruessink, G., & van der Vegt, M. (2020a). Spatio-temporal characteristics of small-scale wave–current ripples on the ameland ebb-tidal delta. *Earth Surface Processes and Landforms*, 45(5), 1248–1261.

Brakenhoff, L., Ruessink, B. G., & van der Vegt, M. (2019). Characteristics of saw-tooth bars on the ebb-tidal deltas of the wadden islands. *Ocean Dynamics*, 69(11), 1273–1285.

Brakenhoff, L., Schrijvershof, R., Van Der Werf, J., Grasmeijer, B., Ruessink, B. G., & Van Der Vegt, M. (2020b). From ripples to large-scale sand transport: The effects of bedform-related roughness on hydrodynamics and sediment transport patterns in delft3d. *Journal of Marine Science and Engineering*, 8(11), 892.

Brakenhoff, L. B. (2021). *Bedforms and their effect on sediment transport on ebb-tidal deltas*. PhD thesis, University Utrecht.

Brand, E., Ramaekers, G., & Lodder, Q. (2022). Dutch experience with sand nourishments for dynamic coastline conservation–an operational overview. *Ocean & Coastal Management*, 217, 106008.

Bretherton, F. P. (1964). Resonant interactions between waves. the case of discrete oscillations. *Journal of Fluid Mechanics*, 20(3), 457–479.

Bretherton, F. P. & Garrett, C. J. R. (1968). Wavetrains in inhomogeneous moving media. *Proceedings of the Royal Society of London. Series A. Mathematical and Physical Sciences*, 302(1471), 529–554.

Calantoni, J. & Puleo, J. A. (2006). Role of pressure gradients in sheet flow of coarse sediments under sawtooth waves. *Journal of Geophysical Research: Oceans*, 111(C1).

Cayocca, F. (2001). Long-term morphological modeling of a tidal inlet: the arcachon basin, france. *Coastal engineering*, 42(2), 115–142.

Chen, H., Tang, X., Zhang, R., & Gao, J. (2018). Effect of bottom slope on the nonlinear triad interactions in shallow water. *Ocean Dynamics*, 68(4), 469–483.

Chen, J.-L., Hsu, T.-J., Shi, F., Raubenheimer, B., & Elgar, S. (2015). Hydrodynamic and sediment transport modeling of new river inlet (nc) under the interaction of tides and waves. *Journal of Geophysical Research: Oceans*, 120(6), 4028–4047.

Chen, Q., Madsen, P. A., & Basco, D. R. (1999). Current effects on nonlinear interactions of shallow-water waves. *Journal of waterway, port, coastal, and ocean engineering*, 125(4), 176–186.

Chen, Y., Guza, R. T., & Elgar, S. (1997). Modeling spectra of breaking surface waves in shallow water. *Journal of Geophysical Research: Oceans*, 102(C11), 25035–25046.

De Bakker, A. T. M., Herbers, T. H. C., Smit, P. B., Tissier, M. F. S., & Ruessink, B. G. (2015). Nonlinear infragravity–wave interactions on a gently sloping laboratory beach. *Journal of Physical Oceanography*, 45(2), 589–605.

De Bakker, A. T. M., Tissier, M. F. S., & Ruessink, B. G. (2016). Beach steepness effects on nonlinear infragravity-wave interactions: A numerical study. *Journal of Geophysical Research: Oceans*, 121(1), 554–570.

de Schipper, M. A., de Vries, S., Ruessink, B. G., de Zeeuw, R. C., Rutten, J., van Gelder-Maas, C., & Stive, M. J. F. (2016). Initial spreading of a mega feeder nourishment: Observations of the sand engine pilot project. *Coastal Engineering*, 111, 23–38.

de Vriend, H. J., Capobianco, M., Chesher, T., De Swart, H. E. d., Latteux, B., & Stive, M. J. F. (1993). Approaches to long-term modelling of coastal morphology: a review. *Coastal engineering*, 21(1-3), 225–269.

de Wit, F. P., Tissier, M. F. S., & Reniers, A. J. H. M. (2017). Including tidal currents in a wave-resolving model. *Proceedings of Coastal Dynamics 2017*.

De Wit, F. P., Tissier, M. F. S., & Reniers, A. J. H. M. (2019). Characterizing wave shape evolution on an ebb tidal shoal. *Journal of Marine Science and Engineering*, 7(10), 367.

de Wit, F. P., Tissier, M. F. S., & Reniers, A. J. H. M. (2020). The relationship between sea-swell bound wave height and wave shape. *Journal of Marine Science and Engineering*, 8(9), 643.

Dean, R. G. (1970). Relative validities of water wave theories. *Journal of the Waterways, Harbors and Coastal Engineering Division*, 96(1), 105–119.

Dean, R. G. (2002). *Beach nourishment: theory and practice*, volume 18. World scientific.

Dibajnia, M., Moriya, T., & Watanabe, A. (2001). A representative wave model for estimation of nearshore local transport rate. *Coastal Engineering Journal*, 43(1), 1–38.

Dodet, G., Bertin, X., Bruneau, N., Fortunato, A. B., Nahon, A., & Roland, A. (2013). Wave-current interactions in a wave-dominated tidal inlet. *Journal of Geophysical Research: Oceans*, 118(3), 1587–1605.

Doering, J. C. & Bowen, A. J. (1995). Parametrization of orbital velocity asymmetries of shoaling and breaking waves using bispectral analysis. *Coastal Engineering*, 26(1-2), 15–33.

Dong, G., Chen, H., & Ma, Y. (2014). Parameterization of nonlinear shallow water waves over sloping bottoms. *Coastal Engineering*, 94, 23–32.

Drake, T. G. & Calantoni, J. (2001). Discrete particle model for sheet flow sediment transport in the nearshore. *Journal of Geophysical Research: Oceans*, 106(C9), 19859–19868.

Dubarbier, B., Castelle, B., Marieu, V., & Ruessink, B. G. (2015). Process-based modeling of cross-shore sandbar behavior. *Coastal Engineering*, 95, 35–50.

Dubois, R. N. (1988). Seasonal changes in beach topography and beach volume in delaware. *Marine Geology*, 81(1-4), 79–96.

Eldeberky, Y. (1996). Nonlinear transformation of wave spectra in the nearshore zone (ph. d. thesis). *Netherlands: Delft University of Technology, Department of Civil Engineering*.

Eldeberky, Y. & Battjes, J. A. (1994). Phase lock in waves passing over a bar. In *Int. Symp.: Waves—Physical and Numerical Modeling, Vancouver* (pp. 1086–1095).

Eldeberky, Y. & Madsen, P. A. (1999). Deterministic and stochastic evolution equations for fully dispersive and weakly nonlinear waves. *Coastal Engineering*, 38(1), 1–24.

Eldrup, M. R. & Andersen, T. L. (2020). Numerical study on regular wave shoaling, deshoaling and decomposition of free/bound waves on gentle and steep foreshores. *Journal of Marine Science and Engineering*, 8(5), 334.

Elgar, S., Freilich, M. H., & Guza, R. T. (1990). Recurrence in truncated boussinesq models for nonlinear waves in shallow water. *Journal of Geophysical Research: Oceans*, 95(C7), 11547–11556.

Elgar, S., Gallagher, E. L., & Guza, R. T. (2001). Nearshore sandbar migration. *Journal of Geophysical Research: Oceans*, 106(C6), 11623–11627.

Elgar, S. & Guza, R. T. (1985). Observations of bispectra of shoaling surface gravity waves. *Journal of Fluid Mechanics*, 161, 425–448.

Elgar, S. & Guza, R. T. (1988). Statistics of bicoherence. *IEEE Transactions on Acoustics, Speech, and Signal Processing*, 36(10), 1667–1668.

Elgar, S., Guza, R. T., Raubenheimer, B., Herbers, T. H. C., & Gallagher, E. L. (1997). Spectral evolution of shoaling and breaking waves on a barred beach. *Journal of Geophysical Research: Oceans*, 102(C7), 15797–15805.

Elgar, S., Raubenheimer, B., & Guza, R. T. (2005). Quality control of acoustic doppler velocimeter data in the surfzone. *Measurement Science and Technology*, 16(10), 1889.

Elgar, S. & Sebert, G. (1989). Statistics of bicoherence and biphase. *Journal of Geophysical Research: Oceans*, 94(C8), 10993–10998.

Elias, E., Stive, M., Bonekamp, H., & Cleveringa, J. (2003). Tidal inlet dynamics in response to human intervention. *Coastal engineering journal*, 45(04), 629–658.

Elias, E. P. & van der Spek, A. J. F. (2006). Long-term morphodynamic evolution of texel inlet and its ebb-tidal delta (the netherlands). *Marine Geology*, 225(1-4), 5–21.

Elias, E. P. L., Van der Spek, A. J. F., Pearson, S. G., & Cleveringa, J. (2019). Understanding sediment bypassing processes through analysis of high-frequency observations of ameland inlet, the netherlands. *Marine Geology*, 415, 105956.

Elias, E. P. L., Walstra, D. J. R., Roelvink, J. A., Stive, M. J. F., & Klein, M. D. (2001). Hydrodynamic validation of delft3d with field measurements at egmond. In *Coastal Engineering 2000* (pp. 2714–2727). American Society Of Civil Engineers.

Fenton, J. D. (1990). Nonlinear wave theories. *the Sea*, 9(1), 3–25.

Fernández-Mora, A., Calvete, D., Falqués, A., & de Swart, H. E. (2015). Onshore sandbar migration in the surf zone: New insights into the wave-induced sediment transport mechanisms. *Geophysical research letters*, 42(8), 2869–2877.

Fiedler, J. W., Smit, P. B., Brodie, K. L., McNinch, J., & Guza, R. (2019). The offshore boundary condition in surf zone modeling. *Coastal Engineering*, 143, 12–20.

Filipot, J.-F. (2015). Investigation of the bottom-slope dependence of the nonlinear wave evolution toward breaking using swash. *Journal of Coastal Research*, 32(6), 1504–1507.

Finley, R. J. (1978). Ebb-tidal delta morphology and sediment supply in relation to seasonal wave energy flux, north inlet, south carolina. *Journal of Sedimentary Research*, 48(1), 227–238.

Fitzgerald, D. M. (1984). Interactions between the ebb-tidal delta and landward shoreline; price inlet, south carolina. *Journal of Sedimentary Research*, 54(4), 1303–1318.

Fredsøe, J. (1984). Turbulent boundary layer in wave-current motion. *Journal of Hydraulic Engineering*, 110(8), 1103–1120.

Freilich, M. H. & Guza, R. T. (1984). Nonlinear effects on shoaling surface gravity waves. *Philosophical Transactions of the Royal Society of London. Series A, Mathematical and Physical Sciences*, 311(1515), 1–41.

Freilich, M. H., Guza, R. T., & Elgar, S. L. (1990). Observations of nonlinear effects in directional spectra of shoaling gravity waves. *Journal of Geophysical Research: Oceans*, 95(C6), 9645–9656.

Gallagher, E. L., Elgar, S., & Guza, R. T. (1998). Observations of sand bar evolution on a natural beach. *Journal of Geophysical Research: Oceans*, 103(C2), 3203–3215.

Gonzalez-Rodriguez, D. & Madsen, O. S. (2007). Seabed shear stress and bedload transport due to asymmetric and skewed waves. *Coastal Engineering*, 54(12), 914–929.

Goring, D. G. & Nikora, V. I. (2002). Despiking acoustic doppler velocimeter data. *Journal of Hydraulic Engineering*, 128(1), 117–126.

Grant, W. D. & Madsen, O. S. (1979). Combined wave and current interaction with a rough bottom. *Journal of Geophysical Research: Oceans*, 84(C4), 1797–1808.

Groeneweg, J., van der Westhuysen, A., van Vledder, G., Jacobse, S., Lansen, J., & van Dongeren, A. (2009). Wave modelling in a tidal inlet: Performance of swan in the wadden sea. In *Coastal Engineering 2008: (In 5 Volumes)* (pp. 411–423). World Scientific.

Grunnet, N. M. & Ruessink, B. G. (2005). Morphodynamic response of nearshore bars to a shoreface nourishment. *Coastal Engineering*, 52(2), 119–137.

Guedes, R. M. C., Bryan, K. R., & Coco, G. (2013). Observations of wave energy fluxes and swash motions on a low-sloping, dissipative beach. *Journal of Geophysical Research: Oceans*, 118(7), 3651–3669.

Guza, R. T. & Thornton, E. B. (1980). Local and shoaled comparisons of sea surface elevations, pressures, and velocities. *Journal of Geophysical Research: Oceans*, 85(C3), 1524–1530.

Hamm, L., Capobianco, M., Dette, H. H., Lechuga, A., Spanhoff, R., & Stive, M. J. F. (2002). A summary of european experience with shore nourishment. *Coastal engineering*, 47(2), 237–264.

Hanson, H., Brampton, A., Capobianco, M., Dette, H. H., Hamm, L., Laustrup, C., Lechuga, A., & Spanhoff, R. (2002). Beach nourishment projects, practices, and objectives—a european overview. *Coastal engineering*, 47(2), 81–111.

Hasselmann, K. (1962). On the non-linear energy transfer in a gravity-wave spectrum part 1. general theory. *Journal of Fluid Mechanics*, 12(4), 481–500.

Hasselmann, K., Munk, W., & MacDonald, G. (1963). Bispectra of ocean waves, time series analysis m. rosenblatt, 125–139.

Haubrich, R. A. (1965). Earth noise, 5 to 500 millicycles per second: 1. spectral stationarity, normality, and nonlinearity. *Journal of Geophysical Research*, 70(6), 1415–1427.

Hayes, M. O. (1980). General morphology and sediment patterns in tidal inlets. *Sedimentary geology*, 26(1-3), 139–156.

Hayes, M. O., Goldsmith, V., & Hobbs III, C. H. (1970). Offset coastal inlets. In *Coastal Engineering 1970* (pp. 1187–1200). American Society of Civil Engineers.

Hedges, T. S. (1995). Regions of validity of analytical wave theories. *Proceedings of the Institution of Civil Engineers-Water Maritime and Energy*, 112(2), 111–114.

Hedges, T. S., Anastasiou, K., & Gabriel, D. (1985). Interaction of random waves and currents. *Journal of waterway, port, coastal, and ocean engineering*, 111(2), 275–288.

Henderson, S. M., Allen, J. S., & Newberger, P. A. (2004). Nearshore sandbar migration predicted by an eddy-diffusive boundary layer model. *Journal of Geophysical Research: Oceans*, 109(C6).

Henderson, S. M., Guza, R. T., Elgar, S., Herbers, T. H. C., & Bowen, A. J. (2006). Nonlinear generation and loss of infragravity wave energy. *Journal of Geophysical Research: Oceans*, 111(C12).

Henriquez, M., Reniers, A. J. H. M., Ruessink, B. G., & Stive, M. (2010). Wave boundary layer hydrodynamics during onshore bar migration. *COASTAL ENGINEERING*, (pp.2̃).

Henriquez, M., Reniers, A. J. H. M., Ruessink, B. G., & Stive, M. J. F. (2014). Piv measurements of the bottom boundary layer under nonlinear surface waves. *Coastal Engineering*, 94, 33–46.

Herbers, T. H. C. & Burton, M. C. (1997). Nonlinear shoaling of directionally spread waves on a beach. *Journal of Geophysical Research: Oceans*, 102(C9), 21101–21114.

Herbers, T. H. C., Elgar, S., & Guza, R. T. (1994). Infragravity-frequency (0.005–0.05 hz) motions on the shelf. part i: Forced waves. *Journal of Physical Oceanography*, 24(5), 917–927.

Herbers, T. H. C., Elgar, S., & Guza, R. T. (1999). Directional spreading of waves in the nearshore. *Journal of Geophysical Research: Oceans*, 104(C4), 7683–7693.

Herbers, T. H. C. & Guza, R. T. (1991). Wind-wave nonlinearity observed at the sea floor. part i: Forced-wave energy. *Journal of physical oceanography*, 21(12), 1740–1761.

Herbers, T. H. C. & Guza, R. T. (1992). Wind-wave nonlinearity observed at the sea floor. part ii: Wavenumbers and third-order statistics. *Journal of physical oceanography*, 22(5), 489–504.

Herbers, T. H. C. & Guza, R. T. (1994). Nonlinear wave interactions and high-frequency seafloor pressure. *Journal of Geophysical Research: Oceans*, 99(C5), 10035–10048.

Herbers, T. H. C., Lowe, R. L., & Guza, R. T. (1992). Field observations of orbital velocities and pressure in weakly nonlinear surface gravity waves. *Journal of Fluid Mechanics*, 245, 413–435.

Hoefel, F. & Elgar, S. (2003). Wave-induced sediment transport and sandbar migration. *Science*, 299(5614), 1885–1887.

Holloway, G. (1980). Oceanic internal waves are not weak waves. *Journal of Physical Oceanography*, 10(6), 906–914.

Holthuijsen, L. (1999). *The Continued Development of the Third-generation Shallow Water Wave Model 'Swan'*. Technical report, Delft University of Technology.

Holzhauer, H., Borsje, B. W., Herman, P. M. J., Schipper, C. A., & Wijnberg, K. M. (2022). The geomorphology of an ebb-tidal-delta linked to benthic species distribution and functionality. *Ocean & Coastal Management*, 216, 105938.

Holzhauer, H., Borsje, B. W., Van Dalfsen, J. A., Wijnberg, K. M., Hulscher, S. J. M. H., & Herman, P. M. J. (2020). Benthic species distribution linked to morphological features of a barred coast. *Journal of marine science and engineering*, 8(1), 16.

Hsu, T.-J., Elgar, S., & Guza, R. T. (2006). Wave-induced sediment transport and onshore sandbar migration. *Coastal Engineering*, 53(10), 817–824.

Hsu, T.-J. & Hanes, D. M. (2004). Effects of wave shape on sheet flow sediment transport. *Journal of Geophysical Research: Oceans*, 109(C5).

Isobe, M. & Horikawa, K. (1982). Study on water particle velocities of shoaling and breaking waves. *Coastal Engineering in Japan*, 25(1), 109–123.

Jacobsen, N. G., Fuhrman, D. R., & Fredsøe, J. (2012). A wave generation toolbox for the open-source cfd library: Openfoam®. *International Journal for numerical methods in fluids*, 70(9), 1073–1088.

Janssen, T. T., Herbers, T. H. C., & Battjes, J. A. (2006). Generalized evolution equations for nonlinear surface gravity waves over two-dimensional topography. *Journal of Fluid Mechanics*, 552, 393–418.

Kabat, P., Fresco, L. O., Stive, M. J. F., Veerman, C. P., Van Alphen, J. S. L. J., Parmet, B. W. A. H., Hazeleger, W., & Katsman, C. A. (2009). Dutch coasts in transition. *Nature Geoscience*, 2(7), 450–452.

Kaihatu, J. M. (2009). Application of a nonlinear frequency domain wave–current interaction model to shallow water recurrence effects in random waves. *Ocean Modelling*, 26(3-4), 190–205.

Kaihatu, J. M. & Kirby, J. T. (1995). Nonlinear transformation of waves in finite water depth. *Physics of Fluids*, 7(8), 1903–1914.

Katsman, C. A., Sterl, A., Beersma, J. J., Van den Brink, H. W., Church, J. A., Hazeleger, W., Kopp, R. E., Kroon, D., Kwadijk, J., Lammersen, R., et al. (2011). Exploring high-end scenarios for local sea level rise to develop flood protection strategies for a low-lying delta—the netherlands as an example. *Climatic change*, 109(3-4), 617–645.

Kim, Y. C. & Powers, E. J. (1979). Digital bispectral analysis and its applications to nonlinear wave interactions. *IEEE transactions on plasma science*, 7(2), 120–131.

King Jr, D. B. (1991). *Studies in oscillatory flow bedload sediment transport*. University of California, San Diego.

Kranenburg, W. M., Ribberink, J. S., Schretlen, J. J., & Uittenbogaard, R. E. (2013). Sand transport beneath waves: The role of progressive wave streaming and other free surface effects. *Journal of Geophysical Research: Earth Surface*, 118(1), 122–139.

Kristensen, S. E., Deigaard, R., Taaning, M., Fredsøe, J., Drønen, N., & Jensen, J. H. (2010). Long term morphological modelling. In *32nd International Conference on Coastal Engineering*: American Society of Civil Engineers.

Kroon, A., de Schipper, M., de Vries, S., & Aarninkhof, S. (2022). Subaqueous and subaerial beach changes after implementation of a mega nourishment in front of a sea dike. *Journal of Marine Science and Engineering*, 10(8), 1152.

Le Méhauté, B. (1976). An introduction to water waves. In *An Introduction to Hydrodynamics and Water Waves* (pp. 197–211). Springer.

Leckler, F., Ardhuin, F., Peureux, C., Benetazzo, A., Bergamasco, F., & Dulov, V. (2015). Analysis and interpretation of frequency–wavenumber spectra of young wind waves. *Journal of Physical Oceanography*, 45(10), 2484–2496.

Lenstra, K. J. H., Pluis, S. R. P. M., Ridderinkhof, W., Ruessink, B. G., & van der Vegt, M. (2019). Cyclic channel-shoal dynamics at the ameland inlet: the impact on waves, tides, and sediment transport. *Ocean Dynamics*, 69(4), 409–425.

Lesser, G. R., Roelvink, J. A., Van Kester, J. A. T. M., & Stelling, G. S. (2004). Development and validation of a three-dimensional morphological model. *Coastal engineering*, 51(8-9), 883–915.

Longuet-Higgins, M. S. (1956). The refraction of sea waves in shallow water. *Journal of Fluid Mechanics*, 1(2), 163–176.

Luettich, J., Richard, A., Westerink, J. J., & Scheffner, N. W. (1992). *ADCIRC: An Advanced Three-Dimensional Circulation Model for Shelves, Coasts, and Estuaries. Report 1. Theory and Methodology of ADCIRC-2DDI and ADCIRC-3DL*. Technical report, Coastal engineering research center vicksburg MS.

Luijendijk, A. P., Ranasinghe, R., de Schipper, M. A., Huisman, B. A., Swinkels, C. M., Walstra, D. J. R., & Stive, M. J. F. (2017). The initial morphological response of the sand engine: A process-based modelling study. *Coastal engineering*, 119, 1–14.

Luth, H. R., Klopman, G., & Kitou, N. (1994). Kinematics of waves breaking partially on an offshore bar; ldv measurements of waves with and without a net onshore current. *Report H-1573, Delft Hydraulics*, 40.

Lygre, A. & Krogstad, H. E. (1986). Maximum entropy estimation of the directional distribution in ocean wave spectra. *Journal of Physical Oceanography*, 16(12), 2052–2060.

Ma, G., Shi, F., & Kirby, J. T. (2012). Shock-capturing non-hydrostatic model for fully dispersive surface wave processes. *Ocean Modelling*, 43, 22–35.

Madsen, O. S. (1971). On the generation of long waves. *Journal of Geophysical Research*, 76(36), 8672–8683.

Madsen, O. S. & Grant, W. D. (1977). Quantitative description of sediment transport by waves. In *Coastal Engineering 1976* (pp. 1092–1112). American Society of Civil Engineers.

Madsen, P. A. & Eldeberky, Y. (1999). A new formulation of deterministic and stochastic evolution equations for three-wave interactions involving fully dispersive waves. In *Coastal Engineering 1998* (pp. 161–174). American Society of Civil Engineers.

Madsen, P. A. & Sørensen, O. R. (1992). A new form of the boussinesq equations with improved linear dispersion characteristics. part 2. a slowly-varying bathymetry. *Coastal engineering*, 18(3-4), 183–204.

Madsen, P. A. & Sørensen, O. R. (1993). Bound waves and triad interactions in shallow water. *Ocean Engineering*, 20(4), 359–388.

Madsen, P. A., Sørensen, O. R., & Schäffer, H. A. (1997). Surf zone dynamics simulated by a boussinesq type model. part i. model description and cross-shore motion of regular waves. *Coastal Engineering*, 32(4), 255–287.

Mahmoudof, S. M., Badiei, P., Siadatmousavi, S. M., & Chegini, V. (2016). Observing and estimating of intensive triad interaction occurrence in very shallow water. *Continental Shelf Research*, 122, 68–76.

Mase, H. & Kirby, J. T. (1992). Hybrid frequency-domain kdv equation for random wave transformation. In *Coastal Engineering 1992* (pp. 474–487). American Society of Civil Engineers.

Masselink, G. (1998). Field investigation of wave propagation over a bar and the consequent generation of secondary waves. *Coastal Engineering*, 33(1), 1–9.

Masselink, G., Austin, M. J., O'Hare, T. J., & Russell, P. E. (2007). Geometry and dynamics of wave ripples in the nearshore zone of a coarse sandy beach. *Journal of Geophysical Research: Oceans*, 112(C10).

McComas, C. H. & Briscoe, M. G. (1980). Bispectra of internal waves. *Journal of Fluid Mechanics*, 97(1), 205–213.

Miles, J. (2013). Wave shape effects on sediment transport. *Journal of Coastal Research*, 65(sp2), 1803–1808.

Monbaliu, J., Padilla-Hernandez, R., Hargreaves, J. C., Albiach, J. C. C., Luo, W., Sclavo, M., & Guenther, H. (2000). The spectral wave model, wam, adapted for applications with high spatial resolution. *Coastal engineering*, 41(1-3), 41–62.

Mori, N., Suzuki, T., & Kakuno, S. (2007). Noise of acoustic doppler velocimeter data in bubbly flows. *Journal of engineering mechanics*, 133(1), 122–125.

Mouragues, A., Bonneton, P., Lannes, D., Castelle, B., & Marieu, V. (2019). Field data-based evaluation of methods for recovering surface wave elevation from pressure measurements. *Coastal Engineering*, 150, 147–159.

Mulder, J. P. M. (2000). Zandverliezen in het nederlandse kustsysteem: Advies voor dynamisch handhaven in de 21e eeuw. *rapport RIKZ/2000.36*.

Nederhoff, C. M., Schrijvershof, R. A., Tonnon, P. K., Van Der Werf, J. J., & Elias, E. P. L. (2019). Modelling hydrodynamics in the ameland inlet as a basis for studying sand transport. In *The Proceedings of the Coastal Sediments 2019*. World Scientific.

Nielsen, P. (1988). Three simple models of wave sediment transport. *Coastal Engineering*, 12(1), 43–62.

Nielsen, P. (1992). *Coastal bottom boundary layers and sediment transport*, volume 4. World scientific.

Nielsen, P. (2006). Sheet flow sediment transport under waves with acceleration skewness and boundary layer streaming. *Coastal Engineering*, 53(9), 749–758.

Norheim, C. A., Herbers, T. H. C., & Elgar, S. (1998). Nonlinear evolution of surface wave spectra on a beach. *Journal of physical oceanography*, 28(7), 1534–1551.

Oertel, G. F. (1972). Sediment transport of estuary entrance shoals and the formation of swash platforms. *Journal of Sedimentary Research*, 42(4), 858–863.

Ohyama, T. & Nadaoka, K. (1994). Transformation of a nonlinear wave train passing over a submerged shelf without breaking. *Coastal Engineering*, 24(1-2), 1–22.

Ojeda, E., Ruessink, B. G., & Guillen, J. (2008). Morphodynamic response of a two-barred beach to a shoreface nourishment. *Coastal Engineering*, 55(12), 1185–1196.

Osborne, P. D. & Greenwood, B. (1992). Frequency dependent cross-shore suspended sediment transport. 2. a barred shoreface. *Marine Geology*, 106(1-2), 25–51.

Pearson, S. G. (2022). *Sediment Pathways on Ebb-Tidal Deltas: New Tools and Techniques for Analysis*. PhD thesis, Delft University of Technology.

Pearson, S. G., Elias, E. P. L., van Prooijen, B. C., van der Vegt, H., van der Spek, A. J. F., & Wang, Z. B. (2022). A novel approach to mapping ebb-tidal delta morphodynamics and stratigraphy. *Geomorphology*, 405, 108185.

Pearson, S. G., van Prooijen, B. C., Elias, E. P., Vitousek, S., & Wang, Z. B. (2020). Sediment connectivity: A framework for analyzing coastal sediment transport pathways. *Journal of Geophysical Research: Earth Surface*, 125(10), e2020JF005595.

Pearson, S. G., van Prooijen, B. C., Poleykett, J., Wright, M., Black, K., & Wang, Z. B. (2021a). Tracking fluorescent and ferrimagnetic sediment tracers on an energetic ebb-tidal delta to monitor grain size-selective dispersal. *Ocean & Coastal Management*, 212, 105835.

Pearson, S. G., Verney, R., van Prooijen, B. C., Tran, D., Hendriks, E., Jacquet, M., & Wang, Z. B. (2021b). Characterizing the composition of sand and mud suspensions in coastal & estuarine environments using combined optical and acoustic measurements. *Earth and Space Science Open Archive*, (pp.36̃).

Peregrine, D. H. (1976). Interaction of water waves and currents. *Advances in applied mechanics*, 16, 9–117.

Phillips, O. M. (1960). On the dynamics of unsteady gravity waves of finite amplitude part 1. the elementary interactions. *Journal of Fluid Mechanics*, 9(2), 193–217.

Rakha, K. A., Deigaard, R., & Brøker, I. (1997). A phase-resolving cross shore sediment transport model for beach profile evolution. *Coastal Engineering*, 31(1-4), 231–261.

Ranasinghe, R. & Stive, M. J. F. (2009). Rising seas and retreating coastlines.

Reniers, A. & Zijlema, M. (2022). Swan surfbeat-1d. *Coastal Engineering*, 172, 104068.

Reniers, A. J. H. M., De Wit, F. P., Tissier, M. F. S., Pearson, S. G., Brakenhoff, L. B., Van Der Vegt, M., Mol, J., & Van Prooijen, B. C. (2019). Wave-skewness and current-related ebb-tidal sediment transport: Observations and modeling. In *The Proceedings of the Coastal Sediments 2019*. World Scientific.

Reniers, A. J. H. M., Thornton, E. B., Stanton, T. P., & Roelvink, J. A. (2004). Vertical flow structure during sandy duck: observations and modeling. *Coastal Engineering*, 51(3), 237–260.

Ribberink, J. S. & Al-Salem, A. A. (1994). Sediment transport in oscillatory boundary layers in cases of rippled beds and sheet flow. *Journal of Geophysical Research: Oceans*, 99(C6), 12707–12727.

Rijkswaterstaat (1990). *A new coastal defence policy for the Netherlands*. Rijkswaterstaat, RIKZ.

Rijnsdorp, D. P., Buckley, M. L., da Silva, R. F., Cuttler, M. V., Hansen, J. E., Lowe, R. J., Green, R. H., & Storlazzi, C. D. (2021). A numerical study of wave-driven mean flows and setup dynamics at a coral reef-lagoon system. *Journal of Geophysical Research: Oceans*, 126(4), e2020JC016811.

Rijnsdorp, D. P., Ruessink, B. G., & Zijlema, M. (2015). Infragravity-wave dynamics in a barred coastal region, a numerical study. *Journal of Geophysical Research: Oceans*, 120(6), 4068–4089.

Rijnsdorp, D. P., Smit, P. B., & Zijlema, M. (2014). Non-hydrostatic modelling of infragravity waves under laboratory conditions. *Coastal Engineering*, 85, 30–42.

Rijnsdorp, D. P., Smit, P. B., Zijlema, M., & Reniers, A. J. H. M. (2017). Efficient non-hydrostatic modelling of 3d wave-induced currents using a subgrid approach. *Ocean Modelling*, 116, 118–133.

Ris, R. C. (1997). *Spectral modelling of wind waves in coastal areas*. PhD thesis, Delft University of Technology.

Ris, R. C., Holthuijsen, L. H., & Booij, N. (1999). A third-generation wave model for coastal regions: 2. verification. *Journal of Geophysical Research: Oceans*, 104(C4), 7667–7681.

Rocha, M., Silva, P., Michallet, H., Abreu, T., Moura, D., & Fortes, J. (2013). Parameterizations of wave nonlinearity from local wave parameters: a comparison with field data. *Journal of Coastal Research*, 65(sp1), 374–379.

Rocha, M. V. L., Michallet, H., & Silva, P. A. (2017). Improving the parameterization of wave nonlinearities–the importance of wave steepness, spectral bandwidth and beach slope. *Coastal Engineering*, 121, 77–89.

Roelvink, J. A. & Reniers, A. J. H. M. (2011). A guide to modeling coastal morphology.

Roelvink, J. A., Reniers, A. J. H. M., Van Dongeren, A., van Thiel de Vries, J. S. M., McCall, R., & Lescinski, J. (2009). Modelling storm impacts on beaches, dunes and barrier islands. *Coastal engineering*, 56(11-12), 1133–1152.

Roelvink, J. A. & Stive, M. J. F. (1989). Bar-generating cross-shore flow mechanisms on a beach. *Journal of Geophysical Research: Oceans*, 94(C4), 4785–4800.

Roelvink, J. A., van Kessel, T. M., Alfageme, S., & Canizares, R. (2003). Modelling of barrier island response to storms. In *Proceedings of Coastal Sediments*, volume 3 (pp. 1–11).

Ruessink, B. G. (1998). Bound and free infragravity waves in the nearshore zone under breaking and nonbreaking conditions. *Journal of Geophysical Research: Oceans*, 103(C6), 12795–12805.

Ruessink, B. G., Kuriyama, Y., Reniers, A. J. H. M., Roelvink, J. A., & Walstra, D. J. R. (2007). Modeling cross-shore sandbar behavior on the timescale of weeks. *Journal of Geophysical Research: Earth Surface*, 112(F3).

Ruessink, B. G., Michallet, H., Abreu, T., Sancho, F., Van Der A, D. A., Van Der Werf, J. J., & Silva, P. A. (2011). Observations of velocities, sand concentrations, and fluxes under velocity-asymmetric oscillatory flows. *Journal of geophysical research: Oceans*, 116(C3).

Ruessink, B. G., Miles, J. R., Feddersen, F., Guza, R. T., & Elgar, S. (2001). Modeling the alongshore current on barred beaches. *Journal of Geophysical Research: Oceans*, 106(C10), 22451–22463.

Ruessink, B. G., Ramaekers, G., & Van Rijn, L. C. (2012). On the parameterization of the free-stream non-linear wave orbital motion in nearshore morphodynamic models. *Coastal Engineering*, 65, 56–63.

Rusu, L., Bernardino, M., & Soares, C. G. (2011). Modelling the influence of currents on wave propagation at the entrance of the tagus estuary. *Ocean Engineering*, 38(10), 1174–1183.

Sallenger Jr, A. H., Holman, R. A., & Birkemeier, W. A. (1985). Storm-induced response of a nearshore-bar system. *Marine Geology*, 64(3-4), 237–257.

Salmon, J. & Holthuijsen, L. (2015). Modeling depth-induced wave breaking over complex coastal bathymetries. *Coastal Engineering*, 105, 21–35.

Salmon, J. E., Holthuijsen, L. H., Zijlema, M., van Vledder, G. P., & Pietrzak, J. D. (2015). Scaling depth-induced wave-breaking in two-dimensional spectral wave models. *Ocean Modelling*, 87, 30–47.

Salmon, J. E., Smit, P. B., Janssen, T. T., & Holthuijsen, L. H. (2016). A consistent collinear triad approximation for operational wave models. *Ocean Modelling*, 104, 203–212.

Sénéchal, N., Bonneton, P., & Dupuis, H. (2002). Field experiment on secondary wave generation on a barred beach and the consequent evolution of energy dissipation on the beach face. *Coastal Engineering*, 46(3), 233–247.

Sha, L. P. (1989). Sand transport patterns in the ebb-tidal delta off texel inlet, wadden sea, the netherlands. *Marine Geology*, 86(2-3), 137–154.

Sheremet, A., Guza, R. T., Elgar, S., & Herbers, T. H. C. (2002). Observations of nearshore infragravity waves: Seaward and shoreward propagating components. *Journal of Geophysical Research: Oceans*, 107(C8), 10–1.

Silva, P. A., Abreu, T., Van Der A, D. A., Sancho, F., Ruessink, B. G., Van der Werf, J. J., & Ribberink, J. S. (2011). Sediment transport in nonlinear skewed oscillatory flows: Transkew experiments. *Journal of Hydraulic Research*, 49(sup1), 72–80.

Smit, P., Janssen, T., Holthuijsen, L., & Smith, J. (2014). Non-hydrostatic modeling of surf zone wave dynamics. *Coastal Engineering*, 83, 36–48.

Smit, P. B., Janssen, T. T., & Herbers, T. H. C. (2017). Nonlinear wave kinematics near the ocean surface. *Journal of Physical Oceanography*, 47(7), 1657–1673.

Smit, P. B., Zijlema, M., & Stelling, G. S. (2013). Depth-induced wave breaking in a non-hydrostatic, near-shore wave model. *Coastal Engineering*, 76, 1–16.

Soulsby, R. L. (1999). Coastal sediment transport: the coast3d project. In *Coastal Engineering 1998* (pp. 2548–2558). American Society Of Civil Engineers.

Soulsby, R. L., Hamm, L., Klopman, G., Myrhaug, D., Simons, R. R., & Thomas, G. P. (1993). Wave-current interaction within and outside the bottom boundary layer. *Coastal engineering*, 21(1-3), 41–69.

Stive, M. J. F. (1987). A model for cross-shore sediment transport. In *Coastal Engineering 1986* (pp. 1550–1564). American Society of Civil Engineers.

Stive, M. J. F., de Schipper, M. A., Luijendijk, A. P., Aarninkhof, S. G. J., van Gelder-Maas, C., van Thiel de Vries, J. S. M., de Vries, S., Henriquez, M., Marx, S., & Ranasinghe, R. (2013). A new alternative to saving our beaches from sea-level rise: The sand engine. *Journal of Coastal Research*, 29(5), 1001–1008.

Stokes, G. G. (1880). On the theory of oscillatory waves. *Transactions of the Cambridge philosophical society*.

Svendsen, I. A., Madsen, P., & Hansen, J. B. (1978). Wave characteristics in the surf zone. In *Coastal Engineering 1978* (pp. 520–539). American Society Of Civil Engineers.

Thornton, E. B. & Guza, R. T. (1982). Energy saturation and phase speeds measured on a natural beach. *Journal of Geophysical Research: Oceans*, 87(C12), 9499–9508.

Thornton, E. B., Humiston, R. T., & Birkemeier, W. (1996). Bar/trough generation on a natural beach. *Journal of Geophysical Research: Oceans*, 101(C5), 12097–12110.

Tissier, M. F. S., Bonneton, P., Marche, F., Chazel, F., & Lannes, D. (2012). A new approach to handle wave breaking in fully non-linear boussinesq models. *Coastal Engineering*, 67, 54–66.

Tissier, M. F. S., Bonneton, P., Michallet, H., & Ruessink, B. G. (2015). Infragravity-wave modulation of short-wave celerity in the surf zone. *Journal of Geophysical Research: Oceans*, 120(10), 6799–6814.

Tolman, H. L. (1991). A third-generation model for wind waves on slowly varying, unsteady, and inhomogeneous depths and currents. *Journal of Physical Oceanography*, 21(6), 782–797.

Torres-Freyermuth, A., Lara, J. L., & Losada, I. J. (2010). Numerical modelling of short-and long-wave transformation on a barred beach. *Coastal Engineering*, 57(3), 317–330.

Ursell, F. (1953). The long-wave paradox in the theory of gravity waves. In *Mathematical Proceedings of the Cambridge Philosophical Society*, volume 49 (pp. 685–694).: Cambridge University Press.

van der A, D. A., O'Donoghue, T., & Ribberink, J. S. (2010). Measurements of sheet flow transport in acceleration-skewed oscillatory flow and comparison with practical formulations. *Coastal Engineering*, 57(3), 331 – 342.

van der Spek, A. J. F. (2018). The development of the tidal basins in the dutch wadden sea until 2100: the impact of accelerated sea-level rise and subsidence on their sediment budget–a synthesis. *Netherlands Journal of Geosciences*, 97(3), 71–78.

van der Werf, J. J., Alvarez Antolinez, J. A., Brakenhoff, L. B., Gawehn, M., den Heijer, K., de Looff, H van Maarseveen, M. C. G., Meijer Holzhauer, H., Mol, J. W., Pearson, S. G., van Prooijen, B. C., Santinelli, G., Schipper, C. A., Tonnon, P. K., de Vet, P. L. M., Vermaas, T., Wilmink, R. J. A., & de Wit, F. P. (2019). *Datareport Kustgenese 2.0*. Technical report, Rijkswaterstaat.

Van der Westhuysen, A. J. (2007). *Advances in the spectral modelling of wind waves in the nearshore. The Netherlands: Delft University of Technology*. PhD thesis, Ph. D. thesis, 207p.

Van Dongeren, A., Reniers, A. J. H. M., Battjes, J. A., & Svendsen, I. (2003). Numerical modeling of infragravity wave response during delilah. *Journal of Geophysical Research: Oceans*, 108(C9).

van Prooijen, B. C., Tissier, M. F. S., de Wit, F. P., Pearson, S. G., Brakenhoff, L. B., van Maarseveen, M. C. G., van der Vegt, M., Mol, J.-W., Kok, F., Holzhauer, H., van der Werf, J. J., Vermaas, T., Gawehn, M., Grasmeijer, B., Elias, E. P. L., Tonnon, P. K., Santinelli, G., Antolínez, J. A. A., de Vet, P. L. M., Reniers, A. J. H. M., Wang, Z. B., den Heijer, C., van Gelder-Maas, C., Wilmink, R. J. A., Schipper, C. A., & de Looff, H. (2020). Measurements of hydrodynamics, sediment, morphology and benthos on ameland ebb-tidal delta and lower shoreface. *Earth System Science Data*, 12(4), 2775–2786.

Van Rijn, L. C. (2007). Unified view of sediment transport by currents and waves. i: Initiation of motion, bed roughness, and bed-load transport. *Journal of Hydraulic engineering*, 133(6), 649–667.

Van Rijn, L. C., Ruessink, B. G., & Mulder, J. P. M. (2002). *Coast3D-Egmond: The Behaviour of a Straight Sandy Coast on the Time Scale of Storms and Seasons: Process Knowledge and Guidelines for Coastal Management: End Document, March 2002*. Aqua Publications.

Van Rijn, L. C., Walstra, D. J. R., & Ormondt, M. v. (2004). Description of transpor2004 and implementation in delft3d-online. *Z3748*.

van Weerdenburg, R. J. A. (2019). Exploring the relative importance of wind for exchange processes around a tidal inlet system: The case of ameland inlet. Master's thesis, Delft University of Technology.

Walstra, D. J. R., Reniers, A. J. H. M., Ranasinghe, R., Roelvink, J. A., & Ruessink, B. G. (2012). On bar growth and decay during interannual net offshore migration. *Coastal Engineering*, 60, 190–200.

Walstra, D. J. R., Roelvink, J. A., & Groeneweg, J. (2001). Calculation of wave-driven currents in a 3d mean flow model. In *Coastal Engineering 2000* (pp. 1050–1063). American Society Of Civil Engineers.

Wang, Z. B., Elias, E. P. L., van der Spek, A. J. F., & Lodder, Q. J. (2018). Sediment budget and morphological development of the dutch wadden sea: impact of accelerated sea-level rise and subsidence until 2100. *Netherlands Journal of Geosciences*, 97(3), 183–214.

Wang, Z. B., Hoekstra, P., Burchard, H., Ridderinkhof, H., De Swart, H. E., & Stive, M. J. F. (2012). Morphodynamics of the wadden sea and its barrier island system. *Ocean & coastal management*, 68, 39–57.

Warner, J. C., Sherwood, C. R., Signell, R. P., Harris, C. K., & Arango, H. G. (2008). Development of a three-dimensional, regional, coupled wave, current, and sediment-transport model. *Computers & Geosciences*, 34(10), 1284–1306.

Watanabe, A. & Isobe, M. (1991). Sand transport rate under wave-current action. In *Coastal Engineering 1990* (pp. 2495–2507). American Society of Civil Engineers.

Watanabe, A. & Sato, S. (2005). A sheet-flow transport rate formula for asymmetric, forward-leaning waves and currents. In *Coastal Engineering 2004: (In 4 Volumes)* (pp. 1703–1714). World Scientific.

Wei, G., Kirby, J. T., Grilli, S. T., & Subramanya, R. (1995). A fully nonlinear boussinesq model for surface waves. part 1. highly nonlinear unsteady waves. *Journal of Fluid Mechanics*, 294, 71–92.

Westerink, J. J., Luettich Jr, R., Blain, C., & Scheffner, N. W. (1994). *ADCIRC: an advanced three-dimensional circulation model for shelves, coasts, and estuaries. Report 2. User's manual for ADCIRC-2DDI.* Technical report, Army engineer waterways experiment station Vicksburg MS.

Wright, L. D., Boon, J. D., Kim, S. C., & List, J. H. (1991). Modes of cross-shore sediment transport on the shoreface of the middle atlantic bight. *Marine Geology*, 96(1-2), 19–51.

Young, I. R. & Eldeberky, Y. (1998). Observations of triad coupling of finite depth wind waves. *Coastal engineering*, 33(2-3), 137–154.

Zijlema, M., Stelling, G. S., & Smit, P. B. (2011). Swash: An operational public domain code for simulating wave fields and rapidly varied flows in coastal waters. *Coastal Engineering*, 58(10), 992–1012.

LIST OF SYMBOLS

Abbreviations and acronyms

$DOFs$	degrees of freedom	N/A
$RMSE$	Root Mean Squared Error	N/A

Greek

$\alpha(f)$	weighting factor	[-]
α_{BJ}	breaking scaling factor	[-]
α_{break}	bound wave breaking ratio	[-]
α_{LTA}	proportionality coefficient for LTA	[-]
α_{SPB}	proportionality coefficient for SPB	[-]
$\beta(f,f)$	biphase	$[rad]$
β_{Ur}	parameterized biphase	$[rad]$
$\Delta\theta$	directional resolution	[°]
Δd	depth difference	$[m]$
Δf	frequency resolution	$[Hz]$
Δk	wave number mismatch	$[m^{-1}]$
Δx	spatial resolution	$[m]$
η	surface elevation	$[m]$
γ	breaker index	[-]
γ_{spec}	spectral peak-enhancement factor	[-]
ω	absolute angular frequency	$[Hz]$
ϕ	wave phase	$[rad]$
Ψ	proportionality factor	[-]
ρ	density	$[kgm^{-3}]$
σ	intrinsic angular frequency	$[Hz]$
σ_{θ_w}	wave directional spreading	[°]
Θ	normalized directional distribution	[-]
θ_U	mean current direction	[°]
θ_w	mean wave direction	[°]
Θ_{new}	adapted normalized directional distribution	[-]

Mathematical operators

$\Im$	imaginary part	N/A
$\langle ... \rangle$	burst averaging	N/A
$\lvert ... \rvert$	absolute value operator	N/A
$\mathscr{H}\{...\}$	imaginary part of Hilbert transform	N/A
$\Re$	real part	N/A
$\mathbf{E}[...]$	expected value operator	N/A
*	complex conjugate operator	N/A

Roman

$\tilde{Q}$	second order contribution to bispectrum for LTA	$[m^2 Hz^{-2}]$
$\widehat{Ur}$	spectral Ursell number	[-]
$\widetilde{As_q}$	dimensional asymmetry	$[dim(q)^3]$
$\widetilde{S_q}$	dimensional combined wave shape	$[dim(q)^3]$
$\widetilde{Sk_q}$	dimensional skewness	$[dim(q)^3]$
A	wave amplitude	$[m]$
a	calibration parameter for SPB	[-]
$A^\star$	delayed wave amplitude	$[m]$
As	dimensionless asymmetry	[-]
b	calibration parameter for SPB	[-]
$B(f,f)$	bispectral density	$[m^3 Hz^{-2}]$
$b(f,f)$	bicoherence	[-]
$B_{m,n}$	discrete bispectrum	$[m^3]$
C	complex amplitude	$[m]$
c	wave celerity	$[ms^{-1}]$
c_g	wave group celerity	$[ms^{-1}]$
D	nonlinear interaction coefficient	$[m^{-1}]$
d	local water depth	$[m]$
$d^\star$	delayed local water depth	$[m]$
D_z	nonlinear interaction coefficient at depth z	$[m^{-1}]$
E	single sided discrete variance spectrum	$[m^2]$
E'	double sided discrete variance spectrum	$[m^2]$
$E'(f,\theta)$	double sided frequency-directional variance density spectrum	$[m^2 Hz^{-1} rad^{-1}]$
$E(f)$	single sided variance density spectrum	$[m^2 Hz^{-1}]$
$E(f,\theta)$	single sided frequency-directional variance density spectrum	$[m^2 Hz^{-1} rad^{-1}]$
$E_b(f)$	single sided bound variance density spectrum	$[m^2 Hz^{-1}]$
f	frequency	$[Hz]$
f_c	cut-off frequency	$[Hz]$
f_N	Nyquist frequency	$[Hz]$
f_s	discrete sampling frequency	$[Hz]$
$f_{i_{b,max}}$	upper bound for the bound super harmonic frequency range	$[Hz]$
$f_{i_{b,min}}$	lower bound for the bound super harmonic frequency range	$[Hz]$
$f_{i_{max}}$	upper bound for the sea-swell frequency range	$[Hz]$
$f_{i_{min}}$	lower bound for the sea-swell frequency range	$[Hz]$
f_{peak}	peak frequency	$[Hz]$
G	breaking parameter	[-]
g	gravitational acceleration	$[ms^{-2}]$
H	significant wave height	$[m]$
$H_{b,hass}$	parameterized bound wave height (Hasselmann, 1962)	$[m]$
H_{br}	wave height at location of wave breaking	$[m]$
H_b	bound superharmonic wave height	$[m]$
i	imaginary number	[-]
j	order of the spectral moment	[-]
K	calibration parameter for SPB	$[m^{-1}]$

k	wave number	$[m^{-1}]$
$k^{\star}$	delayed wave number	$[m^{-1}]$
$k_{-1,0}$	minus first order moment wave number	$[m^{-1}]$
$K_{att,b}(f_m)$	bound attenuation factor	[-]
$K_{att}(f_m)$	attenuation factor	[-]
$k_{peak,local}$	local peak wave number	$[m^{-1}]$
$k_{peak,offshore}$	offshore peak wave number	$[m^{-1}]$
k_{peak}	peak wave number	$[m^{-1}]$
L	wave length	$[m]$
M	directional width power	[-]
m,n,p	frequency indices	[-]
m_0	zero-th order moment	$[m^2]$
m_1	first order moment	$[m^2 Hz]$
m_2	second order moment	$[m^2 Hz^2]$
m_j	j-th order moment	$[m^2 Hz^j]$
m_{-1}	minus first order moment	$[m^2 Hz^{-1}]$
m_{min}	index of first discrete frequency in sea-swell range (Ch. 4)	[-]
N	number of discrete frequencies	[-]
N_θ	number of discrete wave directions	[-]
P	power of directional distribution	[-]
p	water pressure	$[kgm^{-1}s^{-2}]$
p_{air}	air pressure	$[kgm^{-1}s^{-2}]$
p_{total}	total pressure	$[kgm^{-1}s^{-2}]$
Q	second order contribution to bispectrum for SPB	$[m^2 Hz^{-2}]$
Q_b	fraction of breaking waves	[-]
r,s	direction indices (Ch. 4)	[-]
R^2	correlation coefficient	[-]
S	dimensionless combined wave shape	[-]
$S_{b,break}$	bound breaking source term	$[m^2]$
S_{break}	breaking source term	$[m^2]$
$S_{nl3,LTA}$	LTA nonlinear triad source term	$[m^2]$
$S_{nl3,SPB}$	SPB nonlinear triad source term	$[m^2]$
S_{nl3}	nonlinear triad source term	$[m^2]$
S^{+}_{nl3}	positive contributions of SPB nonlinear triad source term	$[m^2]$
S^{-}_{nl3}	negative contributions of SPB nonlinear triad source term	$[m^2]$
$S_{p,hass}$	estimate of the parameterized wave shape based on	[-]
S_{rue}	parameterized dimensionless velocity wave shape (Ruessink et al., 2012)	[-]
Sk	dimensionless skewness	[-]
t	time	$[s]$
$T_{m-1,0}$	minus first-order moment wave period	$[s]$
$T_{m0,1}$	first-order moment wave period	$[s]$
$T_{m0,2}$	second-order moment wave period	$[s]$
T_{peak}	peak period	$[s]$
U	mean current magnitude	$[ms^{-1}]$
u	(orbital) velocity in x direction	$[ms^{-1}]$

U_N	mean current in direction of wave propagation	$[ms^{-1}]$
U_{east}	eastward mean current	$[ms^{-1}]$
U_{north}	northward mean current	$[ms^{-1}]$
u_{p2u}	pressure derived orbital velocity	$[ms^{-1}]$
Ur	Ursell number	[-]
$Ur^{\star}$	delayed Ursell number	[-]
Ur_{crit}	critical Ursell number	[-]
v	(orbital) velocity in y direction	$[ms^{-1}]$
$W_{m,n}$	nonlinear interaction coefficient	$[m^{-2}]$
x, y	horizontal spatial coordinates	$[m]$
z	vertical spatial coordinate	$[m]$
z_p	sensor height above the bed	$[m]$

Sub- and superscripts

η	subscript indicating shape of surface elevation signal	[N/A]
b	referring to the bound part of the spectrum or wave height	[N/A]
$bound$	referring to the bound part of the spectrum or wave height	[N/A]
$F1, etc$	referring to a specific frame location	[N/A]
$free$	referring to the free part of the spectrum	[N/A]
mod	subscript referring to a modelled parameter	[N/A]
nb	superscript referring to a parameter near the bottom	[N/A]
nc	subscript indicating no currents	[N/A]
obs	subscript referring to a measured or observed parameter	[N/A]
p	subscript indicating shape of the pressure signal	[N/A]
$P1, etc$	referring to a specific pressure sensor location	[N/A]
$p2u$	subscript indicating shape of the near-bed velocity signal estimated from the pressure	[N/A]
$pred$	subscript referring to a predicted parameter	[N/A]
q	subscript indicating shape of quantity q	N/A
rue	referring to parameterization by Hasselmann (1962)	[N/A]
rue	referring to parameterization by Ruessink et al. (2012)	[N/A]
u	subscript indicating shape of the near-bed velocity signal	[N/A]

ACKNOWLEDGEMENTS

As a kid I was impressed by tall buildings and large bridges. With mathematics and physics being my favourite courses in school, the decision to study Civil Engineering in Delft was relatively straightforward. During my bachelors, my attention shifted towards water related topics. Together with my life-long passion for sailing this explained doing my master in Hydraulic Engineering.

At one of the first days of my MSc graduation project at the group of Environmental Fluid Mechanics, one of the PhD's asked whether I intended to do a PhD after my graduation. I remember thinking: "Hell no, let's graduate and get out of here.". Eventually, things turned out differently and now here I am, writing these acknowledgements. It's been a long journey, but there are two things I'm certain of. First, I wouldn't want to have missed it. Second, I couldn't have done it alone. Therefore, this chapter is devoted to thanking all the people who helped me throughout this journey.

At first, I would like to thank the two most important contributors to this thesis, my two promotors, Marion and Ad. I admire your enthusiasm and passion for wave research, but also your understanding that there is much more in life than work. Marion, thanks for guiding me in my first steps as a researcher, for your (critical) feedback that significantly improved the quality of this thesis, for always finding potential solutions to my never-ending problems and for staying positive when I was not. I am aware that I might not have been (read: am far from) the easiest person to supervise and that I did not always directly listen, but I am truly thankful for all your help. Ad, many thanks that I could always walk into your office, for sharing your endless experience in wave modelling, for your creative ideas that led to the final chapters of this thesis, but also for just writing pieces of code together at the moments I was really stuck. Ad and Marion, besides all work-related things, I really enjoyed all the laughs, drinks and diners together, I hope we'll keep doing this!

There are three other important people I need to thank. Dirk, Pieter and James, during my master thesis you managed to spread the passion for wave research and modelling in such a way that convinced me to do a PhD. Since then, most of the time we have been in four different countries. Yet, when I was stuck, you were always there to take the time to provide very clear and useful advice, which was very helpful and highly appreciated. Furthermore, I really enjoyed all the nerdy modelling discussions, beers and conferences together. On a similar note, I would like to thank Marcel Zijlema. Even though we have not actively worked together, since my focus shifted more towards field measurements and data analysis, you've been of great help. It was amazing and extremely helpful to have one of the best modellers around that could help with literally any numerical question related to SWAN and SWASH. Also I would like to thank you Marcel, together with Stefan Aarninkhof, Gerben Ruessink, Dano Roelvink and France Floc'h, for taking the time to be the independent committee members during my PhD defence, it is an honor to have you.

Stuart, you've been an amazing partner in the SEAWAD project. It was great planning and executing our first field campaign together. You keep surprising me with the infinite

amount of enthousiasm for literally every research. A massive thanks for this contagious enthousiasm, for always being there for a chat and for all the other things you've helped me with! Bram, you've done a great job as the SEAWAD project leader. Thanks for keeping everyone together in the project, which was definitely not a trivial task. Another thanks to the other PhD's in the SEAWAD project: Harriette, Laura and Klaas, the whole supervisory team, the user committee and all field campaign partners. A special thanks goes to Rijkswaterstaat for making the Kustgenese2/SEAWAD field campaign and great data set possible. Also, I would like to thank all the MSc thesis graduates within the project. Maartje it was a pleasure working together. You were the greatest field worker we could have wished for and without you the drifter campaign wouldn't have been half as successful. Also your thesis work formed the pioneering steps for my first paper. Tolga, you picked one of the most challenging thesis topics there was and I'm well aware how frustrating non-working models are. Yet, you surprised me in the tremendous amount of work and simulations you managed to perform during this short amount of time, resulting in a great thesis. Thanks for working together and your contributions to the SWASH model.

Without any doubt the worst office at TU Delft is room 2.95 in Civil Engineering. It started with James trying to prove his point that this office is so hot that you can grow tropical plants in there. The following years literally everything broke down: windows, doors, locks, curtains, blinds, etc. But it should be said, being together in such a miserable office did bring togetherness and some great friendships. Sotiria, thanks for being my office mate the longest, for bringing your combination of kindness and craziness to the office every day and thanks for your knowledge of internet. Gal, thanks for filling in James' spot as the other wave modeller in the office and help to keep all the oceanographers quiet. Thanks for being stuck together on the same annoying topics, which led to some great discussions. Carine, thanks for being a great friend and for always being in for a coffee, even if you just had one five minutes before. But off course also a big thanks for always being angry with the world, which made the world much nicer for us. Lennart, thanks for bringing some well needed gender balance in the lunch group. But also a huge thanks for being my buddy the last years and for your dry sense of humor and all the associated laughs. Silke, my apologies for me being me most of the time. It was quite annoying (and amazing) how calm and mature you kept responding to all my silly jokes. But besides this, also a big thanks for all the sports chats and being part of the group the last years.

Another thanks for all the chats, coffees, beers, runs and rides goes to all my other colleagues and friends from the second floor, lab and third floor: Otti, Sabine, Steffie, Said, Nils, Juanma, Xuexue, Daan, Tess, Marlein, Irene (x2), Alejandra, Erik, Victor, Lodewijk, Yorick, Jill, Ana, Claudia, Patricia, Judith, Sierd, Matthieu, Max, Matthijs, Paul and Marlies. A special thanks is reserved for Anna, who happened to be a great company on all my conferences. But mainly a big thanks for introducing me to Svašek at the perfect moment when I was looking for a new career move. Thereby I also want to thank all my present colleagues at Svašek for the great work atmosphere. In particular, I would like to thank Bram and Bas for guiding me in my new role in the engineering world.

Modelling waves is amongst the most amazing things there is. Nevertheless, I truly believe that it is equally important to have amazing distractions from work. Therefore, the following is devoted to all my friends outside of the office. Thanks to all my sailing friends, with whom I really manage to escape from everything and fully enjoy. It would be

impossible to mention them all, but a special thanks to Job, Art, Wender, Jesse, DJ, Poolen, Teun, Dilara, Auke, Olli, Coen and the Tantetjes (for all the racing we did together), Joris (for all the crazy adventures and for becoming a great friend), Derk, Mick, Trap and Wolt (for all the great diners and weekends), Maarten and Lucas (for the numerous hours of video calls), Eijk, Jules, Erik, Gilles, Thom, Wouter, Ron, Tim, Tammo, Jikke, Floor, Eef and An (for all the beers) and all other friends from Vinea and DMTRA.

Another thanks to all my friends from Delft. Starting at the VJL43 where I had a great 5 years. In line with that I want to thank all members from Club Styx and WBS45 for the amazing adventures we've had and hopefully will have in the future. Then my Waterbouw friends. During my masters I really started enjoying my time at TU Delft, with the trips to Indonesia and Mexico (with Ewoud, Heinie and Ben) being the absolute highlights. A special thanks to Pieter, with who I organized the trip to Indonesia, who became my housemate, spread his passion for pasta and canned-tomatoes and became a very good friend.

Further, I want to acknowledge and thank the importance of my two paranymphs and great friends, Quirijn and Friso (better known as Q and Ed). Our somewhat random decision to move from Delft to WBS45 in The Hague in 2014 turned out the be a great one. Q thanks for being the HO, for cleaning up the house and for sharing the same excessive passion for running and cycling. Thanks for the numerous hours on the bike, either sweating our asses off but also the easy rides where we chat about anything. This is so valuable to me that I take for granted that you crash into me once in a while. Ed, without you it would be pretty silent as Q and me preferably don't talk. So thanks for keeping the conversations going and for all the great stories (even the untrue stories are nice!). But also thanks for understanding the struggles that come with a PhD and for being the cook in our three man household. Q and Ed, even though you support a shitty football club, you are great friends and I'm happy to have you as paranymphs during my defence.

The final words are reserved for my family, Pap, Mam, Roeland and Emma. A big thanks for providing everything such that I was able to experience a completely carefree youth and student time. Being born and raised as a kid of two mathematicians, diner discussions on imaginary numbers, isosceles triangles or differential equations were not uncommon. This has helped tremendously throughout my school, university and PhD time. Now, being (sort of) grown up, I handle things quite independently. Still, on those occasional moments, once or twice a year, it is amazing to know that you're always unconditionally there to help me out. But also thanks for the numerous hours at the kitchen table, having diner and chatting about life. Overall, a huge thanks for everything!

About the author

Being born in Leidschendam, on 25 March 1991, I attended secondary education at the Sint-Maartenscollege in Voorburg from 2003 to 2009. After this my academic education (BSc and MSc) started in Civil Engineering at Delft University of Technology. In 2016 I graduated with distinction at the section of Environmental Fluid Mechanics conducting my MSc thesis research titled: "Tide-induced currents in a phase-resolving wave model". In the same year I started a PhD in the same section within the SEAWAD Project. At the beginning of 2021, I started working at Svašek Hydraulics. Parallel to my educational, academic and professional career I practiced a wide variety of sports with great enthusiasm, such as sailing, cycling and running.

LIST OF PUBLICATIONS

JOURNAL ARTICLES

- **de Wit, F.P.,** Tissier, M.F.S. and Reniers, A.J.H.M., (2020), Characterizing Wave Shape Evolution on an Ebb-Tidal Shoal, *Journal of Marine Science and Engineering 8*(9), 643.

- **de Wit, F.P.,** Tissier, M.F.S. and Reniers, A.J.H.M., (2019), Characterizing Wave Shape Evolution on an Ebb-Tidal Shoal, *Journal of Marine Science and Engineering 7*(10), 367.

- van Prooijen, B.C., Tissier, M.F.S., **de Wit, F.P.**, Pearson, S.G., Brakenhoff, L.B., van Maarseveen, M.C.G., van der Vegt, M., Mol, J.-W., Kok, F., Holzhauer, H., van der Werf, J.J., Vermaas, T., Gawehn, M., Grasmeijer, B., Elias, E.P.L., Tonnon, P.K., Santinelli, G., Antolínez, J.A.A., de Vet, P.L.M., Reniers, A.J.H.M., Wang, Z.B., den Heijer, C., van Gelder-Maas, C., Wilmink, R.J.A., Schipper, C.A., de Looff, H. (2020), Measurements of hydrodynamics, sediment, morphology and benthos on Ameland ebb-tidal delta and lower shoreface, *Eart System Science Data 12*(4), 2775-2786.

CONFERENCE PROCEEDINGS

- **de Wit, F.P.,** Tissier, M.F.S. and Reniers, A.J.H.M., (2018), Field study on influence of tidal currents on intra-wave sediment transport, *Coastal Engineering Proceedings 2018*.

- **de Wit, F.P.,** Tissier, M.F.S. and Reniers, A.J.H.M., (2017), Including tidal currents in a wave-resolving model, *Coastal Dynamics Proceedings 2017*.

- Pearson, S.G., van Prooijen, B.C., **de Wit, F.P.,** Meijer-Holzhauer, H., de Looff, H. and Wang Z.B. (2019), Observations of suspended particle size distribution on an energetic ebb-tidal delta, *Coastal Sediments Proceedings 2019*.

- Reniers, A.J.H.M., **de Wit, F.P.,** Tissier, M.F.S., Pearson, S.G., Brakenhoff, L.B., van der Vegt, M., and Mol, J.-W., van Prooijen, B. C., (2019), Wave-skewness and current-related ebb-tidal sediment transport: observations and modeling, *Coastal Sediments Proceedings 2019*.

- Hopkins, J., de Schipper, M.A., Wengrove, M., **de Wit, F.P.,** Castelle, B., (2019), Observations and numerical model results of morphodynamic feedback owing to wave-current interaction, *Coastal Sediments Proceedings 2019*.

- Grossmann, F, Gawehn, M, de Vries, S, **de Wit, F.P.,** Aarninkhof, S.G.J. (2019), Comparison of Currents Derived from X-band Radar and Collected In-situ Datain Ameland Inlet, *Coastal Structures 2019*.

- van Prooijen, B. C., de Looff, H., Pearson, S.G.P., Mol, J. W., **de Wit, F.P.,** Tissier, M.F.S, Kok, F., Tonnon, P.K., van der Vegt, M., Brakenhoff, L.B., Wilmink, R.J.A., van Weerdenburg, R. and Wang, Z.B. (2018), Large-scale field campaign for improving nourishment strategies in the Netherlands - Exploring the effects of wind, *AGU Fall Meeting Abstracts 2018*.